upna
Universidad Pública de Navarra
Nafarroako Unibertsitate Publikoa

THESIS FOR THE DEGREE OF DOCTOR OF PHILOSOPHY

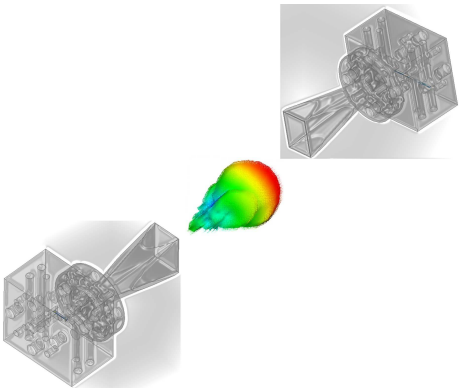

Development of sub-millimetre wave band subsystems and packaging techniques

José Manuel Pérez Escudero

Codirector: Ramón Gonzalo García

Codirector: Iñigo Ederra Urzainqui

Grupo de Antenas
Departamento Ingeniería Eléctrica, Electrónica y de las Comunicaciones
Universidad Pública de Navarra
Pamplona, España, 2019

Agradecimientos

En primer lugar me gustaría dar las gracias a todas las personas que durante estos cuatro años y de un modo u otro han ayudado a que pueda realizar y escribir esta tesis, aunque no esté su nombre aquí. Gracias a todos.

Dicho esto, me gustaría agradecer a mis directores de tesis, Ramón e Iñigo, por todo su apoyo, sus consejos, sus explicaciones y sobre todo su paciencia. Por todo lo que me han enseñado y las oportunidades que me han brindado durante este tiempo; la posibilidad de viajar, conocer gente y crecer como persona, pues el doctorado es más que investigación. Muchas gracias porque no solo sois grandes supervisores sino que además sois grandísimas personas.

Gracias Jorge porque aunque no seas mi director de tesis está claro que has contribuido enormemente a ella, por enseñarme temas de fabricación, de darme la oportunidad de trabajar en sala limpia y por dar siempre buenos consejos a la hora de medir. También darte las gracias, a tí y a Marian, por ayudarnos en lo personal a Alicia y a mí. ¡¡Gracias!!

Por supuesto a Anteral y a todo el Grupo de Antenas, a los que estaban cuando llegué y ya se han ido y a los que siguen.

Principalmente a aquellos con los que no solo hemos compartido despacho sino momentos personales e importantes en nuestras vidas, juevintxos, excursiones y salidas varias, Miguel, Adur, Victor Torres, Victor Pacheco, Baha, Pablo, Unai, Iñigo, Alexia, Irati, Carlos Quemada, Carlos Biurrun, Dayán.

I would also like to thank the Terahertz and Millimetre Wave Laboratory from Chalmers Technology University for the very warm welcome and teaching me so much! It was an incredible experience. I have really happy memories to work with you and to enjoy those Fika moments.

Por último y para mi lo más importante, gracias a mi familia. Gracias a mi familia cubana por acogerme tan bien cuando voy en verano. Por supuesto, GRACIAS a mi madre y a mis hermanas por apoyarme desde el primer momento en que decidí venir a Pamplona a realizar el doctorado y porque siempre estáis ahí para todo, para lo bueno y para lo malo. No puedo olvidarme de mi padre, que por desgracia nos dejó antes de tiempo y del que me acuerdo cada día, me sigues enseñando. Finalmente, MIL GRACIAS a las dos personas que me acompañan todos los días en todo lo que hago. Alicia gracias por ser mi compañera, mi amiga, mi esposa, por soportarme y por comprenderme, por ayudarme, en fin, por todo. José Manuel porque es imposible describir cómo se puede amar tanto a algo tan pequeño, me haces feliz y me alegras cada día. Os amo!

Right now we only have one planet, and we need to work together to protect it.

Stephen Hawking

Resumen

Hasta hace poco más de cuatro décadas había un vacío en la generación y detección de ondas en la parte del espectro situada entre 100 GHz y 10 THz (longitudes de onda desde 3 mm hasta 30 μm) que se conoce como el vacío de Terahercios. No obstante, recientemente, ha habido un gran auge y un acelerado desarrollo en la investigación de dispositivos en este rango de frecuencias que han permitido reducir este "hueco". El gran interés que despierta dicho rango espectral se debe, sobre todo, a la gran utilidad que presenta para imagen médica o escáneres de imagen para seguridad en los aeropuertos, para el estudio de la atmósfera o formación de estrellas, para las comunicaciones inalámbricas de alta capacidad, etc.

En esta tesis se investigan técnicas de diseño y fabricación de dispositivos, ya sean transmisores o receptores, a frecuencias de THz y submilimétricas y técnicas de empaquetado con el objetivo de que el dispositivo final sea más compacto. Esto es interesante sobre todo pensando en uso comercial o en la integración en satélites, ya que en ambos casos la portabilidad y facilidad de uso son muy importantes.

El contenido de la tesis puede dividirse en dos partes bien diferenciadas. La primera de ellas parte de la base de que no hay conectores a tan alta frecuencia y es necesario el uso de equipamiento basado en guía de onda para medir y caracterizar los dispositivos fabricados en estas bandas de frecuencia.

Por lo tanto, la primera parte está orientada hacia el diseño de transiciones de tecnología planar con la tecnología en guía de onda partiendo de un análisis teórico y con el objetivo de un ensamblado sencillo. Este método ha sido aplicado a guía de onda rectangular estándar y también a tecnologías novedosas tales como Gap waveguide. Concretamente, en este trabajo se presentan cuatro transiciones en línea cuyo diseño provee ventajas desde el punto de vista computacional, por el ahorro de recursos y tiempo, además de la sencillez desde el punto de vista de fabricación y ensamblado.

La segunda parte trata el diseño, análisis y fabricación de dispositivos integrados compactos basados en diodos Schottky. Específicamente, dos mezcladores de frecuencia con ocilador local basado en MMIC y un transmisor optoelectrónico. Uno de los prototipos es un mezclador cuarto armónico y el otro es un mezclador subarmónico, que usa el mismo LO e integra un multiplicador de frecuencia en el mismo substrato. Por medio de esta integración se consigue dispositivos de ensamblado más sencillo y más compactos, cuyo comportamiento es cercano al estado del arte. Además, el transmisor optoelectrónico integra el mismo substrato un fotodiodo UTC y un triplicador de frecuencia basado en dio-

dos Schottky. De esta manera, el rango de operación del fotodiodo UTC puede ser extendido a frecuencias más altas, manteniendo sus ventajas, tales como la posibilidad de integración con fibra óptica para enlaces de alta capacidad.

Por último, se ha diseñado un mezclador sexto armónico basado en la tecnología membrana de arseniuro de galio. Esta tecnología permite la integración de los diodos Schottky en la membrana junto con la circuitería microstrip, de tal forma que los diodos no tienen que ser soldados. En este diseño, además, un triplicador de frecuencia se integra también en la misma membrana que el mezclador armónico. Por lo tanto, el comportamiento final del mezclador sexto armónico es similar al de un mezclador subarmónico. De esta forma es más fácil encontrar fuentes con bastante potencia dado que el oscilador trabaja a una frecuencia más baja. Asimismo, gracias a la integración, los problemas causados por desalineamiento durante el ensamblado de los componentes individuales se evitan.

Abstract

Until four decades ago, there was a gap in the generation and detection of electromagnetic waves in the part of the spectrum between 100 GHz and 10 THz (wavelengths from 3 mm to 30 μm) known as the Terahertz gap. Nonetheless, during the last four decades, a great rising interest and progress in research on devices working in the sub-millimetre (sub-mm) and THz bands have allowed to reduce this gap. These frequencies are generating a great interest due to the high possibilities they present for medical or security imaging, atmosphere study or radioastronomy, high-data rates wireless communications, etc.

In this thesis, different design and fabrication techniques for devices, both receiver and transmitter, working in the THz and sub-mm wave bands are investigated. Different packaging and integration techniques have also been evaluated, so that the final devices can be more compact. This is of great interest from the point of view of commercial communication systems and space instruments, since in both cases portability, compactness and reduced size is imperative.

The thesis outline covers two aspects of the system integration and packaging. The first one is based on the fact that sub-mm and THz device packaging requires transitions to waveguides, since there are not connectors for such high frequencies.

According to this, the first part of the thesis is orientated to the design of planar to waveguide transitions based on a straightforward theoretical analysis and with simple assembly. This method has been applied to standard rectangular waveguides and also to innovative technologies such as gap waveguide. This last technology simplifies assembly and improves the performance with respect to standard split-block technology. Concretely, four inline transitions are proposed providing several advantages from the point of view of simple analytic design, which saves computational resources and time, manufacturing and ease of assembly.

The second part of the thesis focuses on the design, analysis and fabrication of Schottky diode based compact integrated devices. Specifically, two frequency mixers with a MMIC based local oscillator for integrated packaging and an optoelectronic transmitter. One of the prototypes is a fourth harmonic mixer and the other one is a subharmonic mixer, which uses the same LO and integrates a frequency multiplier in the same substrate. By means of this integration procedure we achieve a more compact and simpler assembly device, with close to the state of the art performance. Besides, the optoelectronic transmitter integrates an UTC-Photodiode and a Schottky diode frequency tripler in the same substrate. This way, the operation frequency range of the UTC photodiodes can

be extended to higher frequencies, while keeping their advantages, such as the possibility of integration with an optical fiber for high data rate links.

Finally, a sixth harmonic mixer based on GaAs membrane technology has been designed. This technology allows the integration of the Schottky diodes with the membrane in which the microstrip lines are printed. This fabrication process provides a solution to the discrete diodes circuit design, whose performance and functionality is limited, mainly because the diodes needs to be welded to the substrate. In this design, furthermore, a frequency tripler is integrated in the same membrane that the harmonic mixer. Therefore, the final behaviour of the sixth harmonic mixer is more similar to the subharmonic mixer behaviour. This way, it is easier to find sources with enough power insomuch as the local oscillator works at a relatively low frequency. In addition, thanks to the integration, problems caused by misalignments during assembly of the individual components are avoided.

Contents

1 Introduction **1**

1.1 Brief introduction to THz communications 3

1.2 Background 6

1.2.1 Introduction to Packaging 6

1.2.2 Terahertz Photonic Sources 7

1.2.3 Electronic Sources 11

1.3 Motivation and thesis outline 18

2 Inline Transitions from Planar to Waveguide Technology at W-Band **21**

2.1 Theoretical analysis 23

2.1.1 Theoretical analysis based on Chebyshev transformer . . 23

2.1.2 Theoretical analysis for pin dimension 24

2.2 Microstrip to Standard WR-10 Waveguide Transition 26

2.2.1 Configuration and Transition Concept 26

2.2.2 Design and Simulation Results 29

2.2.3 Manufacturing 33

2.2.4 Experimental Validation 34

2.3 Microstrip to Groove Gap Waveguide Transition 36

2.3.1 Proposed Transition and Simulation Results 36

2.3.2 Tolerance analysis 43

2.3.3 Manufacturing and Experimental validation 45

2.4 Microstrip to Rectangular Waveguide Transition Packaged by Gap Waveguide . . . 48
2.4.1 Transition Concept . . . 48
2.4.2 Groove gap waveguide characteristics . . . 48
2.4.3 Transition design . . . 51
2.4.4 Simulated performance of the proposed prototypes . . . 52
2.4.5 Experimental Validation . . . 55
2.5 Microstrip to Waveguide transition based on Ridge-Groove Gap with very simple assembly . . . 58
2.5.1 Proposed configuration and simulated performance . . . 58
2.5.2 Manufacturing and experimental validation . . . 60
2.6 Conclusions . . . 64

3 Harmonic Mixers Based on Schottky Diodes with Integrated MMIC based Local Oscillator 67
3.1 MMIC Local Oscillator . . . 71
3.2 Fourth harmonic mixer . . . 73
3.2.1 Design topology . . . 74
3.2.2 3D-Model of the Diode . . . 75
3.2.3 Passive Circuit Design . . . 76
3.2.4 Non-linear analysis . . . 78
3.2.5 Thermal Analysis . . . 80
3.3 Combined doubler/sub-harmonic mixer . . . 82
3.3.1 Design Topology . . . 82
3.3.2 3D-Model of the Diodes . . . 84
3.3.3 Passive Circuit Design . . . 86
3.3.4 Non-linear analysis . . . 87
3.3.5 Thermal analysis . . . 91
3.4 Fabrication and measurements . . . 92
3.4.1 Local Oscillator . . . 93
3.4.2 Fourth harmonic mixer . . . 93
3.4.3 Combined doubler/subharmonic mixer . . . 97
3.5 Conclusions . . . 100

4 Optoelectronic Transmitter Based on UTC-PD source and Schottky Diodes Frequency Tripler 101
4.1 100 GHz source based on UTC-Photodiode . . . 103
4.2 UMS Schottky Diode . . . 105
4.3 Design procedure . . . 106

4.3.1 Passive circuit designs . . . 107
4.3.2 Non-linear analysis . . . 108
4.3.3 Thermal analysis . . . 110
4.4 Conclusions . . . 111

5 Integrated mixer-multiplier based on GaAs membrane Schottky diodes 113
5.1 Design methodology . . . 114
5.1.1 GaAs membrane Schottky diode technology . . . 114
5.1.2 Topology . . . 115
5.2 Passive circuits design . . . 117
5.2.1 Filters . . . 118
5.2.2 Waveguide probes . . . 118
5.3 Non-linear analysis . . . 120
5.3.1 Load-pull technique . . . 120
5.3.2 Simulation of mixer behaviour . . . 121
5.4 Thermal Analysis . . . 123
5.5 Conclusions . . . 124

6 Conclusions and future work 125
6.1 Conclusions . . . 126
6.2 Conclusiones . . . 128
6.3 Guidelines for future investigation . . . 131
6.4 Pautas para futuras investigaciones . . . 132

Appendices 133

A Photolithography 135

B Prototype dimensions and pictures of the receivers and transmitter 139
B.1 Dimension drawing of the prototypes . . . 140
B.2 Pictures of the fabricated prototypes . . . 145

C Y-Factor Measurement 147
C.1 Attenuator Procedure . . . 149
C.2 Noise-Injection Procedure . . . 150
C.3 Gain Procedure . . . 151

D Triquint Datasheet 153

References **187**

Author's Merit **201**

List of Figures

1.1 Frequency spectrum. 3
1.2 Possibilities of Terahertz communication wireless links: (a) WAN Network and (b) Digital Kiosk. Images obtained from [Fuj15]. . . 4
1.3 (a) Atmospheric attenuation at sea level for different conditions of temperature, relative humidity (RH), fog, dust and rain. (STD: 20 °C, RH 44%), (Humid: 35 °C, RH 90%), (Winter: 10 °C, RH 30%), (Fog, Dust, and Rain: 20 °C, RH 44%). (b) Bit data rate of experimental wireless links for different technologies. Images obtained from [Yan11] and [Duc14]. 5
1.4 Metal enclosure effect for: (a) Standard packaging where cavity resonances and spurious modes propagation exist and (b) gap waveguide packaging where the bed of nails avoids such propagation. 7
1.5 Different implementations of gap waveguides: (a) Groove gap waveguide for which a TE mode propagates (Similar behaviour to a standard rectangular waveguide) and (b) Ridge gap waveguide whose propagating mode is a Quasi-TEM mode (Similar behaviour to a microstrip line). 7
1.6 Schematic of optical-to-THz-Convertor with two laser beams to obtain a Terahertz signal. 8
1.7 Band structure for: (a) p-i-n photodiode and (b) Uni-Travelling-Carrier photodiode. Image obtained from [Car15]. 9
1.8 Normalized response for different PD structures with identical capacitance. Image obtained from [Car15]. 10

1.9 Typical block diagram of a negative resistance oscillator. In some types the NDR device is connected in parallel with the resonant circuit. 12
1.10 Schottky diode equivalent circuit. 14
1.11 Schottky diodes antiparallel configuration [Biu15]. 15
1.12 Schottky diodes antiseries configuration [Biu15]. 16

2.1 Schematic reflection coefficients for a multisection transformer. . 23
2.2 3D geometry of the metallic pin. 24
2.3 3D geometry of the microstrip to standard rectangular waveguide (WR-10) transition: (**a**) microstrip Chebyshev transformer and (**b**) microstrip linear taper. The grey areas correspond to the rectangular waveguide metallic walls. 26
2.4 Side view of the multisection Chebyshev transformer from dielectric filled rectangular waveguide to standard rectangular waveguide. 27
2.5 Top view of the microstrip to dielectric filled rectangular waveguide transition: (**a**) Chebyshev multisection transformer and (**b**) microstrip linear taper. 29
2.6 Performance evaluation of the different parts of the transition: (Solid red line) Linear microstrip to DFRW transition, (Dashed black line) Chebyshev microstrip to DFRW transition and (Star green line) DFRW to rectangular waveguide Chebyshev transformer. (**a**) Reflection (S_{11}); (**b**) Transmission (S_{21}). 31
2.7 The simulation results of the two proposed whole transitions: (Dashed line) Chebyshev impedance transformer and (Solid line) microstrip taper. (**a**) Reflection (S_{11}); and (**b**) Transmission (S_{21}). 32
2.8 Photograph of (**a**) a fabricated back-to-back waveguide block; (**b**) a fabricated microstrip taper in Rogers CuClad. 33
2.9 Setup for the experimental validation of the microstrip-to-waveguide transition. 34
2.10 Simulated performance taking into account the fabricated dimensions (solid line) and measured (dashed line) back-to-back transition. (**a**) Reflection (S_{11}) and (**b**) Transmission (S_{21}). 35
2.11 (a) Perspective view the proposed microstrip to groove gap waveguide (GGW) transition. (b) Explosion view of the microstrip to GGW transition. 37
2.12 Dispersion diagram of the periodic unit cell. 38

2.13 Performance of a direct connection between a gap groove waveguide and a WR-10 rectangular waveguide: (a) Return loss. (b) Insertion loss. 39
2.14 Microstrip to groove gap waveguide transition: (a) Perspective view of the half-split Chebyshev waveguide transformer and (b) Top View. It is important to notice that the microstrip taper touches the metal of the DFGW. 40
2.15 Simulation of the scattering parameters of the microstrip to dielectric filled GGW (solid red line) and the GGW Chebyshev transformer (dashed black line). 41
2.16 (Inset) 3D perspective view of the back-to-back microstrip to standard waveguide transition model for simulation in HFSS. (b) Simulation of the scattering parameters for the microstrip to groove gap waveguide single (solid line) and back-to-back transitions (dashed line). 42
2.17 E-Field distribution of the microstrip to GGW transition at f = 92.5 GHz. 43
2.18 (a) Evaluation of the effect on the transition performance of errors in the fabrication of the metallic pins, given by different values of h. (b) Evaluation of the effect on the misalignment in the z direction, given by different values of mis_z. (c) Evaluation of the effect on the misalignment in the x direction, given by different values of mis_x. (d) Evaluation of the effect on the error in the substrate cutting so that this is longer than nominal, given by different values of tol_z. The dashed line represents the position of the circuit without misalignment error. 44
2.19 Photograph of the fabricated prototype and measurement set-up. (a) Picture of the microstrip line printed on CuClad substrate on the bottom metallic block and on the left the two upper metallic parts. (b) Setup of the back-to-back transition connected to W-Band VDI extenders. 46
2.20 Comparison between simulated (point-dashed blue line), simulation taking into account fabrication errors (solid red line) and measured (dashed green line) back to back transition. 47
2.21 3-D view of the proposed back-to-back microstrip to rectangular waveguide transition model for HFSS simulation. 49
2.22 Perspective view of the structure solved using HFSS eigenmode: (a) Metallic Pin and (b) Groove Gap Waveguide with Rogers CuClad substrate. 49

2.23 Comparison of the propagation constant, β , between groove gap waveguide with different width w and the standard rectangular waveguide. 50
2.24 Evaluation of the cutoff frequency for different waveguide height (b). (Inset) Formula of cutoff frequency where c is velocity of light, m and n are index of the TE_{mn} mode. 51
2.25 Microstrip to standard rectangular transition: (a) Perspective view of the Chebyshev transformer and (b) Top view of the microstrip taper line. 53
2.26 Predicted response by using commercial software HFSS: (a) Microstrip to dielectric filled ridge gap waveguide transition.(b) Dielectric filled ridge gap waveguide to standard WR-10 transition. Insertion Loss (Dashed black line) and Return Loss (Solid red line). 53
2.27 Simulation of the scattering parameters for the microstrip to standard WR-10 single (solid line) and back-to-back transitions (dashed line): (a) Insertion Loss and (b) Return Loss. 54
2.28 Top view of the E-field distribution of the microstrip to WR-10 transition at f = 92.5 GHz. 55
2.29 Photograph of the fabricated structure: (a) Top view of the aluminium metallic block and microstrip circuit. (b) Perspective view of the aluminium metallic block. 56
2.30 Photograph of the assembled and packaged structure connected to the VDI W-Band VNA Extenders. 56
2.31 Comparison between simulated transition taking into account the fabricated value (dashed line) and measured (solid line) back to back configuration: (a) Insertion Loss and (b) Return Loss. . . . 57
2.32 3D perspective view of the microstrip to waveguide transition based on gap waveguide Chebyshev transformer. 58
2.33 Notations of dimensions of the microstrip to waveguide transition: (a) Perspective view of the Chebyshev transformer and (b) Top view of the microstrip to ridge gap waveguide. 60
2.34 Predicted response of the microstrip to waveguide single (solid line) and back to back transition (dashed line): (a) Return Loss and (b) Insertion Loss. 61
2.35 Photograph of the fabricated structure: (a) Top view of the aluminium metallic block and microstrip circuit. (b) Photograph of the assembled back-to-back transition connected to the VDI W-Band VNA extenders. 62

2.36 Comparison between predicted response (solid line), simulation taking into account manufacturing error (dashed-point green line) and measured performance (dashed line): (a) Insertion loss and (b) Return loss. 62

3.1 Basic frequency mixer schematic (left) and graphic description of the downconversion process of the signals presented at the input and output of a fundamental mixer (right). 68
3.2 Schematic of the local oscillator based on Triquint Semiconductor flip chips. The VCO is based on chip TGV2204-FC, the first doubler on TGC4703-FC and the second doubler on TGC4704-FC. 71
3.3 (a) Frequency output versus tuning voltage of the MMIC LO. (b) Picture of the board with MMIC LO PCB with PLL for characterization. (Inset) MMIC LO detail. 72
3.4 3D perspective view of the fourth harmonic mixer. 73
3.5 Schematic of the fourth harmonic mixer with integrated Local Oscillator. 74
3.6 Layers of UMS Schottky Diode. 75
3.7 HFSS model of four diodes in antiparallel configuration. 75
3.8 Top view and predicted response of the fourth-harmonic mixer passive circuits: (a) IF low-pass filter, (b) LO low-pass filter, (c) High-pass filter (d) E-Probe transition between waveguide and microstrip for RF. 76
3.9 (a)Perspective view of the RF low pass filter and waveguide to microstrip transition with the diode interface for impedance matching. (b) Smith Chart with matching representation. Red solid line corresponds to the diode impedance at LO frequency and black line to RF frequency. Black circles are the S_{11} for the waveguide transition with diode interface and red triangles for the LPF with diode interface for different matching line lenghts. 79
3.10 Fourth harmonic mixer predicted performance for different LO power. 80
3.11 Thermal analysis results. 81
3.12 Exploded view of the 3D model of the combined doubler-subharmonic mixer with integrated MMIC based LO. 83
3.13 Schematic of the combined doubler/mixer circuit. 84
3.14 3D illustration of the antiseries diodes used for HFSS simulation of the frequency doubler. 85

3.15 3D illustration of the antiparallel diodes used for HFSS simulation of the subharmonic mixer. 85
3.16 Top view and predicted response of the frequency doubler passive circuits: (a) Low pass filter for DC-Bias, (b) DC-Block 1 for MMIC source, (c) Stepped impedance low pass filter (LPF1) and (d) DC-Block 2 for LO. 86
3.17 Top view and predicted response of passive circuits used in the subharmonic mixer: (a) IF Hammer-head filter, (b) Stepped impedance LPF for RF rejection and (c) RF E-Probe transition between waveguide and microstrip. 88
3.18 Load-Pull analysis results and matching procedure:(a) Doubler frequency multiplier and (b) Subharmonic mixer. 88
3.19 Predicted response of the frequency doubler for different LO input power levels: (a) Output power and (b) Efficiency. 89
3.20 Predicted results of combined frequency doubler/subharmonic mixer for for different MMIC source power levels: (a) Conversion Loss and (b) DSB Equivalent Noise Temperature. 90
3.21 3D illustration of the result of the thermal analysis of the frequency doubler. 91
3.22 Schematic of the Y-Factor setup used for mixer characterization. 92
3.23 Photograph of the MMIC based local oscillator setup and zoom on the Spectrum Analyzer screen showing an example of its output. 93
3.24 Picture of the fourth harmonic mixer printed on Topas COC substrate. 94
3.25 (a) Picture of the fourth harmonic mixer assembled on the metallic housing block bonded to the local oscillator. (b) Picture of the enclosed mixer block ready for measurement. 94
3.26 Y-Factor setup for fourth harmonic mixer characterization. . . . 95
3.27 Comparison of the simulated and experimental performance of the fourth harmonic mixer for an Intermediate Frequency, IF = 2 GHz. 95
3.28 Comparison of the simulated and experimental performance of the fourth harmonic mixer for an Local Oscillator, LO = 75 GHz, sweeping the IF. 96
3.29 Pictures of the subharmonic mixer: (a) Subharmonic mixer printed on Topas COC without IF and LPF for DC bias filters. (b) Harmmerhead filter for IF and (c) LPF for DC Bias. 97

3.30 Photograph of the subharmonic mixer mounted in the metallic housing block: (a) MMIC source and doubler/subharmonic mixer with inset of the UMS diodes. (b) Enclosed housing metallic block. 97
3.31 Setup for Y-Factor measurement where the board with Arduino Due for IN tuning can be observed. 98
3.32 (a) Measured conversion loss and (b) Measured equivalent noise temperature of the combined doubler/subharmonic mixer and its comparison with predicted performance for a fixed IF = 2 GHz. . 98
3.33 Comparison of the simulated and experimental performance of the combined doubler/harmonic mixer for a MMIC source frequency, f_{IN} = 75.5 GHz, sweeping the IF. 99

4.1 (a) Block diagram of the 300 GHz optoelectronic transmitter based on UTC-PD and Schottky diode technology. (b) 3D view of the whole transmitter. The top metallic block is shown with transparency in order to see the substrate and the bottom metallic part. 102
4.2 (a) 3D perspective view of the integrated UTC-PD to tripler passive circuit; (b) Close view of the UTC-PD 50 Ω coplanar structure excited by a discrete port providing the input signal; (c) Simulated frequency response. 103
4.3 Perspective view of the balance configuration of Schottky diodes. 105
4.4 Scheme of the integrated photodiode and Schottky diode frequency tripler. 106
4.5 Passive circuits: perspective view and simulations. (a) Bias-T, (b) LPF for IN signal, (c) LPF for DC bias and (d) Waveguide transition. 107
4.6 Load-Pull analysis results and matching procedure for the balanced configuration performing antiparallel pair of Schottky diodes. 108
4.7 3D perspective of the transmitter model used for simulation. . . 109
4.8 Performance of the photodiode fed frequency tripler. a) Efficiency and b) output power. 109
4.9 Thermal analysis of the multiplier Schottky diodes. 110

5.1 Antiparallel configuration of Schottky diodes. 115
5.2 Schematic of the integrated tripler-mixer. 115

5.3 Top view and predicted response of the passive components of the sixth harmonic mixer. (a) Stepped impedance LPF for IF; (b) Waveguide transition for IN; (c) LPF for IN; (d) High pass filter for LO; (e) LPF for LO; and (f) waveguide transition for RF. 117
5.4 Load-pull analysis results. (a) Tripler: Red solid line corresponds to the diode embedding impedance at IN frequency and black solid line at LO frequency. (b) Mixer: Red solid line corresponds to the diode embedding impedance at LO frequency and black solid line to RF. The dots correspond to the obtained values of embedding impedance. 120
5.5 3D view of the integrated tripler/mixer used for simulation. . . . 121
5.6 Conversion Loss and Equivalent Noise Temperature for different levels of input power. 122
5.7 Thermal analysis of the Schottky diodes for: (a) 30 mW and (b) 20mW. 123

A.1 Schematic of the photolithography procedure at the Public University of Navarra's facilities. 135
A.2 Pictures of the: (Left) Dicing Saw DAD321 and (Right) TPT HB16D die bonder. 137
A.3 Welded diodes.(Left) Antiseries Schottky Diodes configuration for doubler multiplier. (Center) Antiparallel Schottky Diodes for subharmonic mixer. (Rigth) Balance diodes featuring antiparallel configuration for the tripler multiplier. 137
A.4 I-V measured curve of an UMS Schottky diode. 137

B.1 Layout and dimensions of the fourth harmonic mixer. 141
B.2 Layout and dimensions of the combined doubler/sub-harmonic mixer. 142
B.3 Layout and dimensions of the frequency tripler multiplier. 143
B.4 Layout and dimensions of the integrated tripler/subharmonic mixer layout. 144
B.5 Pictures of the fourth harmonic mixer fabrication. (a) Tee for the local oscillator; (b) Waveguide E-Probe transition; (c) Low pass filter and (d) Hammerhead filter. 145
B.6 Pictures of the doubler of the subharmonic mixer fabrication. (a) DC-Block for LO; (b) Low pass filter for DC feed; (c) Low pass filter for LO and (d) DC-Block for 2×LO. 145

B.7 Pictures of the subharmonic mixer fabrication.(a)Hammerhead filter for IF frequency; (b) Low pass filter for 2×LO and (c) Waveguide E-probe transition. 146

C.1 Y-Factor variables (Image obtained from [Roh12]). 148

List of Tables

2.1 Dimensions of the Chebyshev transformer waveguide sections (μm). 30
2.2 Dimension of the microstrip to DFRW linear taper transition (μm). 30
2.3 Dimension of the microstrip to DFRW Chebyshev transition (μm). 31
2.4 Dimensions of the unit cell (metallic pin) of the bed of nails (μm). 37
2.5 Dimensions of the transition (μm). 40
2.6 Dimension of metallic pin (μm). 50
2.7 Dimensions of Chebyshev transformer waveguide sections and microstrip line (μm). 52
2.8 Dimensions of the transition (μm). 59
2.9 Performance of millimeter wave rectangular waveguide to microstrip transitions. 65

3.1 State of the art of fourth harmonic Schottky diode mixers working at frequencies similar to this work. 80
3.2 State of the art of Schottky diode subharmonic mixers working at similar frequencies to this work. 90
3.3 State-of-the-art of Schottky diode mixers working at similar frequencies to this work. 100

5.1 Layers of GaAs membrane Schottky diodes. 114

Abbreviations and Acronyms

ADS	Advanced Design System
AMC	Artificial Magnetic Conductor
CL	Conversion Loss
CNC	Computer Numerical Control
DFRW	Dielectric Filled Rectangular Waveguide
DSB	Double Side Band
ENT	Equivalent Noise Temperature
GGW	Groove Gap Waveguide
HBT	Heterojunction Bipolar Transistor
HBV	Heterostructure Barrier Varactor
HEMT	High Electron Mobility Transistor
HFSS	High Frequency Structure Simulator
IF	Intermediate Frequency
IL	Insertion Loss
LO	Local Oscillator
MMIC	Monolithic Microwave Integrated Circuits
NDC	Negative Differential Conductance
NLO	NonLinear Optical
PLL	Phase-Locked Loop
PMC	Perfect Magnetic Conductor
QCL	Quantum Cascade Laser
RF	RadioFrequency
RGW	Ridge Gap Waveguide
RL	Return Loss
RTD	Resonant Tunnelling Diode
TE	Transverse Electric
TEM	Transverse Electromagnetic
UMS	United Monolithic Semiconductors
UTC-PD	Uni-Travelling-Carrier Photodiode
VCO	Voltage-Controlled Oscillator

Chapter 1

Introduction

For future THz applications new compact, flexible and portable receivers and transmitters are needed. In particular, for the development of Beyond 5G next generation mobile communication system networks, THz frequency signal sources must be not only compact, which implies reduced cost, but also work at room temperature and have potential for integration. All these characteristics can only be obtained if novel schemes as well as new packaging concepts are developed.

In this thesis, **the main goal** consists in the design of integrated and compact receivers and transmitters based on Schottky diode technology for future THz instruments and applications.

Concretely, the following **specific objectives** have been set:

- Development of a simple design procedure based on Chebyshev transformer theory for analytical design of inline transitions from planar to waveguide technology.
- Study and development of packaging techniques in order to achieve more simplified, compact and easier assembly inline transitions from planar to waveguide based technology.
- Development of compact integrated receiver configurations. This includes:
  - Design of harmonic mixers-receivers with integrated MMIC based Local Oscilator.

  - Design of combined tripler/mixer working at 600 GHz, based on GaAs membrane technology since the discrete flip-chips are not a good option for devices working beyond 300 GHz.

- Development of a compact transmitter configuration combining photonic and electronic components.

In order to achieve these goals, the **main tasks** that have been realized during this thesis include:

- Study and design of the different circuits presented in this thesis by means of commercial software simulations.
- Fabrication of most of the components by means of the standard photolithography process at Public University of Navarra's facilities.
- Measurement and validation of the prototypes.

Finally, the **main novelties** presented in this thesis can be summarized basically in two points:

- Development of a very simple design procedure for inline planar to waveguide transition, which has been applied to different waveguiding technologies.
- Introduction of integrated designs that can be a good starting point for future THz devices, concretely, for receivers and transmitter.

1.1 Brief introduction to THz communications

Terahertz waves or sub-millimetre waves refer to the electromagnetic part of the spectrum between 100 GHz and 10 THz, i.e. the region situated between the microwave and the infrared frequencies (see Figure 1.1). This THz frequency range lays on the borderline of the electronic world, where generation uses methods based on radio and microwave techniques, and the photonics realm, where optical techniques are employed. But for a long time, this frequency range has been known as the THz gap due to the lack of devices, mainly sources, able to work at such frequencies.

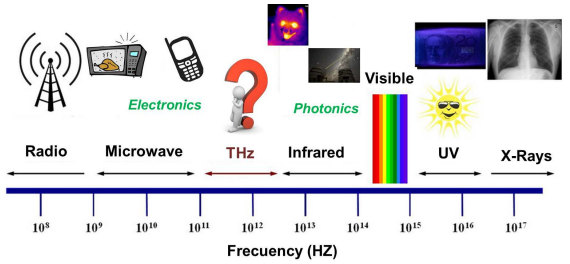

Figure 1.1: Frequency spectrum.

However, nowadays it has become a frequency band of great interest due to the multiple possibilities it presents. That is why during the last decades and thanks to the advances and progress in high-frequency photonic and electronic technologies, the development of these THz devices and systems has been enabled [Tak78, Rai80, Arc81, Arc84, Eri85, Pag85, PG86]. There are two alternatives for the moment in order to create a THz system. One of them consists in starting from an electronic source and then upscale in frequency; the second one is based on using photonics sources and then downscale in frequency.

Another indicator that THz technology is being an active scientific field is the fact that the number of publications is increasingly rapidly. Among all the applications in which they are getting interest, they have demonstrated to be very useful for:

- **Automotive Radar** [Has12, Fol05].
- **Terahertz imaging**, e.g, monitoring the moisture level of a leaf [Yuj03].
- **Security**, e.g, to detect illegal substances in airports [She01].

- **Medical**, e.g, detection of epithelial cancer [Woo03].
- **Radioastronomy**, e.g, beginning of new star formation [Tor17].
- **Communications**, e.g, high data rate wireless links [Pan15, Nag16].

In this thesis we focus on the integration, packaging and development of compact transmitter and receiver devices in the THz frequency range. The main aim of this compactness is focused on communication applications for high data rates links, which are taking more relevance everyday since, according to Edholm's law, telecommunications data rates are as predictable as Moore's law, i.e., the demand for point-to-point bandwidth in wireless communications doubles every 18 months [Che04]. Their applications could be, for example, ultra fast connections for WAN networks or digital kiosks to buy digital media contents instantaneously (Figure 1.2).

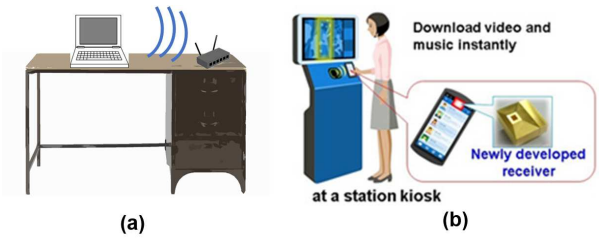

Figure 1.2: Possibilities of Terahertz communication wireless links: (a) WAN Network and (b) Digital Kiosk. Images obtained from [Fuj15].

Wireless communication links below 100 GHz require compression algorithms and new sophisticated schemes, such as Multiple Input Multiple Output (MIMO) systems, to make the links more efficient. However, they are becoming saturated and the only solution consists on wider bandwidth links. The technologies between 10 THz and 100 THz provide a large available bandwidth; however, they are not useful for communications. The reasons are the ultra-low power forced by the eye-safety limits for human beings [Hea98, Koc07], in addition to the high propagation attenuation, which makes it almost impossible to stablish a wireless link even at normal atmospheric conditions ($20°C$ *and* *relative humidity* 40%). Nonetheless, THz radiation is non-ionizing, i.e safe for human beings, and using carriers at THz frequencies implies very wide bandwidths, which are able to provide very high data rates.

Furthermore, these links present other advantages, such as the possibility of creating secure links. That is why the use of the THz and sub-millimetre wave range for broadband communication links [Aky14] is getting so much relevance. Although at THz there is also atmospheric attenuation, there are many propagation windows that can be used for communications, as we can see in Figure 1.3(a). In this figure the power attenuation taking into account different seasonal temperatures as well as the effects of fogs, dust and rain is represented against the frequency. It is remarkable that the attenuation changes significantly due to weather and seasonal variations in humidity, what makes these links highly dependent on weather conditions.

Recently, several transmission experiments using different technologies, i.e. optical sources, electronic sources (multipliers) and resonant tunnelling diodes (RTDs), have been carried out where the data rate has been higher than 10 Gbps, 40 Gbps and even 100Gbps [Son11, Hir06, Nag13, Duc14, Xia16, Rod18, Jia18]. A summary picture with some reported experiments is shown in Figure 1.3(b).

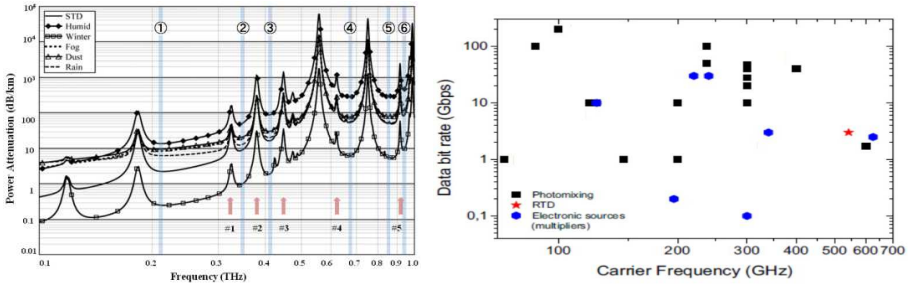

(a) (b)

Figure 1.3: (a) Atmospheric attenuation at sea level for different conditions of temperature, relative humidity (RH), fog, dust and rain. (STD: 20 °C, RH 44%), (Humid: 35 °C, RH 90%), (Winter: 10 °C, RH 30%), (Fog, Dust, and Rain: 20 °C, RH 44%). (b) Bit data rate of experimental wireless links for different technologies. Images obtained from [Yan11] and [Duc14].

It can be seen that both photonics and electronic systems are developed to the achieve high data bit rates. The best performance has been achieved by combination of photonic systems at emission, because of their high bandwidth, and electronic receivers, due to their linearity and high sensitivity [Duc15].

1.2 Background

1.2.1 Introduction to Packaging

Electronic packaging is the final stage of devices manufacturing. This process is necessary in order to avoid the physical damage and corrosion of PCB circuits. Furthermore, packaging is important to protect the circuit not only from enviromental hazards but also from mechanical stress that components may suffer. Since 1970, when the military used ceramic flat packs in order to package integrated circuits, electronic packaging has largely evolved. The recent developments consist in integrating multiple dies in a single package, called system in package, or three-dimensional integrated circuit. Apart from that, it also happens that among the components in development at submilliter and terahertz frequencies, those in planar technology are becoming increasingly relevant [Lyn08, Reb11]. However, given the lack of connectors at sub-millimetre and terahertz frequencies, most test equipment is waveguide-based. In addition, integration of planar circuits with waveguide components, e.g. horn antennas, makes transitions between planar transmission lines and waveguide indispensable. That is why the development of efficient packaging techniques for these applications, which allows integration of microstrip and waveguide based components has become essential. Beside the fact that working at terahertz and millimetre waves, similar to what happens at microwaves, RF packaging is also important to isolate the circuits from external interferences. However, standard enclosing is liable to create resonant cavities and destructive electromagnetic interferences with metallic walls, which produce additional losses, standing waves and interference between components or croostalk, if not properly controlled.

Recently, a novel approach for packaging has been proposed, based on the so-called bed of nails [Raj11]. These are periodic metallic structures which constitute an artificial magnetic conductor (AMC) which emulates the behaviour of a perfect magnetic conductor (PMC). This structure involves a very high impedance that avoids the propagation of electromagnetic waves in a certain frequency range. Thanks to this property they have found its application for parasitic mode suppression in packaging [Raj10, Raj13, Zam14, Reb14, Shi17]. A representative picture where the gap waveguide benefits in packaging is shown in Figure 1.4. In Figure 1.4(a) it is shown that the standard metal enclosure can provoke resonances and the spurious radiation of the microstrip can also propagate, which can deteriorate the final behaviour of the circuit. In Figure 1.4(b) the bed of nails avoids such propagation with the consequent improvement.

But gap waveguides are used not only for packaging but also to create new

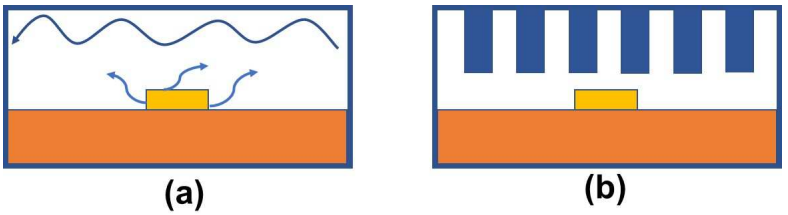

Figure 1.4: Metal enclosure effect for: (a) Standard packaging where cavity resonances and spurious modes propagation exist and (b) gap waveguide packaging where the bed of nails avoids such propagation.

types of waveguides, see Figure 1.5. In this type of transmission line the field propagates along metal grooves (1.5(a)) or ridges (1.5(b)). For the case of groove gap waveguide the propagation is similar to that in a standard rectangular waveguide, i.e., the TE_{10} mode propagates. Conversely, ridge gap waveguides emulate microstrip line and their fundamental propagation mode is quite similar to the Quasi-TEM mode [Raj11].

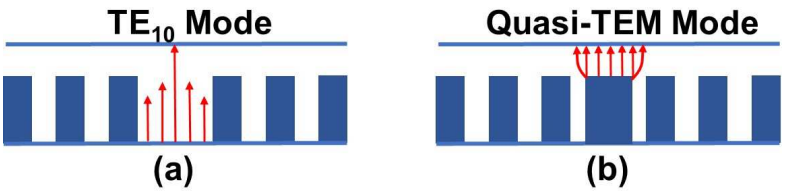

Figure 1.5: Different implementations of gap waveguides: (a) Groove gap waveguide for which a TE mode propagates (Similar behaviour to a standard rectangular waveguide) and (b) Ridge gap waveguide whose propagating mode is a Quasi-TEM mode (Similar behaviour to a microstrip line).

1.2.2 Terahertz Photonic Sources

The Terahertz gap is getting reduced due to the great advance and progress on the development of sources at this frequency range. From the photonic point of view there are three well-studied options for THz generation. One purely optical terahertz source is based on molecular gas lasers [Cru07]. These lasers

can achieve peak power up to megawatts at frequencies ranging from 300 GHz to 10 THz. Nevertheless, they are bulky and expensive, therefore, unattractive for industrial applications. Another interesting solution emerged in the early 1990s and helped boosting THz technology. It consists in photonic generation of THz waves based on optical-to-THz conversion devices with use of lasers. Finally, Quantum cascade lasers (QCLs) represent a very promising technology for THz generation [Lin16].

Among them, the most usual method at room temperature is the optical-to-THz signal conversion. Its operational principle for THz photonic generation consists of beating two laser beams whose difference in frequency is a THz signal. Both lasers are absorbed by the optical device and produce an AC current signal at the difference frequency. Figure 1.6 shows schematically the optical-to-THz conversion using interaction media such as nonlinear optical (NLO) materials, photoconductors and photodiodes [Car15, Nag11].

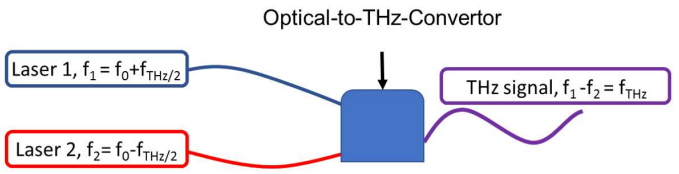

Figure 1.6: Schematic of optical-to-THz-Convertor with two laser beams to obtain a Terahertz signal.

Nonlinear optical (NLO) materials

Nonlinear optical (NLO) materials have achieved a lot of interest for THz generation, since the intensity and conversion efficiency has increased during the last few years. The development of new techniques for fabrication and growth of artificial materials have contributed to this evolution.

There are two approaches in order to generate this THz frequency; one of them consists in generating "pulsed waves" by means of injecting lasers pulses into the NLO materials. The other one is to use difference frequency generation in the NLO materials to generate Terahertz waves. Typical NLO materials are crystals with large nonlinear susceptibility such as cadmium telluride (CdTe), zinc telluride (ZnTe), gallium phosphide (GaP), lithium niobate ($LiNbO_3$) and DAST crystal.

Photodiodes

Photodiodes are very convenient for the advance in the development of communication wireless links accessible to everybody, insomuch as they are able to provide THz signals avoiding bulky and expensive lasers.

Currently two different kind of devices can be found: p-i-n photodiodes and Uni-Travelling-Carrier photodiodes (UTC-PD). Their different band structure can be seen in Figure 1.7.

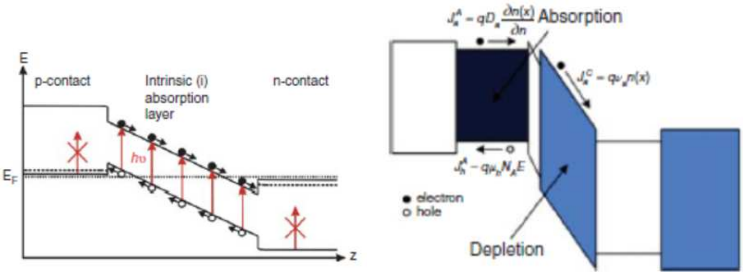

(a) (b)

Figure 1.7: Band structure for: (a) p-i-n photodiode and (b) Uni-Travelling-Carrier photodiode. Image obtained from [Car15].

The photoresponse of a UTC-PD is determined only by the electron transport in the whole structure. However, in the pin-PD both electron and holes contribute to the response current, and the low-velocity hole-transport determines the total performance. Therefore, due to the higher electron velocity UTC-PD is a better option for THz frequencies [HI07]. Furthermore, it has been demonstrated that the output level of UTC-PDs is about 20 dB higher than the p-i-n PDs output at 100 GHz [Son15].

The important parameters to characterize photodiodes are:

- Bandwidth
- Responsivity
- Roll-off
- Saturation power

All these parameters can be summarized by the efficiency of conversion of light into THz signal as follows.

$$\eta_{THz} = P_{max_{THz}}/P_{opt}^2 \tag{1.1}$$

The bandwidth is limited by two factors, electrical limit and transit time-related, as shown in equation 1.2, where the output power is a function of the frequency.

$$P(f) \propto \frac{1}{1+(\frac{2\pi W_d f}{3.5\bar{v}})^2}\frac{1}{1+(2\pi RCf)^2} \tag{1.2}$$

where

$$\bar{v} = \sqrt[4]{\frac{2}{\frac{1}{v_e^4}+\frac{1}{v_h^4}}} \tag{1.3}$$

f is the frequency, W_d is the thickness of the depletion layer,R and C are the total resistance and capacitance, v_e and v_h are the electron and hole velocities in the drift zone W_d.

The saturation power is mostly limited by the space charge and power distribution. Responsivity and roll-off are improved by means of travelling wave UTC-PD (TW-UTC-PD) devices. A normalized response for different PD structures with identical capacitance is shown in Figure 1.8.

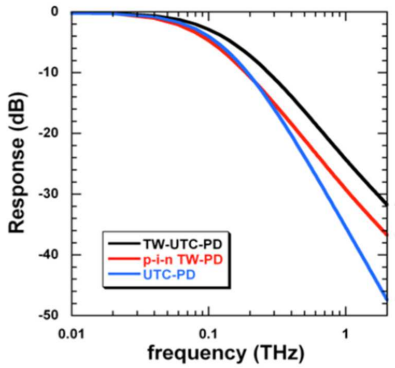

Figure 1.8: Normalized response for different PD structures with identical capacitance. Image obtained from [Car15].

This figure shows the great advantage of using TW-UTC-PD and the better responsivity of UTC-PD over p-i-n photodiodes until 300 GHz. However, it is

remarkable to say that this analysis does not take into account the enhancement in terms of saturation power that a UTC-PD can offer. In conclusion, TW-UTC-PD yields a better performance than UTC-PD and p-i-n photodiodes at the expense of more complicated fabrication. Between UTC-PD and p-i-n photodiodes the performance is similar; however, until 300 GHz UTC-PD presents better responsivity.

Quantum Cascade Lasers

Quantum cascade lasers (QCL) are lasers that emit in the mid-to-far infrared part of the electromagnetic spectrum. The operational principle is based on intersubband transitions in quantum wells. The first QCL was demonstrated in 1994 [Fai94] using intersubband transitions in a superlattice of semiconductor multiple quantum well heterostructures. The key feature of this kind of structure in cascade is that a single injected electron can emit many photons, which allows for differential quantum efficiencies greater than unity. Furthermore, QCL are the most compact and high-powered coherent THz sources. That is why they are very useful for spectroscopic applications. However, it is very difficult for THz QCLs to operate at room temperature.

1.2.3 Electronic Sources

Although optical sources have been dominating THz frequency generation for a long time, recently electronic sources are getting more interest and expanding its boundaries. Nowadays, there are three studied approaches for this kind of sources: transistor-based sources, diode-based sources and frequency multiplication [Rie14, Eis10].

Transistor-based sources

MMIC local oscillators at THz can be realized with transistor-based oscillators and amplifiers. The active elements can be high electron mobility transistors (HEMTs), heterojunction bipolar transistor (HBT; SiGe or III-V devices) and field effect transistors (FETs) [Urt17, J. 16].

The main barrier for transistors to generate THz has been their cutoff frequency. However, thanks to innovation on materials and the advances in semiconductor research, this cutoff frequency has been significantly increased. This fact has allowed THz generation by means of transistors up to 500 GHz and for those devices based on SiGe Heterojunction Bipolar Transistor (HBTs) 1 THz

has been achieved [Sch18b]. The main advantage of this kind of generation over diode based devices is the availability of gain.

Diode-based sources

For a long time diode-based devices have been considered as millimetre-wave and sub-millimetre-wave sources. The most employed ones are Gunn diodes, IMPATT (IMPAct ionization Transit Time) diodes and Resonant Tunneling Diodes (RTDs) [Cha11]. These are negative-resistance oscillators whose typical block diagram is shown in Figure 1.9. The equivalent model consists in a resonant circuit, usually a LC tank, connected to a device with a negative differential resistance (NDR). The operational principle is the negative resistance of the active device (diodes in this case) cancelling the loss resistance of the loaded resonator. Thus, a circuit with zero differential resistance producing spontaneous oscillations is created. The main difference between them arises from how they obtain the NDR.

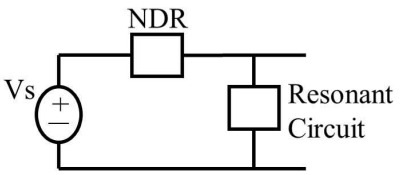

Figure 1.9: Typical block diagram of a negative resistance oscillator. In some types the NDR device is connected in parallel with the resonant circuit.

Gunn diodes are frequently found from III-V compound semiconductor. The operation of this diode is as simple as applying a DC voltage to bias the device into its negative resistance region. Gunn diodes are widely used for microwave region devices and new Gallium Arsenide Gunn diodes are made for frequencies up to 200 GHz.

IMPATT diodes achieve NDR from time delays caused by the avalanche breakdown and carrier transit across the device. Compared to other kinds of NDR diodes, IMPATT based generators achieve much higher output power levels. Besides, they have been proved to be one of the most reliable and stable microwave sources. However, it is difficult to obtain those advantages for frequencies over 150 GHz.

Resonant tunnelling diodes (RTDs) are double-barrier tunnel semiconductor structures. Tunnelling diodes make use of quantum mechanical tunnelling.

The mechanism of electron transport through the barriers is resonant tunnelling through the quantized subbands in the quantum well. RTDs have a very particular I-V curve with a negative-differential-conductance (NDC) region with a very fast process; therefore, RTDs can operate at very high frequencies.

Frequency Multipliers Chains

In general, diode or transistor based sources have limited bandwidth and are bulky and expensive. Besides, they are not able to provide high power or are limited to frequencies below 150 GHz.

Therefore, planar frequency multipliers are one of the best options insomuch as they have greatly improved their bandwidth and efficiency during the last few years. These frequency multipliers are nonlinear devices that generate a specified harmonic of the input signal [War04]. Frequency multiplication devices can generate such harmonic frequency thanks to a variable capacitance (e.g. heterostructure barrier varactors (HBVs)) or variable resistance (e.g Schottky diodes). Those devices based on variable capacitance present better efficiency and power handling than variable resistance devices.

Nonetheless, when the order of the harmonic is high, i.e. more than four or five times the source frequency, individual devices are not a good solution since the higher the harmonic generated the higher the losses associated to that generation. Therefore, when very high frequencies are needed, the solution is a combination of doublers and triplers (cascade of multipliers). Because of the simplicity of fabrication process, Schottky diodes are the preferred device for building frequency multiplier chains.

Schottky diode technology

The Schottky diode, named after the physicist Walter Schottky, is a semiconductor diode formed by the junction of a semiconductor and a metal. This component has as main characteristic that it works with low forward voltage, which, in addition to its fast switching, makes it a good candidate for working at high speed and high frequency [Mae10]. For practical reasons, there are four types of Schottky diodes depending on the barrier height: high barrier, medium barrier, low barrier and Zero Bias barrier. The first three types are made with n-type Silicon and the appropriate metal; Zero Bias diodes are traditionally built with p-type Si semiconductor material, although recently the trend is to fabricate them using the n-type semiconductor InGaAs. Finally, there are also Gallium Arsenide diodes that are fabricated with n-type semiconductor only

and metal.

The general equivalent circuit of a Schottky diode can be seen in Figure 1.10 and its modelling equation of the current for a Schottky junction, regardless of the technology in which it has been implemented is:

$$I = I_{sat}\left(e^{\frac{q(V-IR_s)}{nkT}} - 1\right) \tag{1.4}$$

where
k = Boltzmann's constant, $1.38044 \times 10^{-23} J/K$
q = electron charge, $1.60206 \times 10^{-19} C$
T = absolute temperature, K
R_s = series resistance, Ω
I_{sat} = saturation current, A
η = ideality factor
and

$$I_{sat} = AA^{**}e^{(\frac{-q\Phi_b}{KT})} \tag{1.5}$$

where
A = effective diode area, cm^2
A^{**} = modified Richardson constant, $(A/K)^2/cm^2$
Φ_b = barrier height, V

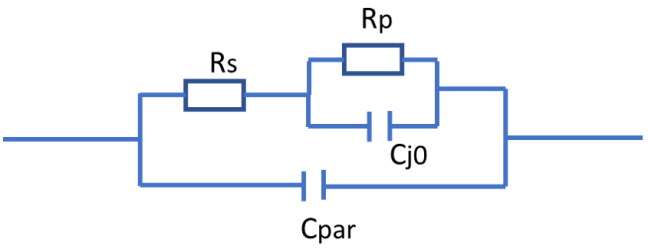

Figure 1.10: Schottky diode equivalent circuit.

An important parameter that determines the operational frequency is the cutoff frequency. The cutoff frequency is computed as the frequency at which the reactance of the diode equals the series resistance:

$$f_c = \frac{1}{2\pi R_s C_j}. \tag{1.6}$$

The junction capacitance is determined by the physical dimension of the junction and the doping profile of the semiconductor layer:

$$C_j(V_R) = \frac{C_j(0)}{(1 - \frac{V_R}{V_i} - \frac{kT}{q})^{1/2}} \tag{1.7}$$

where
$C_j(V_R)$ = junction capacitance at reverse bias voltage V_R
$C_j(0)$ = junction capacitance with $V_R = 0$
V_i = internal contact potential

and the series resistance R_S is the addition of the resistance due to the epitaxial layer and the resistance due to the substrate $R_S = R_{epi} + R_{sub}$ [Cor09].

Depending on the application, and therefore, on the harmonic we would like to obtain, there are different diode configurations that provide us a better efficiency for each case [Maa03].

- **Antiparallel configuration**

  The antiparallel configuration is shown in Figure 1.11.

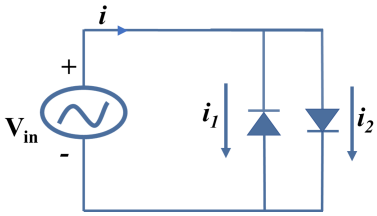

Figure 1.11: Schottky diodes antiparallel configuration [Biu15].

We can simplify the current of the diodes $i = i_{sat}(e^{\frac{q(V-IR_s)}{nkT}} - 1$ as $i = i_s(e^{\alpha V_{in}} - 1)$. Besides, if we define $i_1 = f(V_{in})$, then $i_2 = -f(-V_{in})$. Thus, the output current will be:

$$i_{out} = i_1 + i_2 = i_s(e^{\alpha V_{in}} - 1) - i_s(e^{-\alpha V_{in}} - 1) = 2i_s \sinh(\alpha V_s cos(\omega_s t)) \tag{1.8}$$

Applying Taylor's approximation

$$sinh(V) = V + 1/6V^3 + 1/120V^5 + \dots \tag{1.9}$$

and the final output is

$$i_{out} = A_1 i_s V + A_2 i_s V^3 + A_3 i_s V^5 + \dots \tag{1.10}$$

If the input is a tone $V_{in} = V_S cos(\omega_s t)$, the output

$$i_{out} = Acos(\omega_s t) + Bcos(3\omega_s t) + \dots \tag{1.11}$$

is an efficient frequency tripler multiplier where the even harmonics are cancelled by the antiparallel configuration itself and higher efficiency is obtained in the odd harmonics.

On the other hand, if the input is a sum of two tones $V_{in} = V_1 cos(\omega_1 t) + V_2 cos(\omega_2 t)$, then the output will be

$$i_{out} = \dots + Acos^2(\omega_1 t)Bcos(\omega_2 t) + \dots + Acos^4(\omega_1 t)Bcos(\omega_2 t) + \dots \tag{1.12}$$

which provides an intermediate frequency either $F_{IF} = 2\omega_1 - \omega_2$ or $F_{IF} = 4\omega_1 - \omega_2$ which is a good solution for subharmonic and fourth harmonic mixing, respectively.

- **Antiseries configuration**

  Due to the circuit symmetry we can also have the antiseries configuration shown in Figure 1.12.

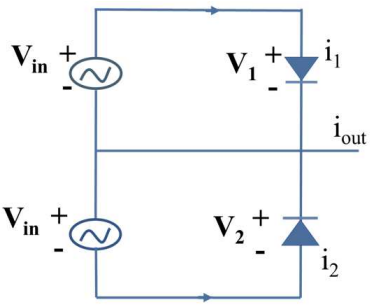

Figure 1.12: Schottky diodes antiseries configuration [Biu15].

We can analyse the output node and we obtain

$$i_{out} = i_1 + i_2 \tag{1.13}$$

where, according to the equations described previously in this section

$$i_1(V) = A_1V + A_2V^2 + A_3V^3 + A_4V^4 + \dots \tag{1.14}$$

and

$$i_2(V) = i_1(-V) = -A_1V + A_2V^2 - A_3V^3 + A_4V^4 + \dots \tag{1.15}$$

therefore

$$i_{out} = 2A_2V^2 + 2A_4V^4 + \dots \tag{1.16}$$

That is why the antiseries configuration is a good solution for doubler frequency multiplier, since on the contrary of the antiparallel configuration, in this case the odd harmonics are cancelled and the even harmonics are more efficient.

1.3 Motivation and thesis outline

As it has been previously said, new compact, flexible and portable devices are going to be necessary for future THz applications. In particular, for the development of new generation of mobile communication and satellite applications, where the reduced compact size, which implies lower cost, is an important factor to be taken into account.

The work presented in this thesis is focused on the development of submillimetre and terahertz wave band components and packaging techniques. The main novelty of this thesis consists in the integration of different components on the same substrate and housing metallic block. This way the prototypes designed present the advantage of being more compact, of reduced weight and, thus, more useful for communication systems.

The content of the thesis is divided into six chapters.

- **Chapter 1** In this chapter a brief introduction of the state-of-the-art of terahertz and millimetre wave systems for communications is made. Besides, it gives a general introduction to packaging technology, photodiodes and Schottky diodes technologies.

- **Chapter 2** describes the different designs that have been realized during this thesis for packaging and integration of planar technology and waveguide components, all of them based on an analytic procedure. Firstly, a simple inline transition between microstrip and rectangular waveguide is presented. Secondly, an inline transition between microstrip and groove gap waveguide is analysed and measured. Afterwards, a design for microstrip to rectangular waveguide transition using bed of nails and gap waveguide with very simple assembly procedure is presented. Finally, the last studied transition is an even more simplified design and with simpler assembly process than previous design.

- **Chapter 3** presents the development of two receivers with integrated MMIC based LO: a fourth harmonic mixer and a subharmonic mixer designed on a combination of planar and waveguide technology. Both mixer prototypes are based on Schottky diode flip-chips with antiparallel configuration. The main novelty of the fourth harmonic mixer consists in the integration of the local oscillator and the mixer in the same housing metallic block with the implication of a reduced weight and cost. On the other hand, the subharmonic mixer presents the main novelty of integrating not only the local oscillator in the same block but also a frequency doubler

together with the mixer in the same substrate, performing, in terms of frequency conversion, as a fourth harmonic mixer. Both configurations are very convenient, since they reduce the LO power requirements.

- **Chapter 4** studies a THz transmitter which integrates a photodiode source and a frequency tripler multiplier based on flip-chip Schottky diode technology. The goal of this chapter is the design of a compact broadband terahertz transmitter working at 300 GHz for communication systems.

- **Chapter 5** deals with the integration of a tripler frequency multiplier and a subharmonic mixer in the same substrate working at 600 GHz. This way a sixth harmonic mixer with the behaviour of a subharmonic mixer is achieved. Schottky diodes are integrated in a Gallium Arsenide membrane substrate alongside all the necessary circuitry.

- **Chapter 6** summarizes and draws conclusions of the whole work presented in this thesis and proposes future research lines that could be followed.

Chapter 2

Inline Transitions from Planar to Waveguide Technology at W-Band

As has already been commented in the introduction to packaging, planar transmision line to waveguide transitions have become essential for the integration of devices developed in planar technology and those components developed in waveguide. Different types of microstrip-to-waveguide transitions can be found in the literature. Among them, the E-plane probe is the most common. This transition is based on a microstrip line introduced through an aperture in the E-Plane of a rectangular waveguide that couples the quasi-TEM mode of the microstrip line to the TE_{10} mode of the waveguide [Leo99, Row10, Li13, Zam16].

Some of these transitions have been presented operating in the full W-Band [Row10, Zam16], and feature insertion loss (IL) as low as 0.4 dB, typically around 1 dB. However, in order to avoid higher order mode excitation, they require a very narrow channel to introduce the microstrip probe. Moreover, in E-plane probe transitions, the input port is usually perpendicular to the output port. This fact can make integration of devices or antennas a cumbersome task, as a consequence additional bent sections are required. Furthermore, the behaviour of the transition is very sensitive to the position of the microstrip substrate with respect to the waveguide, in such a way that small errors during the fabrication process may produce large disagreements between simulation and experimental results. This problem repeats in other transitions based on radiating elements such as quasi-Yagi antennas [Kan99] and slotline antennas

[Yan10].

On the other hand, the quasi-TEM microstrip mode can be easily coupled to the TE_{10} rectangular waveguide mode by means of an inline configuration in which the field propagation direction in the waveguide is the same as in the microstrip line[Yao94, Bou09, Zha10, Sim18, Li18, Sch18a, Reb15]. In the W-band, this concept was used in [Reb15], where waveguide matching sections partially filled with dielectric were used. These sections were based on the gradual reduction of the dielectric material inside the waveguide. Therefore, they must be numerically optimized and, in addition, complicate manufacturing and assembly. A similar approach was followed in [Gra17], where the band was extended at the expense of an increase of the number of sections. This length can be reduced by using a cavity excited by a microstrip probe [Zam17], but the design requires full-wave optimization.

In this work inline microstrip to waveguide transitions have been realized in a simple way so that the manufacturing process and assembly is not complicated. Besides, the full-optimization is avoided by means of computing the dimension theoretically based on Chebyshev transformer and small reflections theory. The first transition presented in this project consists of an inline microstrip to standard WR-10 transition. The disadvantage of this model is that the waveguide has a H-plane split, what makes the manufacturing and assembly difficult. This problem can be alleviated by using Perfect Magnetic Conductor (PMC) lids [Zam16], allowing for wide microstrip substrates, although at the expense of increased manufacturing complexity. The rest of the transitions described in this chapter are based on this concept. One of them is a microstrip to groove gap waveguide compatible with WR-10 standard waveguide. The other one is a microstrip to standard WR-10 transition by means of ridge and groove gap waveguide. The last one is also a microstrip to WR-10 transition using ridge and groove gap waveguide based transformer, however in this design the shaping of the substrate simplifies even more both the design and the fabrication of the transition.

2.1 Theoretical analysis

2.1.1 Theoretical analysis based on Chebyshev transformer

All the transitions presented in this thesis are based on Chebyshev transformers [Orf13]. This is an analytical method based on small reflection theory which equates the reflection coefficient to a Chebyshev polynomial. This way, Chebyshev matching transformers have wider bandwidth than other transformers at the expense of a passband ripple. A schematic of a multisection transformer is shown in Figure 2.1. It must be noticed that Chebyshev transformers are gradual and match a low impedance to a high impedance or viceversa.

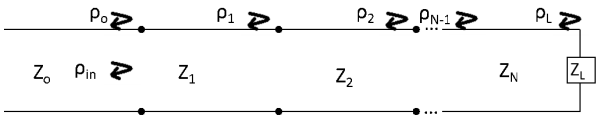

Figure 2.1: Schematic reflection coefficients for a multisection transformer.

Chebyshev Polynomials

The n-th order Chebyshev polynomial is a polynomial of degree n, denoted by $T_N(x)$. The first four polynomials are

$$T_1(x) = x, \tag{2.1}$$

$$T_2(x) = 2x^2 - 1, \tag{2.2}$$

$$T_3(x) = 4x^3 - 3x, \tag{2.3}$$

$$T_4(x) = 8x^4 - 8x^2 + 1. \tag{2.4}$$

Higher order polynomials are calculated using the recurrence formula:

$$T_n(x) = 2xT_{n-1}(x) - T_{n-2}(x). \tag{2.5}$$

General design method of Chebyshev transformer

The overall maximum value of the reflection coefficient magnitude for the Chebyshev sections, i.e the entire transition, can be calculated as [Orf13]:

$$A = \ln\left(\frac{Z_L}{Z_0}\right)\frac{1}{2T_N(\sec(\theta_M))} \tag{2.6}$$

where N is the order of the Chebyshev transformer, T_N is the Chebyshev polynomial of Nth order, Z_L is the load impedance, and Z_0 is the input impedance.

The parameter θ_M is given by

$$\theta_M = \frac{\pi}{2}\left(1 - \frac{\Delta f}{2f}\right) \tag{2.7}$$

where Δ_f is the bandwidth of the transition, and f is the central frequency.

The reflection coefficients are calculated using:

$$\begin{aligned}\rho(\theta) = 2e^{(-jN\theta)}[\rho_0 \cos N\theta + \rho_1 \cos(N-2)\theta + \ldots + \\ \rho_n \cos(N-2n)\theta + \ldots] = |A|e^{(-jN\theta)}T_N(\sec\theta_m \cos\theta)\end{aligned} \tag{2.8}$$

where $\theta = \beta l$ and ρ_n is the reflection coefficient between the transformer sections. Equating same order terms in $\cos n\theta$, the reflection coefficients are obtained.

Finally, the impedance of the n-th section, Z_n, satisfies:

$$Z_n = Z_{n-1}e^{2\rho_{n-1}} \tag{2.9}$$

2.1.2 Theoretical analysis for pin dimension

In this section we present some inline transitions based on gap waveguide technology. This type of waveguide consists of an air channel in between two periodic metallic pin sections creating a propagation band. Here we present an analytical approach to the calculation of the dimensions of the metallic pin based on the theoretical study developed in [Raz13]. The square metallic pin structure and dimensions notation are shown in Figure 2.2.

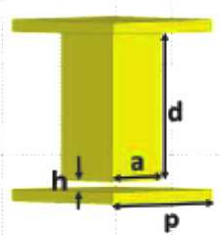

Figure 2.2: 3D geometry of the metallic pin.

We can estimate the period, p, as follows:

$$p \leq \lambda/2 \tag{2.10}$$

where λ is the wavelength at central frequency. Usually a good result is obtained when the relation between the pin width and period is $a/p = 0.5$. The height of the pins, d, can be computed with the next equation :

$$d = \lambda_{c1}/4 \tag{2.11}$$

where λ_{c1} is the longest wavelength, i.e. the lower cut-off frequency of the desired bandgap.

The air gap is calculated as:

$$h = \lambda_{c2}/2 - d \tag{2.12}$$

where λ_{c2} is the shortest wavelength, i.e the upper cut-off frequency of the desired bandgap. Below the lower cut-off frequency as well as above the upper cut-off frequency there is propagation through the bed of nails. This propagation is avoided within the designed band gap. Therefore an air channel surrounded by periodic metallic pins can be used as a transmission line in this frequency range.

2.2 Microstrip to Standard WR-10 Waveguide Transition

This first prototype is an alternative design to the E-probe microstrip to waveguide transition, since it is based on an inline configuration. Moreover, it is also an alternative to other inline transitions [Zha10, Reb15, Alj17], for it does not use any soldering or a gradual taper of the dielectric material, which can be difficult to manufacture for W-Band frequencies and above. It is, therefore, simpler than other inline transitions and easier to manufacture, which makes it appropriate for sub-millimeter and Terahertz frequencies. In addition, the proposed configuration allows a simplified design based on standard Chebyshev impedance transformers (see Section 2.1). Furthermore, for the microstrip section, two alternatives will be compared: a microstrip Chebyshev transformer and a linear taper transition [Pé16]. In both cases, calculation of dimensions of the whole transition is made analytically, which avoids full-wave optimization.

2.2.1 Configuration and Transition Concept

Two prototypes have been evaluated and their perspective view are shown in Figure 2.3.

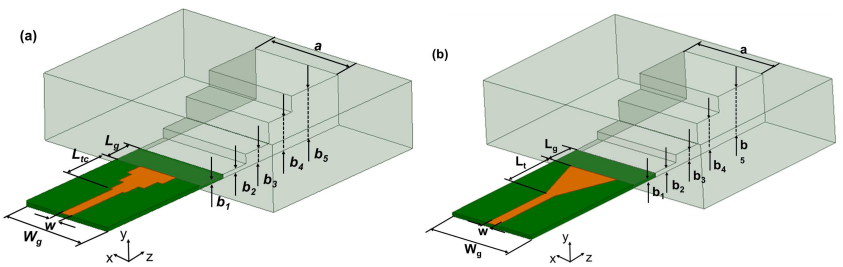

Figure 2.3: 3D geometry of the microstrip to standard rectangular waveguide (WR-10) transition: (**a**) microstrip Chebyshev transformer and (**b**) microstrip linear taper. The grey areas correspond to the rectangular waveguide metallic walls.

The proposed transitions first couple the quasi-TEM mode of the microstrip line to the TE_{10} mode of a dielectric filled rectangular waveguide (DFRW). Afterwards, the transition from DFRW to standard rectangular waveguide is

done by means of a multisection Chebyshev transformer. As a difference to previous designs, in this case, homogeneous waveguide sections will be used. This allows the design method to be completely analytic and make use of the Chebyshev transformer design procedure presented above (Section 2.1). For the microstrip to DFRW section, two alternatives are proposed: a Chebyshev transformer (Figure 2.3(a)) and a linear taper transition (Figure 2.3(b)).

In this case, the DFRW impedance is an intermediate impedance lower than both the input microstrip line and the standard waveguide impedance. For instance, for the standard WR10 waveguide $a = 2.54$ mm and $b = 1.27$ mm, leading to $Z_L = 376.7\ \Omega$, whereas for the dielectric filled rectangular waveguide b corresponds to the substrate thickness. If a 0.1-mm-thick Rogers CuClad ($\epsilon_r = 2.4$) is considered, $Z_{DFRW} = 19\ \Omega$. Since this intermediate impedance is lower than the start and final impedances, it is not possible to design directly a Chebyshev transition. Therefore, the procedure for the calculation of the inline microstrip-to-rectangular-transition must be a two-step process. The first one is the design of the transition from DFRW to rectangular waveguide, presented in Figure 2.4. The second one involves the transition from microstrip to DFRW, shown in Figures 2.5. The details of the design of both sections are given in the following subsections.

Transition from Dielectric Filled Rectangular Waveguide to Standard Waveguide

A multisection waveguide Chebyshev transformer is used to match the DFRW with the rectangular waveguide, see Figure 2.4.

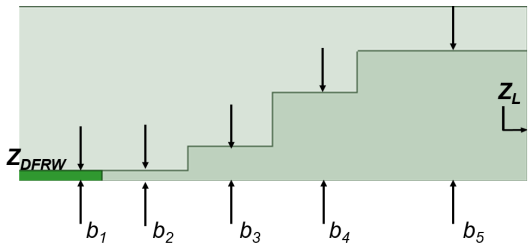

Figure 2.4: Side view of the multisection Chebyshev transformer from dielectric filled rectangular waveguide to standard rectangular waveguide.

The impedances of the rectangular waveguide sections are computed by the

equivalent electric waveguide impedance [Esh05]:

$$Z_{wg} = 2\frac{\eta}{\sqrt{\epsilon_r}}\frac{b}{a} \tag{2.13}$$

where $\eta = \sqrt{\frac{\mu_0}{\epsilon_0}}$ is the free-space wave-impedance, ϵ_r is the relative permittivity of the waveguide filling medium, a is the waveguide width, and b is the height of the waveguide sections.

Once the DFRW and the standard rectangular waveguide impedances have been obtained, Z_{DFRW} and Z_L, we apply the Chebyshev transformer method to calculate the impedances of the matching sections. With these impedance values, the height of each rectangular waveguide section is determined by

$$b_n = \frac{Z_{wg_n}\sqrt{\epsilon_r}a}{2\eta} \tag{2.14}$$

where Z_{wg_n} is the impedance of each waveguide section computed previously with the Chebyshev method.

Note that the first section corresponds to a dielectric filled waveguide, whereas the rest of them are air-filled waveguide sections. A more accurate transition could be designed taking into account the reactance effect due to the change of the waveguide height [Esh05]. This effect should make the transformer sections shorter. However, if the change of height is small, the effect may be negligible. In this design it has not been taken into account for simplicity since the difference is smaller than the tolerances of the manufacturing method. The three sections of the transition have a length l_g equal to $\lambda_g/4$ (at the central frequency).

Transition from Microstrip to Dielectric Filled Rectangular Waveguide

The microstrip to DFRW transition can be carried out with two different approaches. The first one uses also a multisection Chebyshev impedance transformer. The second approach consists of a linear taper that matches the impedance of the microstrip line with the impedance of the DFRW.

- **Multisection Microstrip Chebyshev Impedance Transformer**

  The multisection Chebyhsev transformer is shown in Figure 2.5(a). The microstrip line is built on a substrate with thickness (b_1) which corresponds to the height of the DFRW. Taking this into account, Equation

(2.13) is used to calculate the impedance of the DFRW, and Chebyshev transformer standard equations [Orf13] are employed to determine the impedances of the transformer between 50 Ω and this impedance. The width of the microstrip line sections are given by the well known formulae of the microstrip impedance [Poz04]. The length of each section is $\lambda_{eff}/4$ where λ_{eff} is the wavelength at the central frequency in each microstrip line section.

- **Tapered Microstrip**

  An alternative way of matching the 50 Ω impedance with the impedance of the DFRW can be seen in Figure 2.5(b). This transition consists of a linear microstrip taper of length $L_t = 3\lambda_{eff}/4$ (where λ_{eff} is the guided wavelength of the microstrip line), which is enough to ensure good matching [Des10]. The width W_t is calculated so that the characteristic impedance of the equivalent microstrip line is equal to the impedance of the DFRW.

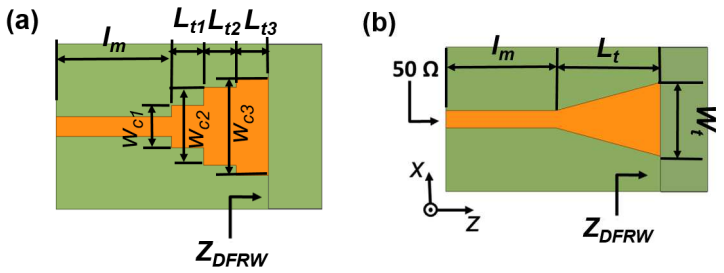

Figure 2.5: Top view of the microstrip to dielectric filled rectangular waveguide transition: (**a**) Chebyshev multisection transformer and (**b**) microstrip linear taper.

2.2.2 Design and Simulation Results

The procedure above described has been applied to the design of a microstrip to a W-band rectangular waveguide inline transition. The microstrip line is printed on a 0.10-mm-thick Rogers CuClad ($\epsilon_r = 2.4$ and $\tan\delta = 0.009$). Losses in the copper line are also included in the simulations. The height of the dielectric filled rectangular waveguide (DFRW), b_1, is the thickness of the substrate, i.e.,

0.1 mm, and the width, a, is the width of the standard WR-10 waveguide, i.e., 2.54 mm.

The dimensions of the DFRW to WR-10 Chebyshev transformer were calculated with the previous procedure. To cover the full W-band $\Delta f = 35$ GHz (which leads to $\theta_M = 1.27$) is required. The maximum reflection coefficient is set to -15 dB, i.e., $A = 0.032$. Three sections are required to comply with this requirement. Table 2.1 shows the dimensions of the required waveguide sections for the Chebyshev transformer. The labels are defined in Figure 2.4.

Table 2.1: Dimensions of the Chebyshev transformer waveguide sections (μm).

Parameter	Value	Fabricated Value
b_1	100	100
b_2	120	115
b_3	320	347
b_4	850	870
b_5	1270	1270
l_{g1}	835	820
l_{g2}	835	817
l_{g3}	835	860

For the microstrip to DFRW section, both versions, i.e., the Chebyshev transition and linear taper, were designed. For the linear taper (Figure 2.5(b)) the dimensions are gathered in Table 2.2.

Table 2.2: Dimension of the microstrip to DFRW linear taper transition (μm).

Parameter	Description	Value
L_t	Length of the taper	1500
W_t	Width of the taper	1300
l_m	Length of the microstrip	2590

The Chebyshev transformer-based transition (see Figure 2.5(a)) consists of three sections, whose impedances were calculated with the same procedure above. Their dimensions are compiled in Table 2.3.

The performance of the microstrip to DFRW transitions (both taper and Chebyshev line) and of the DFRW to rectangular waveguide Chebyshev transformer have been evaluated separately with High Frequency Structure Simulator (HFSS) from Ansys. The simulation results are shown in Figure 2.6.

Table 2.3: Dimension of the microstrip to DFRW Chebyshev transition (μm).

Parameter	Description	Value
a	Width of the rectangular waveguide	2540
W	Width of the microstrip	301
W_{c1}	Width of section 1	450
W_{c2}	Width of section 2	780
W_{c3}	Width of section 3	1100
L_{t1}	Length of section 1	493
L_{t2}	Length of section 2	485
L_{t3}	Length of section 3	481
L_g	Length of the DFRW	830
l_m	Length of the microstrip	2590

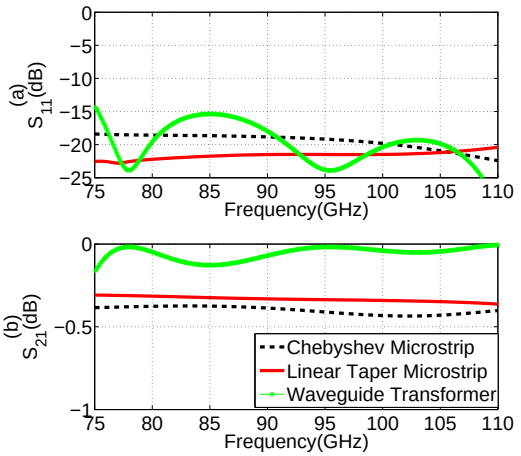

Figure 2.6: Performance evaluation of the different parts of the transition: (Solid red line) Linear microstrip to DFRW transition, (Dashed black line) Chebyshev microstrip to DFRW transition and (Star green line) DFRW to rectangular waveguide Chebyshev transformer. (**a**) Reflection (S_{11}); (**b**) Transmission (S_{21}).

Return loss results are shown in Figure 2.6(a), where we can appreciate that the linear taper microstrip line performs better than the Chebyshev transformer microstrip transition, both in return loss and insertion loss. For the DFRW to

waveguide transition, the maximum return loss is in good agreement with the objective performance, a return loss higher than 15 dB. This result justifies that the previously mentioned additional reactance created in the waveguide steps does not affect the transition performance. In Figure 2.6(b), the S_{21} parameter is presented. For all cases, the insertion losses are below 0.5 dB.

The predicted responses of the whole transitions are presented in Figure 2.7, where a comparison of the return loss between the linear taper and Chebyshev transitions is presented.

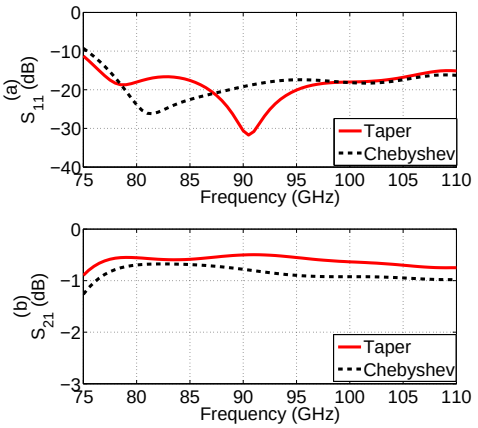

Figure 2.7: The simulation results of the two proposed whole transitions: (Dashed line) Chebyshev impedance transformer and (Solid line) microstrip taper. (**a**) Reflection (S_{11}); and (**b**) Transmission (S_{21}).

It can be observed that the reflection (S_{11}) is below -15 dB in both cases. On the other hand, Figure 2.7b shows the insertion loss. For both cases, the insertion losses are lower than 1 dB in the full W-band. Nevertheless, the Chebyshev case has larger insertion losses than those of the tapered transition. These losses are ascribed to the radiation in the steps between the different impedance sections of the Chebyshev transformer. Note that the transitions include a 2.59 mm microstrip line. The contribution of this line to the insertion losses above has been estimated as 0.33 dB. If these losses are removed, the insertion loss of each transition can be estimated to be better than 0.5 dB and 0.8 dB for the linear and Chebyshev cases, respectively.

Finally, it is worth pointing out that all these results have been accomplished

with the dimensions resulting from the analytic procedure above. There has not been any optimization, and the objective return loss and bandwidth are fulfilled.

2.2.3 Manufacturing

Since the experimental validation will be carried out with a waveguide-based vector network analyser, a back-to-back transition is needed. A photograph of the fabricated back-to-back waveguide blocks and microstrip taper in Rogers CuClad is shown in Figure 2.8.

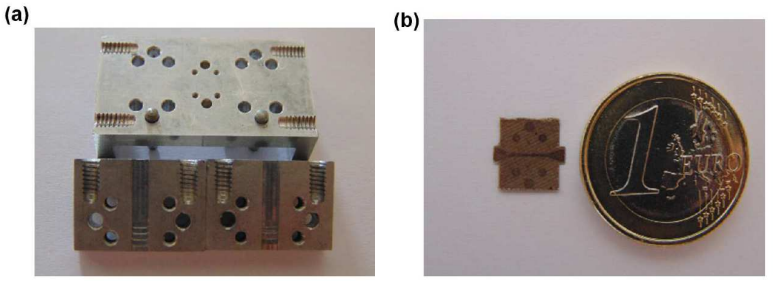

Figure 2.8: Photograph of (**a**) a fabricated back-to-back waveguide block; (**b**) a fabricated microstrip taper in Rogers CuClad.

The manufactured process has to be separated in two parts: the milling process for the waveguide sections and the photolithographic process for the microstrip. Figure 2.8(a) shows the micromachined back-to-back waveguide blocks for the transition. They are made of aluminium by a high precision milling machine. To simplify assembly the waveguide block has been split in the H-plane, and both parts are screwed together. To reduce losses in the H-plane cut, this contact must be very tight, which is guaranteed by eight screws and four dowel pins. The block has been designed and manufactured with the appropriate WR-10 flange. The whole waveguide block is 34.2 mm long and 19.05 mm wide. The fabricated dimensions, shown in Table 2.1, are slightly different from the original design. The largest deviation correspond to the height of Chebyshev step (b_3), where the error is 8 %. Note also that 0.150 mm radius rounded corners were created by the manufacturing method. The microstrip section was manufactured at the Public University of Navarra facilities following a standard photolithography procedure, see Appendix A for details. The lines were created by sputtering the CuClad substrate with 2

μm of copper. Finally,the substrate was cut with the required shape with a milling machine. Due to the better performance of the linear taper microstrip transition shown in simulation, only this one was fabricated and measured. The final circuit is shown in Figure 2.8(b).

2.2.4 Experimental Validation

The set-up for measurements is shown in Figure 2.9. An Agilent PNA-X E3861 Microwave Network Analyzer with two VDI W-Band VNA Extenders was used. The equipment has been calibrated using the standard W-Band TRL (Through-Reflect-Line) calibration kit for VDI extenders. The manufactured back-to-back transition was connected in between the extender waveguide ports, and S parameter measurements were carried out.

Figure 2.9: Setup for the experimental validation of the microstrip-to-waveguide transition.

The measured reflection coefficient, presented in Figure 2.10, shows a degradation of the performance with respect to the design, Figure 2.7. First, the working band has been shifted towards higher frequencies. For this reason, the return loss between 75 and 80 GHz becomes lower than 10 dB. In addition, the return loss increases to nearly 12 dB in the central frequency. However, taking into account the whole band, they are higher than 8 dB. The insertion losses also increase, and the measured values are between 0.4 and 0.7 dB higher than the predictions. The obtained average value is 1.9 dB.

This degradation is ascribed to the manufacturing errors. These errors can be noticed in Table 2.1. They are particularly large in Chebyshev step 3, with

more than 20 μm difference in both length and height. The real dimensions have been simulated in order to perform a fair comparison with the measurements. This comparison is shown in Figure 2.10. There is good agreement between them, especially from 75 GHz to the central frequency, 92.5 GHz. The higher return loss was adequately predicted. The transmission coefficient is displayed in Figure 2.10(b).

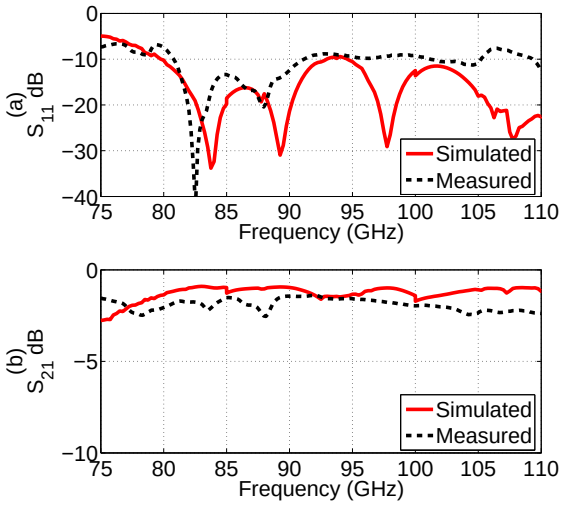

Figure 2.10: Simulated performance taking into account the fabricated dimensions (solid line) and measured (dashed line) back-to-back transition. (**a**) Reflection (S_{11}) and (**b**) Transmission (S_{21}).

The mean value of the simulated and measured insertion losses is 1.5 dB and 1.9 dB, respectively. These losses include those in the transitions and in the 5.18 mm microstrip line. Taking into account the value of $\tan\delta = 0.009$ and the conductivity of copper, this microstrip line has a 0.65 dB insertion loss. If these losses are removed, the average insertion loss of each transition can be assumed to be 0.63 dB. A comparison with other similar transition is realized in Table 2.9.

2.3 Microstrip to Groove Gap Waveguide Transition

In this section we will focus on the so-called groove gap waveguide (GGW). This waveguide consists of an air channel in between two periodic metallic pins sections, also known as bed of nails, that allow the propagation of an electromagnetic mode similar to the rectangular waveguide TE_{10}. The bed of nails is a structured surface that creates an Artificial Magnetic Conductor (AMC), which prevents propagation of electromagnetic waves in a certain frequency region. An inline microstrip to groove gap waveguide transition working at W-Band will be presented here. The transition design follows the same analytical approach, see Section 2.1, and the design procedure is similar to that presented in Section 2.2, but adjusted to groove gap waveguide technology instead of standard waveguide technology. As a consequence, since the dimensions are computed by means of the standard Chebyshev transformer design formulae, full wave optimization is avoided. In addition, as an improvement to the previous design, the GGW provides a good solution for the contact problem due to the H-plane split.

2.3.1 Proposed Transition and Simulation Results

The proposed inline transition is presented in Figure 2.11. The operating principle is based on the high similitude between the field distribution of the quasi-TEM mode of the microstrip line and the so called vertical mode of the groove gap waveguide (GGW)[Ber16], which guarantees good coupling between them. Even though this principle and the design procedure presented for this kind of transition is applicable to any frequency band, in this case the transition will be realized to work at W-Band. The transition consists of two sections: a Chebyshev transformer from standard (air filled) GGW to dielectric filled GGW and a linear transition from microstrip to dielectric filled GGW.

Groove Gap Waveguide design

For groove gap waveguide design, firstly, the pin that forms the periodic metallic pin distribution that sourrounds the waveguide, also refered to as bed of nails, is designed to have its band-gap in the desired frequency range [Reb14, Raj11]. In this case, the pin parameters were optimized using eigenmode solver so that the band-gap covers the W-band, i.e. 75-110 GHz, and the final dimensions are gathered in Table 2.4.

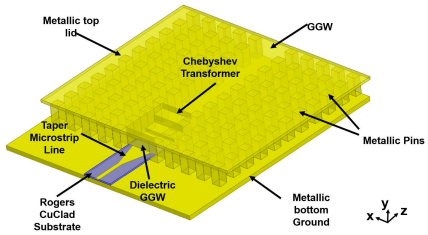

(a)

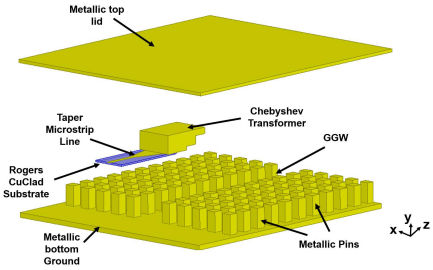

(b)

Figure 2.11: (a) Perspective view the proposed microstrip to groove gap waveguide (GGW) transition. (b) Explosion view of the microstrip to GGW transition.

Table 2.4: Dimensions of the unit cell (metallic pin) of the bed of nails (μm).

Parameter	Description	Value (μm)
d	Pin height	1190
a	Pin size	600
h	Air gap	80
p	Period	1240

The resulting dispersion diagram, computed with HFSS eigenmode solver, is shown in Figure 2.12. We can observe that the band-gap, determined by the highest frequency of the first mode of the dispersion diagram and the lowest frequency of the second mode of the dispersion diagram, covers the full W-band.

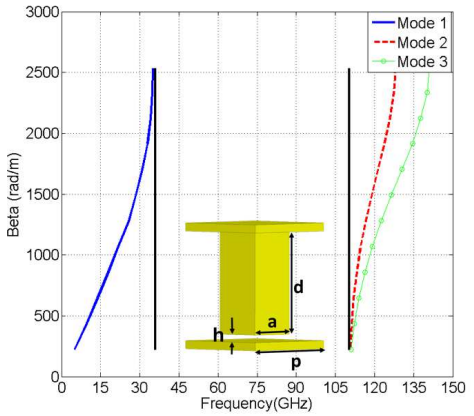

Figure 2.12: Dispersion diagram of the periodic unit cell.

Based on these pins, a GGW was created by leaving a gap in between them. In order to make the resulting GGW compatible with a W-band WR10 rectangular waveguide, the height of the GGW is the same as that of the WR10 waveguide, i.e. d+h = 1.27 mm. Regarding the width, w in Figure 2.13, it should be adjusted for monomode operation in the desired frequency range. In our case, in order to facilitate testing, it should also provide good matching to a WR10 waveguide.

The best result was obtained for $w = 2.45\ mm$ and the performance of this direct connection is shown in Figure 2.13. The return loss is higher than 25 dB within the W-band operational bandwidth (75-110 GHz) and the insertion loss is negligible, below 0.1 dB. The different width between GGW and standard waveguide may be caused by the different boundary condition at the waveguide walls, which allow evanescent fields to penetrate the lateral pin regions. Note that five periods of pins surround the waveguide (Fig. 2.11). Even though a smaller number of pins (usually three rows) would be enough to prevent leakage (Fig. 2.13), the whole available surface was covered with pins.

Transition design

As mentioned, the transition is divided into two parts: a Chebyshev transformer between air filled and dielectric filled GGW and a microstrip linear taper (see

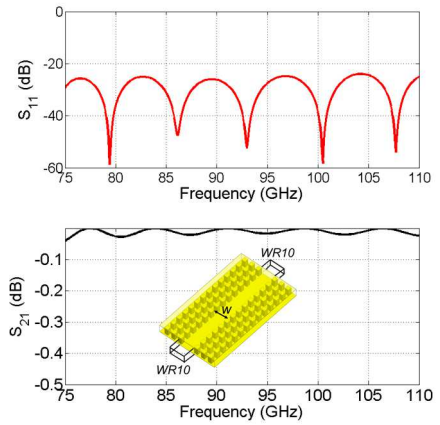

Figure 2.13: Performance of a direct connection between a gap groove waveguide and a WR-10 rectangular waveguide: (a) Return loss. (b) Insertion loss.

Figure 2.14 for details). The first part follows a similar approach to that proposed in previous section. The impedances of the Chebyshev transformer sections are calculated by the standard formulation presented in section 2.1. For this design a three section transformer is enough to obtain return loss higher than 15 dB in the full W-band.

These impedances calculated with Chebyshev transformer method can be equated with the corresponding electric impedance of a waveguide [Esh05] using equation 2.13, taking into account that the width corresponds to the equivalent width of the GGW, 2.45 mm. Afterwards, the heights are calculated using equation 2.14.

Figure 2.14(a) shows a perspective view of the three steps of the half-split Chebyshev transformer with waveguide height b_n and length l_n, which corresponds to $\lambda_g/4$. The input GGW section is filled with dielectric, and its height corresponds to the substrate thickness plus the metal cladding. Note that there is no restriction on its length, since this section is not strictly a part of the Chebyshev transformer. The same value as for the other sections has been taken. In addition, given the change of dielectric, the required impedance of the first section is obtained with the same height, i.e. $b_1 = b_0$.

The second part corresponds to a microstrip linear taper, whose top view is shown in Figure 2.14(b). This line, which matches the 50 Ω to the input

waveguide impedance is calculated using the standard microstrip impedance formula and a $3\lambda_g/4$ length [Poz04]. It is printed on 100 μm thick Rogers CuClad 233 ($\epsilon_r = 2.34$ and $\tan\delta = 0.009$) and the calculated width to obtain the impedance of 50 Ω is 300 μm.

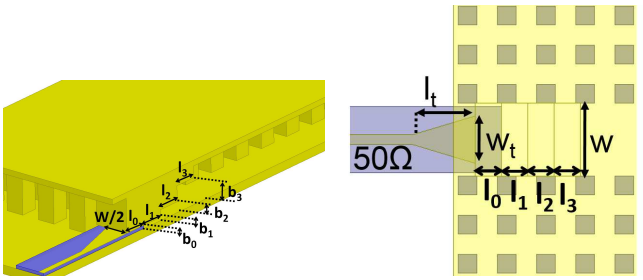

Figure 2.14: Microstrip to groove gap waveguide transition: (a) Perspective view of the half-split Chebyshev waveguide transformer and (b) Top View. It is important to notice that the microstrip taper touches the metal of the DFGW.

The dimensions of the whole transition can be seen in Table 2.5.

Table 2.5: Dimensions of the transition (μm).

Parameter	Description	Design	Fabricated
l_t	Microstrip taper length	1500	1467
w_t	Microstrip taper width	1300	1256
b_1	GGW Height 1	116	158
b_2	GGW Height 1	116	158
b_3	GGW Height 3	380	407
b_4	GGW Height 3	950	953
l_1	Metal Step length 1	830	859
l_2	Metal step length 2	830	821
l_3	Metal step length 3	830	810
l_4	Metal step length 3	830	810
w	GGW width	2450	2290
b	WR-10 waveguide height	1270	1280

The structure has been simulated using the commercial Finite Element Method solver of HFSS. First, the two different parts, i.e. the microstrip to dielectric filled GGW and the Chebyshev transformer between dielectric filled GGW and air filled GGW, have been simulated separately. These results are presented in Figure 2.15.

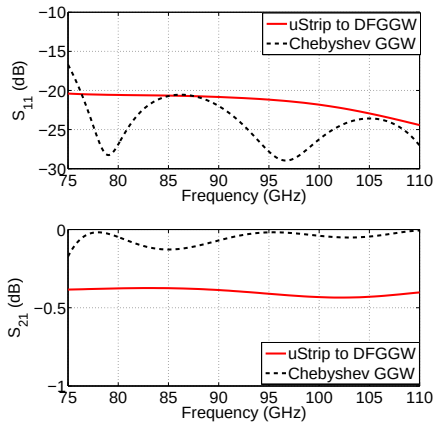

Figure 2.15: Simulation of the scattering parameters of the microstrip to dielectric filled GGW (solid red line) and the GGW Chebyshev transformer (dashed black line).

It can be seen that the return loss is better than 20 dB for both cases. On the other hand, the insertion loss are lower than 0.5 dB for both cases. Nonetheless, in the microstrip case the losses are higher, due to the dielectric and radiation losses. Note that these results have been obtained with the analytic procedure above, without any full-wave optimization.

The back-to-back transition includes a 5.18 mm microstrip line in between the two transitions; the model used for simulation is shown in inset of Figure 2.16. When the whole transition is analysed, the insertion and return loss results shown in Figure 2.16 are obtained.

The mean insertion loss is 0.66 dB for the single transition and 1 dB for the back-to-back configuration. The higher insertion loss in the back-to-back configuration is ascribed to the substrate losses in the longer microstrip line. The losses in the microstrip line have been calculated by full wave simulation in HFSS taking into account the loss tangent of the dielectric material at high

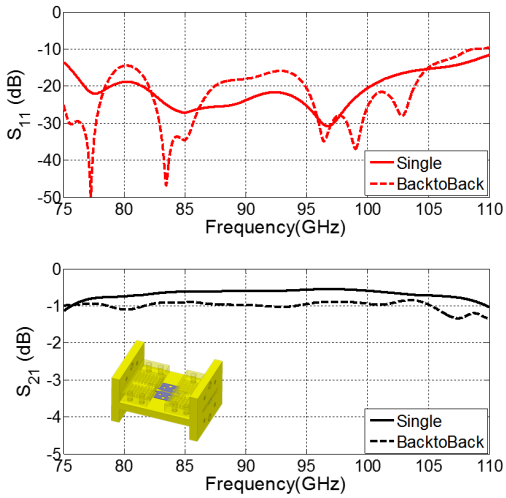

Figure 2.16: (Inset) 3D perspective view of the back-to-back microstrip to standard waveguide transition model for simulation in HFSS. (b) Simulation of the scattering parameters for the microstrip to groove gap waveguide single (solid line) and back-to-back transitions (dashed line).

frequencies ($tan\delta = 0.009$). For the single transition these losses are 0.33 dB. Therefore, the losses of the transition can be estimated as $0.66 - 0.33 = 0.33$ dB. The mean return loss is 24.1 dB and 17.2 dB for the single and back-to-back transitions, respectively. The back-to-back transition presents worse S_{11} due to the non perfect matching at both ports. Anyway, return loss is better than 15 dB for almost the whole band in both configurations. In Figure 2.17 the electric field distribution at 92.5 GHz is shown.

It can be observed that the Quasi-TEM mode of the microstrip line couples to the vertical mode of the GGW. Furthermore, the mode confinement in the GGW region thanks to the bed of nails can be also appreciated, although the field evanescently decays in the pin areas.

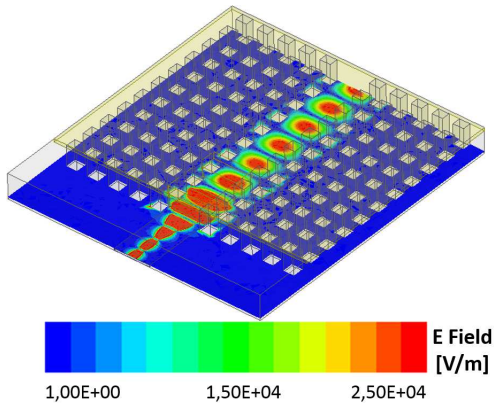

Figure 2.17: E-Field distribution of the microstrip to GGW transition at f = 92.5 GHz.

2.3.2 Tolerance analysis

The effect of different manufacturing and assembly errors will be evaluated in this section. The results are summarized in Figure 2.18.

First, the effect of the air gap between the bed of nails and the lid on the performance of the transition will be studied. As a matter of fact, one of the main problems when rectangular waveguides are split in the H-Plane is the tight contact required between both parts in order to reduce losses. This problem is alleviated by the use of the bed of nails, since no contact is required. In our design an 80 μm air gap has been considered at the end of the pins. To evaluate the error tolerance on this air gap the pin length has been swept around the nominal value. The results are shown in Figure 2.18(a).

We can observe that when the air gap is smaller than the nominal value, the transition behaviour remains hardly unaffected. The performance gets worse at the central frequency but in any case the reflection coefficient is below -18 dB. However, when the air gap increases, there is a certain degradation of the performance and the bandwidth below -15 dB is reduced. Consequently, there is also an increase of the insertion losses, in particular at the beginning of the band. Nonetheless, the performance is still acceptable and represents a good solution for H-plane splits.

In addition, different errors related to misalignments of the microstrip substrate have been considered. First, the misalignment in the waveguide longitu-

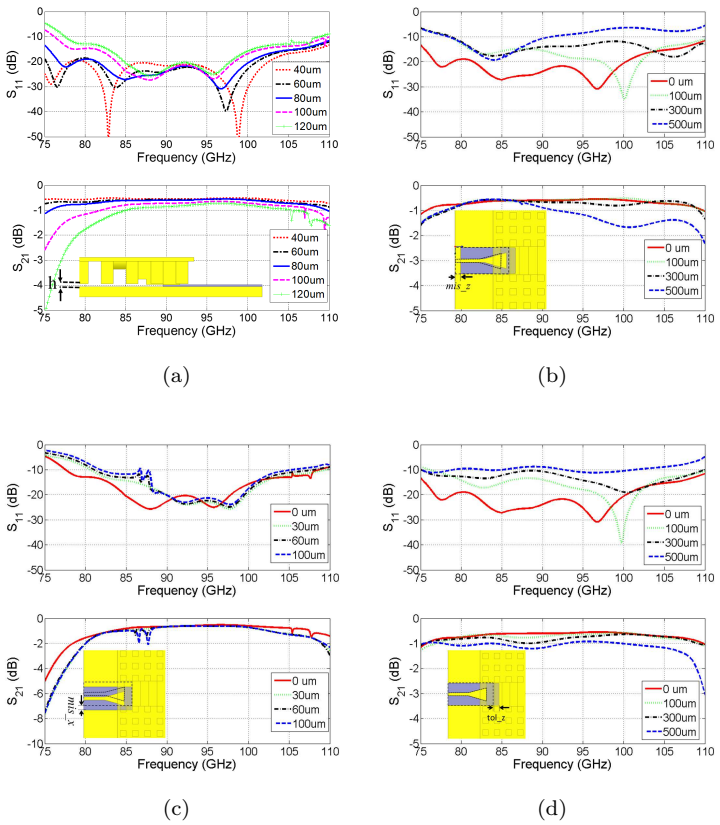

Figure 2.18: (a) Evaluation of the effect on the transition performance of errors in the fabrication of the metallic pins, given by different values of h. (b) Evaluation of the effect on the misalignment in the z direction, given by different values of mis_z. (c) Evaluation of the effect on the misalignment in the x direction, given by different values of mis_x. (d) Evaluation of the effect on the error in the substrate cutting so that this is longer than nominal, given by different values of tol_z. The dashed line represents the position of the circuit without misalignment error.

dinal direction, i.e. z direction according to Figure 2.11 has been analysed. In this case the misalignment produces the microstrip taper length to be shorter than designed and the substrate enters into the second step of the Chebyshev transformer, see the inset in Figure 2.18(b) for clarification. The simulation results for different values of misalignment are shown in Figure 2.18(b). The response is still acceptable for 100 μm, with $S_{11} \leq -12\ dB$ for almost the whole band. However, for 500 μm the performance is not satisfactory. The return loss condition for working at W-Band, $S_{11} \leq 15$ dB, is only fulfilled from 82 GHz to 87 GHz, which does not guarantee a good performance.

Another effect that has been taken into account is the misalignment in the transverse direction, i.e. in the x direction according to Figure 2.11. This positioning error implies that the pins touch the dielectric substrate and therefore the air gap at their end becomes equal to the substrate thickness, i.e. 0.127 mm. Therefore, the nominal case corresponds to the substrate centred with the GGW, but with this value of h, different from the optimum, 80 μm. In this case, the effect is more important than in the previous one, see Figure 2.18(c), mainly because, due to the loss of symmetry, the displacement prevents the microstrip taper from exciting the GGW mode properly.

As a matter of fact, a high order resonance is excited for misalignments larger than 30 μm. Nonetheless, the performance is still acceptable until the displacement is 100 μm. Thus, the alignment pins in the microstrip substrate are necessary in order to guarantee accurate assembly. Finally, the effect that the substrate has a cutting error so that it is longer than the designed one has been evaluated. The effect is shown in Figure 2.18(d). This error is not so critical, since it just affects the impedance and propagation constant of the second transformer section. The S_{11} is below -10 dB for all cases; thus, the circuit is tolerant to this misalignment.

2.3.3 Manufacturing and Experimental validation

In order to verify the transition performance, the back-to-back configuration was manufactured and tested. As explained previously, the two transitions were separated by a 5.18 mm long microsrip line. The behaviour of the whole structure is not affected by this microstip length; however, the longer the microstrip the higher the circuit global losses. The GGWs were 9 mm long and were connected directly to the WR10 rectangular waveguides of the W-band millimetre wave extenders.

The metallic block was micromachined in aluminium and split in the H-Plane. The pins are machined just in one of the metallic blocks, the other

one being flat. Proper alignment was guaranteed by eight screws and eight alignment pins. Since a tight contact between the upper and bottom metallic parts is not required, the manufacturing tolerances can be relaxed.

The microstrip transition was manufactured by a standard photolithography procedure at the Public University of Navarra's facilities, following the procedure described in Appendix A. Photographs of the fabricated prototype can be seen in Figure 2.19(a).

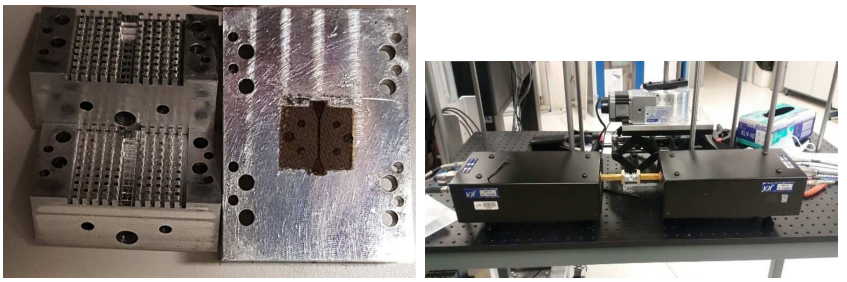

(a) (b)

Figure 2.19: Photograph of the fabricated prototype and measurement set-up. (a) Picture of the microstrip line printed on CuClad substrate on the bottom metallic block and on the left the two upper metallic parts. (b) Setup of the back-to-back transition connected to W-Band VDI extenders.

The circuit assembly is simple. The substrate is placed on the bottom metallic block with the help of the alignment pins. It is then tightly screwed and finally the circuit is closed with the top metallic block. It is not necessary to weld or glue any part.

Once assembled, the back-to-back transition was measured with an Agilent PNA-X E3861 Microwave Network Analyser with two VDI W-Band VNA Extenders. Previously the equipment was calibrated using the standard TRL (Through, Reflect, Line) calibration kit. Figure 2.19(b) shows a photograph of the measurement setup. A comparison between the measurements and the back-to-back simulation, for the ideal case and for the case taking into account the deviation of the dimensions produced by the tolerance error in the fabrication process is plotted in Figure 2.20. These dimensions have been measured with a Mitutoyo Hyper MF-U 176-402-43 measuring microscope.

Comparing with the simulation results shown in Figure 2.16 where the tolerance error of manufacturing are not taken into account, the cut-off frequency

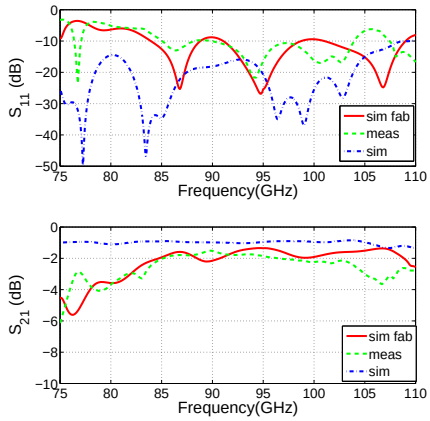

Figure 2.20: Comparison between simulated (point-dashed blue line), simulation taking into account fabrication errors (solid red line) and measured (dashed green line) back to back transition.

and the performance is blueshifted and there is certain degradation in terms of performance. The frequency shift is ascribed to the narrower manufactured GGW channel, which is 2.39 mm wide instead of 2.45 mm. Nonetheless, the predicted response once the fabricated values are introduced in the simulation model is in good agreement with the measured performance. The best measured insertion loss is 1.5 dB at 90.4 GHz, with 3 dB mean value if the full W-band is considered. These losses include those in the transition and in the microstrip line. For the 5.18 mm long microstrip line the losses computed by HFSS are 0.66 dB. If the transition is considered symmetric and the losses of the microstrip line are removed, the transition losses can be estimated as 1.17 dB for each single transition, i.e. the taper and the Chebyshev transformer. Finally, the return loss is better than 10 dB from 83.9 GHz to 109 GHz, except for a resonant peak at 105 GHz.

2.4 Microstrip to Rectangular Waveguide Transition Packaged by Gap Waveguide

In this section a simplified inline transition from microstrip to standard rectangular waveguide packaged by gap waveguide technology is presented. This transition presents two main advantages when compared with the previous designs. On the one hand, it provides a solution to the problems caused by the H-plane split, which are solved by means of the use of gap waveguide technology. On the other hand, the unwieldy task of fabrication and assembly due to the shaped cutting of the dielectrics can be avoided, taking into account that the substrate may partially fill the gap waveguide and the bed of nails. Therefore, the propagation constant and the effect of the dielectric in the cutoff frequency of the partially dielectric filled gap waveguide are also studied in this section.

2.4.1 Transition Concept

The structure proposed in this paper consists of a Chebyshev transformer based on ridge and groove gap waveguide. The whole bottom metallic part is covered by a dielectric substrate where a tapered microstrip line has been printed to connect the ridge gap waveguide to the microstrip line. Finally, the groove gap waveguide is directly connected to a standard rectangular waveguide. The scheme of the whole structure is presented in Figure 2.21.

The whole transition is surrounded by periodic metallic pins, which form the gap waveguide.

2.4.2 Groove gap waveguide characteristics

The core of the transition is the groove gap waveguide. Therefore, the properties of this waveguide will be studied in this section. Firstly, the periodic metallic pins distribution is optimized to have the band gap in the desired frequency range [Raj11], in this work W-Band. The structure of the pin can be seen in Figure 2.22(a) and the optimized dimensions are compiled in Table 2.6.

In this case, in order to facilitate the use of this transition with wide microstrip substrates, the gap between the pins and the lid is filled with a dielectric substrate, in this case a 100 μm thick slab of Rogers CuClad ($\epsilon_r = 2.34$ and $\tan\delta = 0.009$). The optimized dimensions are compiled in Table 2.6.

The performance of this waveguide has been found to be similar to that of a equivalent rectangular waveguide, whose width has been demonstrated to be

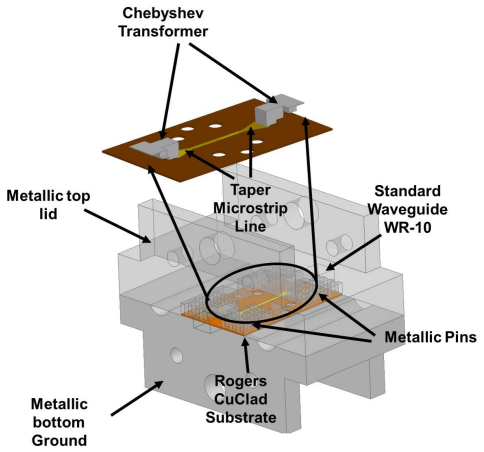

Figure 2.21: 3-D view of the proposed back-to-back microstrip to rectangular waveguide transition model for HFSS simulation.

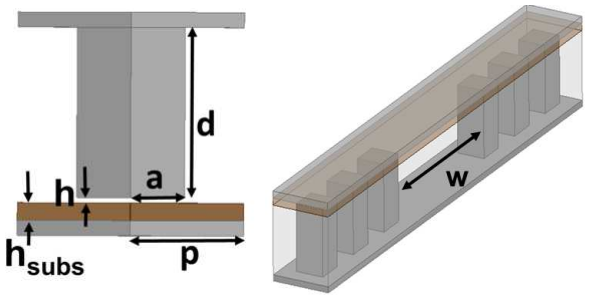

(a) (b)

Figure 2.22: Perspective view of the structure solved using HFSS eigenmode: (a) Metallic Pin and (b) Groove Gap Waveguide with Rogers CuClad substrate.

narrower than the width of the GGW channel [Ber16, Raj10]. Although the propagation characteristics of groove gap waveguides have been studied, in this work we are dealing with partially filled GGW. Therefore, an analysis of the propagation characteristics of this dielectric filled GGW has been done. The height of the GGW is the same as that of the equivalent rectangular waveg-

Table 2.6: Dimension of metallic pin (μm).

Parameter	Description	Value
a	pin size	500
d	pin height	1120
h	air gap	34
p	period	1050
hsubs	substrate height	116

uide. The width w (see Figure 2.22(b) for clarification) is parametrized and its propagation constant, β, is compared with that of a standard waveguide in Figure 2.23.

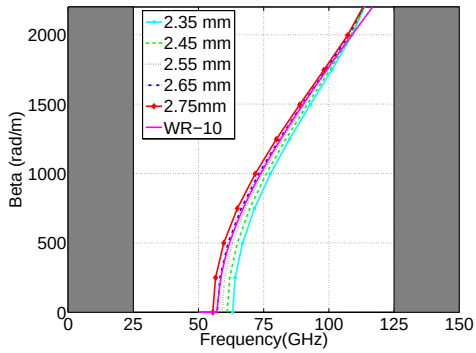

Figure 2.23: Comparison of the propagation constant, β , between groove gap waveguide with different width w and the standard rectangular waveguide.

It can be observed that the propagation constant for all widths is similar at high frequencies. However, the behaviour at low frequencies turns out to be quite different between them. The cutoff frequency of the GGW is higher than the cutoff frequency of the standard rectangular waveguide for the same propagation channel. This effect is produced because the GGW is electrically smaller than the rectangular waveguide but it shows a higher dispersion [Ber16]. In this case, the most similar behavior in terms of propagation constant corresponds to 2.65 mm GGW width (w).

2.4.3 Transition design

The next step corresponds to the design of the Chebyshev transformer that matches the standard rectangular waveguide to the first dielectric ridge waveguide. Following a similar procedure to that presented in [Pé18] (Section 2.3), the impedances of the transformer are calculated by the standard formulation [Orf13](Section 2.1). The order of the transition is calculated to reach 20 dB return loss. The impedance of the groove gap waveguide sections is adjusted by changing their height according to the waveguide electric impedance formula [Esh05].

The GGW is partially filled with the dielectric substrate. Therefore, the effective ϵ_e changes with different GGW heights. Moreover, if ϵ_e changes, the cutoff frequency (f_c) of the second mode also does: the smaller the height, the lower the cut-off frequency. Therefore, an analysis of f_c versus waveguide height was carried out and shown in Figure 2.24 for constant width $w = 2.65\ mm$. It can be observed that for waveguide height lower than 0.6 mm the second mode propagates within the W-Band; therefore, those waveguides whose height, b_n, provides this second order mode propagation are substituted by ridge gap waveguide sections in order to achieve the required impedance without the presence of higher order modes [Poz04].

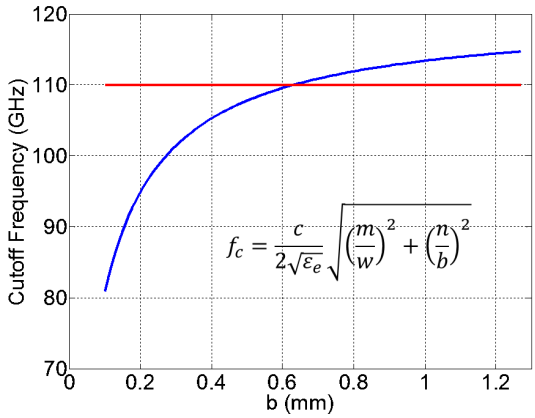

Figure 2.24: Evaluation of the cutoff frequency for different waveguide height (b). (Inset) Formula of cutoff frequency where c is velocity of light, m and n are index of the TE_{mn} mode.

Table 2.7: Dimensions of Chebyshev transformer waveguide sections and microstrip line (μm).

Parameter	Description	Ideal Value	Fabricated Value
w	GGW Width	2650	2590
w_r	RGW Width	1200	1130
t_1	Metal step thickness 1	1139	1164
t_2	Metal step thickness 2	882	843
t_3	Metal step thickness 3	402	361
t_4	Metal step thickness 4	54	28
l_1	Metal Step Length 1	925	941
l_2	Metal Step Length 2	673	685
l_3	Metal Step Length 3	705	683
l_4	Metal Step Length 4	726	697
l_t	Taper Length	1500	1467
w_t	Taper Width	1300	1256

Finally, the second part of the transition is a microstrip taper that matches the 50 Ω microstrip line to the impedance of the dielectric filled ridge gap waveguide (DFRGW), see Figure 2.25(b) [Poz04].

2.4.4 Simulated performance of the proposed prototypes

The procedure above explained has been applied to a microstrip to standard rectangular waveguide transition working at W-Band. The substrate that has been used is 100 μm thick Rogers CuClad ($\epsilon_r = 2.34$ and $tan\delta = 0.009$). According to this, the dimensions obtained are compiled in Table 2.7. A perspective view of the Chebyshev transformer and a top view of the microstrip taper are shown in Figure 2.25.

First, both parts of the transition have been simulated separately using the 3D full-wave simulator HFSS, based on the Finite Element Method. The predicted response of these structures is shown in Figure 2.26.

Figure 2.26(a) shows the simulation result of the microstrip to dielectric filled ridge gap waveguide. An inset showing the structure simulated in HFSS is inserted. The surrounding material is a perfect conductor in order to simulate the circuit packaging. The return loss is better than 20 dB for almost the whole bandwidth. The mean value of return loss is 20.2 dB and the insertion loss has a

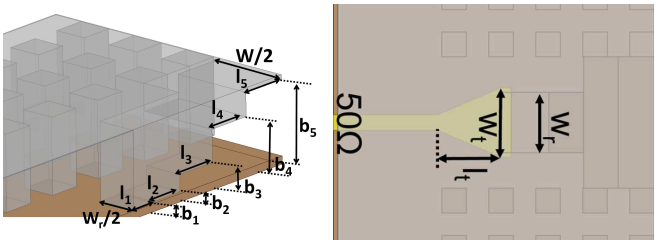

(a) (b)

Figure 2.25: Microstrip to standard rectangular transition: (a) Perspective view of the Chebyshev transformer and (b) Top view of the microstrip taper line.

mean value of 0.2 dB. Figure 2.26(b) shows the ridge gap waveguide to standard waveguide transition performance with an inset of the simulated circuit. It can also be observed that the return loss is better than 20 dB and the insertion loss is almost negligible. The mean value of S_{11} is -20.9 dB and of S_{21} is -0.3 dB.

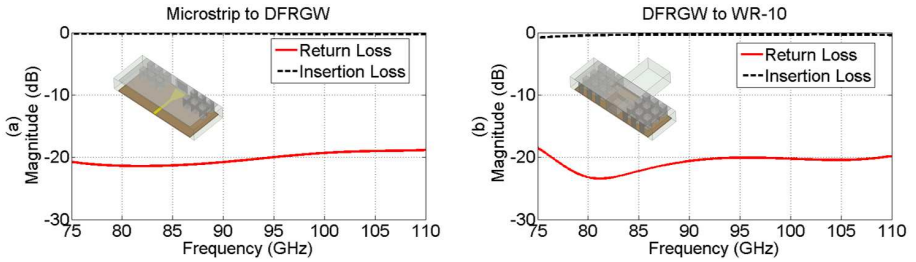

Figure 2.26: Predicted response by using commercial software HFSS: (a) Microstrip to dielectric filled ridge gap waveguide transition.(b) Dielectric filled ridge gap waveguide to standard WR-10 transition. Insertion Loss (Dashed black line) and Return Loss (Solid red line).

The performance of the full transition is shown in Figure 2.27. Since a back-to-back configuration will be used for experimental validation, a comparison between the performance of single and back-to-back configurations is presented in the same Figure. Both transitions are connected by a 5.18 mm long microstrip line.

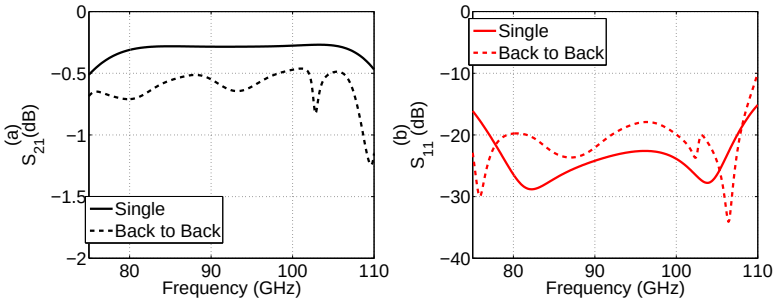

Figure 2.27: Simulation of the scattering parameters for the microstrip to standard WR-10 single (solid line) and back-to-back transitions (dashed line): (a) Insertion Loss and (b) Return Loss.

For the single transition the return loss is better than 20 dB for almost the whole bandwidth (77 - 107.9 GHz). The mean value of the return loss is 23.9 dB and in the whole W-band bandwidth is below 15.74 dB. For the back-to-back configuration the performance slightly degrades: the return loss is now better than 19 dB within the 75 and 108.3 GHz bandwidth. This slight degradation of the return loss performance compared to the single transition is ascribed to the reflections due to the non-perfect matching at both ports. On the other hand, the single configuration presents insertion loss below 0.6 dB and mean value 0.3 dB. The back-to-back transition has maximum insertion loss of 1.3 dB and a mean value of 0.6 dB. This insertion loss increment is mainly caused by the losses associated to the 5.18 mm microstrip line in between both transitions. However, in both cases the insertion loss is below 1 dB and the return loss better than 19 dB.

Figure 2.28 shows that the Quasi-TEM mode of the microstrip is well coupled to the Quasi-TEM mode of the ridge gap waveguide, then the electric field is coupled to the so-called vertical mode of the groove gap waveguide and through this to the standard rectangular waveguide WR-10 TE_{10} mode. We can also notice that the electric field is not propagated through undesired directions thanks to the bed of nails.

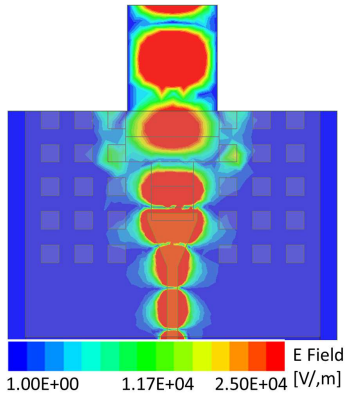

Figure 2.28: Top view of the E-field distribution of the microstrip to WR-10 transition at f = 92.5 GHz.

2.4.5 Experimental Validation

As mentioned above, a back to back transition has been designed for experimental validation. The fabrication process has been split into two parts: a milling process for the metallic component and photolithography for the microstrip taper line. The aluminium block has been realized by CNC machining. The block has been split in the H-Plane. Six screws guarantee the connection between top and bottom parts and four dowel pins the proper alignment. Besides, there are four dowel pins for substrate positioning and alignment. The dimensions of the whole block are 13.65 mm long and 25.05 mm width. The microstrip taper transition has been built in 100 μm thick CuClad substrate ($\epsilon_r = 2.34$ and $\tan\delta = 0.009$) with 15 μm thickness of copper using the standard photolithography process at the Public University of Navarra's facilities. The prototype is shown in Figure 2.29. Figure 2.29(a) shows a top view of the microstrip line mounted on the bottom metallic block and of the upper metallic block, which contains the bed of nails. Figure 2.29(b) is a perspective view of the metallic blocks to see the bed of nails with more details. The whole structure is assembled and connected between the VDI W-Band VNA Extenders as can be seen in Figure 2.30. Then it is measured with the Agilent PNA-X E3861 Microwave Network Analyzer. Previously, the equipment has been calibrated using the standard W-Band TRL (Through-Reflect-Line) calibration kit for VDI extenders.

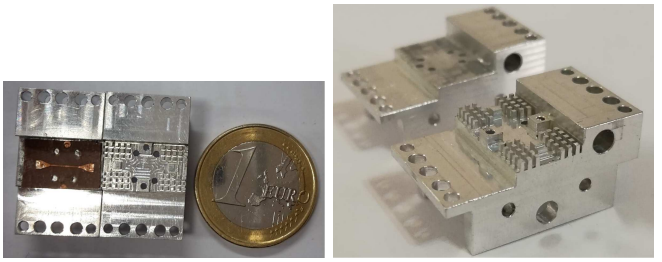

Figure 2.29: Photograph of the fabricated structure: (a) Top view of the aluminium metallic block and microstrip circuit. (b) Perspective view of the aluminium metallic block.

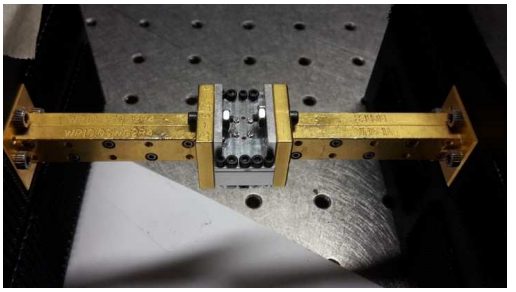

Figure 2.30: Photograph of the assembled and packaged structure connected to the VDI W-Band VNA Extenders.

The results of the measurement and its comparison with predicted response of the back-to-back configuration is shown in Figure 2.31. The simulation of the back-to-back transition has been realized using the dimensions of the fabricated components. These dimensions are shown in Table 2.7. Due to the manufacturing errors, the behaviour has degraded with respect to that shown in Figure 2.27. The insertion losses are slightly higher at the lower half of the bandwidth than in the designed model response. This increase of losses is linked to the larger return losses in this part of the band.

Nevertheless, the simulated insertion loss is lower than 1 dB and the mean value is 0.6 dB. However, the mean measured insertion loss increases 1.3 dB with a maximum of 3.8 dB at higher frequencies. This effect can be ascribed to

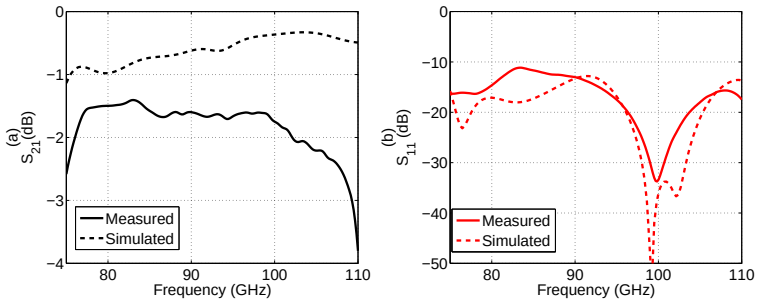

Figure 2.31: Comparison between simulated transition taking into account the fabricated value (dashed line) and measured (solid line) back to back configuration: (a) Insertion Loss and (b) Return Loss.

larger losses in the substrate. Regarding the return loss, the simulated circuit exhibits S_{11} below 14.8 dB and mean value of 19.8 dB, while the measured S_{11} has a mean value of 17.2 dB and the minimum is 33.15 dB at 99.85 GHz.

Summarizing, we can observe that the behaviour of the return loss is quite similar to the predicted evaluation of the prototype once the tolerance fabrication error has been taken into account.

2.5 Microstrip to Waveguide transition based on Ridge-Groove Gap with very simple assembly

The main goal of the prototype presented in this section is the simplification of the design and assembly of the transition presented above. The main disadvantage of the previous design is the necessity of combining ridge and gap waveguide to avoid higher order modes. These higher order modes can propagate in the lower impedance first sections, where both height and width of the steps must be optimized, which makes the design procedure more tedious and not so intuitive. This is avoided in this new prototype, since the substrate does not cover the whole bottom metal part. Therefore, all the groove gap waveguide sections are working in monomode regime. This way the whole process is simplified.

2.5.1 Proposed configuration and simulated performance

The proposed prototype is presented in Figure 2.32. Two different parts can be distinguished: microstrip line printed on dielectric substrate and ridge/groove gap waveguide Chebyshev transformer.

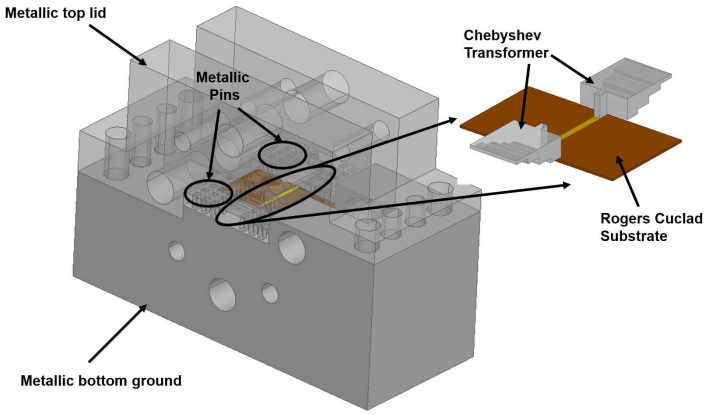

Figure 2.32: 3D perspective view of the microstrip to waveguide transition based on gap waveguide Chebyshev transformer.

The design procedure is based on the same theoretical analysis in which the other transitions presented in this thesis are based, see Section 2.1. The idea is to use a Chebyshev transformer based on ridge and groove gap waveguide technology in which the impedances to match are 50 Ω of the microstrip and 285 Ω corresponding to the standard rectangular waveguide WR-10. The ridge gap waveguide assures the contact between microstrip and the groove waveguide. However, unlike the previous design, in this case the substrate does not fill any step of the transformer and the taper section is avoided. This simplifies the design, since we do not have to split the design in two steps, given the fact that we do not have an intermediate impedance. In addition, as the substrate does not fill the waveguide, any higher order mode is below cut-off.

The frequency design is W-Band, therefore, the pin dimensions are the same already used in Section 2.4. The substrate is Rogers CuClad 233 ($\epsilon = 2.34$ and $\tan\delta = 0.009$) and the width of the groove gap waveguide is 2.65 mm. The rest of dimensions are shown in Table 2.8 and the annotation in Figure. 2.33. These dimensions have been obtained with the procedure in Section 2.1 to obtain S_{11} below -20 dB.

Table 2.8: Dimensions of the transition (μm).

Parameter	Description	Design	Fabricated
w_t	Microstrip width	300	367
w_r	RGW width	325	256
b_0	RGW Height 0	115	158
b_1	GGW Height 1	325	378
b_2	GGW Height 2	700	758
b_3	GGW Height 3	975	957
b_4	GGW Height 4	1195	1053
b_5	GGW Height 5	1270	1253
l_0	RGW length	500	430
l_1	Metal Step length 1	820	826
l_2	Metal step length 2	820	830
l_3	Metal step length 3	820	870
l_4	Metal step length 4	840	807
l_5	Metal step length 5	840	907
w	GGW width	2650	2590
b	WR-10 waveguide height	1270	1280

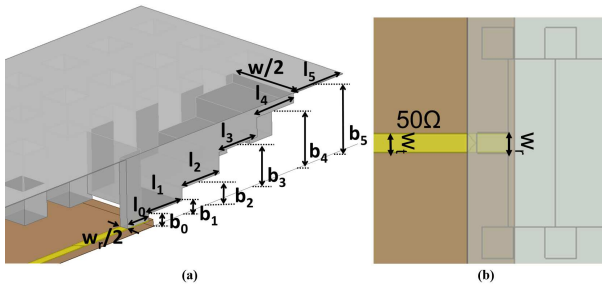

Figure 2.33: Notations of dimensions of the microstrip to waveguide transition: (a) Perspective view of the Chebyshev transformer and (b) Top view of the microstrip to ridge gap waveguide.

The comparison of the predicted response of single and back-to-back configurations is shown in Figure. 2.34. In the back-to-back configuration the transitions are connected by a 5.18 mm long microstrip line. We have used the commercial 3D-fullwave simulator Ansys HFSS.

The single transition has a predicted return loss higher than 15 dB for the whole W-Band and better than 20 dB from 80 GHz to 107.3 GHz. The mean value is 26.68 dB, the minimum is achieved at 88.8 GHz and its value is 37 dB. The insertion loss are less than 0.5 dB and its mean value is 0.27 dB. On the other hand, the back-to-back transition has a return loss higher than 10 dB for the whole band and better than 15 dB from 78 GHz to 107 GHz. The mean value is 19.75 dB and its minimum is achieved at 85.2 GHz where the S_{11} equals 33.23 dB. The insertion loss is less than 1 dB and its mean value is 0.35 dB. The slight degradation of the evaluated performance comparing the single to back-to-back transitions is produced by the small reflections due to the non-perfect matching at both ports.

2.5.2 Manufacturing and experimental validation

A prototype has been evaluated using a back-to-back configuration. The fabrication of the microstrip line has been realized using the standard photlithography process at Public University of Navarra's facilities. The microstrip has been printed on Rogers CuClad 233 ($\epsilon_r = 2.34$ and $\tan\delta = 0.009$) and shaped using the Disco Dicing Saw (DAD232). On the other hand, the metallic block where the Chebyshev transformer and gap waveguide require milling has been

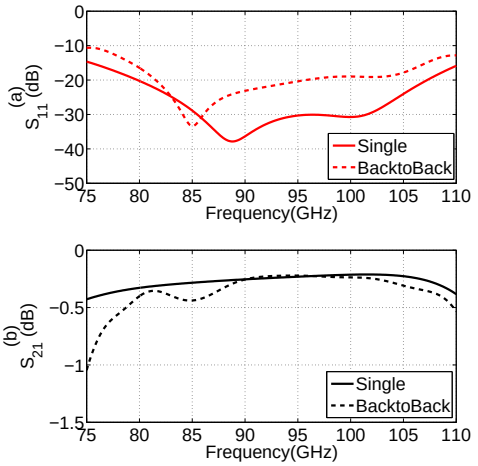

Figure 2.34: Predicted response of the microstrip to waveguide single (solid line) and back to back transition (dashed line): (a) Return Loss and (b) Insertion Loss.

fabricated using CNC machining technique in an external workshop. The split has been realized in H-Plane and four dowel pins guarantee the alignment. Four screws are used for the connection between bottom and top part. No WR-10 section is used, and direct connection to the input and output waveguides is provided by the standard flanges. Figure 2.35(a) shows a picture of the top view of the fabricated prototype. Figure 2.35(b) shows the measurements setup where the back-to-back transition is connected to the VDI W-Band VNA extenders.

The measurement is realized using the Agilent PNA-X E3861 Microwave Network Analyzer. Previously, the measurement equipment has been calibrated by means of the standard W-Band TRL calibration kit for VDI extenders. Finally, the comparison between the predicted performance of the back to back transition, the simulation taking into account manufacturing error and the actual characterized performance is shown in Figure 2.36.

It can be observed that the insertion loss is higher than the simulated one. In the predicted performance of the transition the mean insertion loss is 0.35 dB while in the measured case it increases until 5 dB. The return loss also shows a degradation, in this case the mean value is 11.18 dB instead of 19.75 dB.

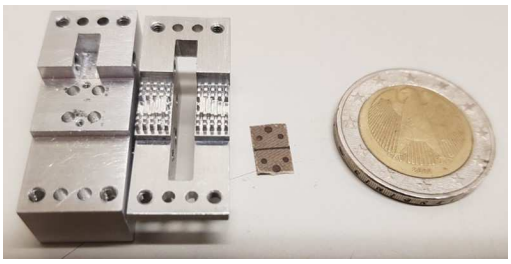

(a)

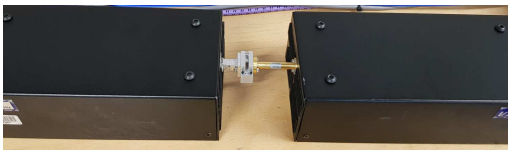

(b)

Figure 2.35: Photograph of the fabricated structure: (a) Top view of the aluminium metallic block and microstrip circuit. (b) Photograph of the assembled back-to-back transition connected to the VDI W-Band VNA extenders.

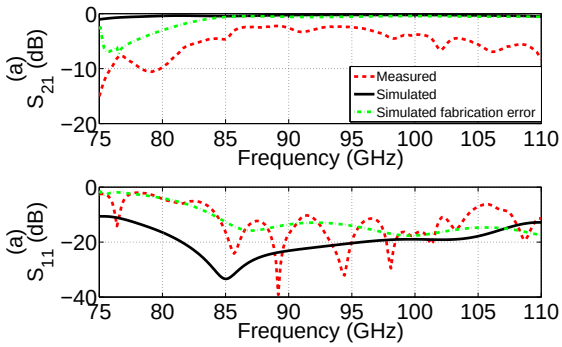

Figure 2.36: Comparison between predicted response (solid line), simulation taking into account manufacturing error (dashed-point green line) and measured performance (dashed line): (a) Insertion loss and (b) Return loss.

This degradation can be associated to the losses ascribed to the substrate but overall due to the manufacturing error. The dashed-point green line shows the performance taking into account the fabricated dimensions of the prototype. In this case the behaviour is more similar to the measured one, and the blue-shift is reproduced. The mean insertion losses and return losses are 1.78 dB and 12.29 dB, respectively. This simulation results can explain the degradation of the transition; however, there are more effects that are causing higher insertion losses. This losses could be caused by some misalignment problems, which provokes the microstrip line and the ridge gap waveguide do not match properly. Another likely effect is a high roughness of the aluminium block, since the higher the roughness the higher the attenuation of a transmission line.

2.6 Conclusions

In this chapter a theoretical method for calculation of the transitions dimensions without optimization, based on small reflections and Chebyshev transformer theories has been presented. This method has been developed for inline configurations and allows for analytic design.

Based on this concept, four different transitions, involving different waveguiding technologies have been developed.

The first studied prototype is a simple inline microstrip to rectangular waveguide transition, which allows for analytical design. The configuration used in this work is simpler and easier to manufacture than other similar inline transitions. The same concept has been applied to an inline microstrip to groove gap waveguide transition, which reduces losses associated to bad contacts in the H-Plane of the waveguide thanks to the use of the bed of nails.

The main disadvantage of these two transitions relies in the required shaping of the substrate, since it must be very precise in order to avoid any misalignment. A solution to this problem has been presented and applied to a microstrip to standard WR-10 waveguide transition, which makes use of gap waveguide technology. Due to the fact that the substrate covers the whole bottom metallic block, problems associated to substrate cutting with a specific shape are avoided, which simplifies manufacturing. However, the first lower impedance steps must be replaced for ridge gap waveguide in order to avoid higher order modes propagation, which gives more complexity to the design process.

Finally, the last transition suppresses the microstrip taper transition, but at the expense of using ridge gap waveguide sections. In this case the substrate does not cover the whole bottom. This way any possibility of high order mode propagation is avoided and the design procedure is simplified.

Summarizing, these transitions are, therefore, a good solution for packaging and characterization of planar circuits such as filters, coupler, MMICs, etc. A comparison between them and the state-of-art of microstrip to waveguide transitions working at similar frequencies is shown in Table 2.9. Finally, we can conclude that the third approach (2.4) is the one which offers the best compromise between fabrication and assembly difficulty and RF performance.

Table 2.9: Performance of millimeter wave rectangular waveguide to microstrip transitions.

REFERENCE	$\|S_{11}\|\,(dB)$	$\|S_{21}\|\,(dB))$	$FrequencyBand$
2.2	12	1.9	W-Band
2.3	12	1.17	W-Band
2.4	17.17	1.3	W-Band
2.5	11.18	5.1	W-Band
[Alg16]	15	1.3	F-Band
[Shi18]	12	2.5	W-Band
[Zha10]	20	1.5	X-Band
[Reb15]	15	1.1	W-Band

Chapter 3

Harmonic Mixers Based on Schottky Diodes with Integrated MMIC based Local Oscillator

A basic frequency mixer is a device whose output is related to the product of two different input signals [Bah88]. Actually, a radiofrequency (RF) signal is downconverted, thanks to an intermodulation process with a local oscillator (LO) signal, to an intermediate frequency (IF). During this process the amplitude and phase modulation of the original signal (RF) is preserved so that is possible to be analysed. An schematic of the downconversion process can be seen in Figure 3.1.

We can consider the mixer as a three port block where the inputs are the LO and RF signals and the output is the IF signal. Taking this into account, we can define the main parameters of a mixer as follows:

Conversion Losses As can be seen in Figure 3.1, the IF signal is proportional to the RF signal, so that there is a loss during the process that can be defined as Conversion Loss:

$$CL(dB) = -10 \log \frac{P_{IF}}{P_{RF}} \tag{3.1}$$

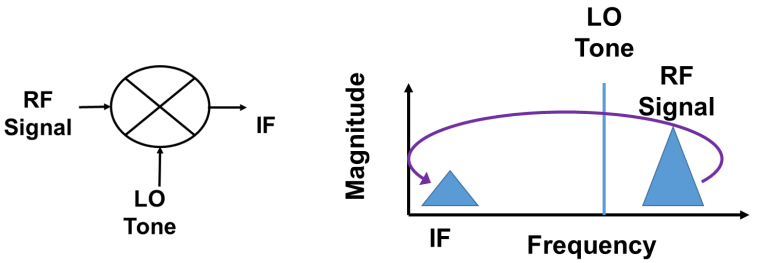

Figure 3.1: Basic frequency mixer schematic (left) and graphic description of the downconversion process of the signals presented at the input and output of a fundamental mixer (right).

Although the power of the local oscillator (P_{LO}) is not explicit in the equation, CL depends on the LO level and it is very important for obtaining reasonable values of CL.

Isolation It is necessary to have the ports isolated between them in order to the signal from one port not affect the signal of the other ports. Although it is impossible to avoid some coupling, at least it is important to maximize isolation, i.e the maximum loss from one port to the other in these cases:

- Isolation RF-IF.
- Isolation LO-IF.
- Isolation LO-RF.

Equivalent Noise Temperature Mixers are electronic components; therefore, as many other electronic devices, they are a source of noise. However, the noise power degrades the final behaviour of the system. That is why noise is an important parameter that must be minimized. The Equivalent Noise Temperature (ENT) is related with the Noise Factor (F) as follows:

$$ENT = (F-1)T_0 \tag{3.2}$$

Where T_0 is the room temperature in Kelvin and the Noise Factor F is defined as:

$$F = \frac{S_i/N_i}{S_o/N_o} \tag{3.3}$$

where S_i and N_i are the input power and noise, respectively, and S_o and N_o are the output power and noise. Note that in this definition the noise at the mixer input, N_i, is that given by a load at room temperature, i.e. $N_i = kT_0B$, where B is the bandwidth. Therefore, the Noise Factor evaluates the Signal to Noise degradation.

Sensitivity Another important parameter is the sensitivity of the receiver, defined as the smallest change of temperature that can be measured. It is computed as follows:

$$\Delta T = \frac{T_{sys}}{\sqrt{B\tau}} \tag{3.4}$$

where T_{sys} is the noise temperature of the receiver system, B is the bandwidth and τ is the integration time. The bandwidth is usually fixed by the specific application. The integration time will typically depend on the system requirements, e.g. spatial resolution, and will be limited by system drift. Therefore, the sensitivity will be determined mostly by the noise of the receiver. This parameter must be as low as possible and will depend on the choice of the technology and the design of the receiver.

In order to do the mixing process we need non-linear elements such as transistors or diodes. However, the lack of availability of these devices to work at submillimetre wave and terahertz ranges, besides the non-existence of THz sources, provoked a gap in this part of the spectrum. Nevertheless, during the last four decades, the THz gap has been reduced thanks to research progress in miniaturization of components that allows the design of submillimeter wave frequency multipliers and mixers [Sob11a, Zha16, Wan09, Tho05].

The main application for THz mixers are related to the heterodyne receivers for satellites imaging, such as Earth observation and atmospheric studies, but also, for high data rate communication system. Among all the technologies that can be used for mixing, Schottky diodes are the best options due to their room temperature operation, in addition to their capability of fast modulation. In addition to this, Schottky diode mixers present another important advantage, since they can be implemented in planar technology, which provides good integration and compact designs. Beyond 400 GHz other solutions such as GaAs membrane or even substrateless technologies are taking relevance over planar circuits for the integration of Schottky diode mixers.

Nonetheless, it is still a troublesome task to find sources with enough power to work as local oscillator in this frequency range. The standard procedure consists on the design of efficient multipliers in order to, starting from a low

frequency signal, achieve the frequency needed by the LO in our mixer circuit. However, this solution is either not always possible or it consists of several stages of frequency multiplication, what entails to a bulky and expensive system which can suffer from losses due to misalignments in the multiple interfaces.

This inconvenience has motivated that several integrated THz receivers have been proposed during the last years [Fed10, Tho08a, Tre10, Ede07, Rec15, Tho10a]. Nevertheless, in these designs the local oscillator is still external, built as an independently packaged element. Therefore, the local oscillator still needs a connection to the mixer. Usually this is a flange connection that requires expensive machining to assure good alignment. The most compact configuration found in the literature corresponds to [Rec15], although frequency multipliers and mixers are in different layers or substrates, which may introduce some misalignments.

That is why in this work we present two different harmonic mixers based on Schottky diodes [Mae15, Mic13, Den18] which integrate a MMIC based source at W-Band as local oscillator. The first circuit is a fourth-harmonic mixer. This configuration has been chosen because it is easier to find local oscillator developed on planar technology with enough power to pump the diodes at lower frequencies than at higher frequencies. Furthermore, using planar technology for both designs, i.e. the mixer and the local oscillator, allows the integration on the same housing metallic block. The second one is a combined doubler/subharmonic mixer that also uses the same 75 GHz MMIC based source. This solution integrates in the same substrate the doubler and the mixer, which share the same metallic packaging with the MMIC source. Taking advantage of this integration we have a configuration similar to a fourth harmonic mixer, but with the performance of a subharmonic mixer.

The main advantage of both circuits that are presented in this work consists in the integration of MMIC source as local oscillator and the mixers in the same metallic blocks. Since only one block is used, flange connection is avoided, this way misalignment errors are also prevented. Besides this advantage, the compactness is also very remarkable, insomuch as this means reduction of weight. Size and weight reduction are of great interest for applications in the field of space or communications. Both designs are realized with the traditional E-split block waveguide architecture.

3.1 MMIC Local Oscillator

An oscillator is a component able to provide a RF signal from DC voltage. In general, local oscillators are composed of:

- A resonant structure whose own resonant frequency works around the operational frequency of the final oscillator.
- An amplifier element.
- A coupling structure that optimizes the behaviour of the oscillator.

Usually, the LO output is mixed with other signal in order to obtain the intermediate frequency, therefore it is important to achieve both the correct operational frequency and the stability.

In this work, the local oscillator (LO) is composed of the following TriQuint flip-chip components [Tri19]: a voltage-controlled oscillator (VCO) with 19 GHz output (TGV2204-FC) and two frequency doublers (TGC4703-FC and TGC4704-FC) in order to obtain a total frequency range from 74 GHz to 78 GHz with around 10 dBm output power. The material used to implement the printed circuit board (PCB) of this LO is Rogers 3210 and a schematic of this circuit can be seen in Figure 3.2.

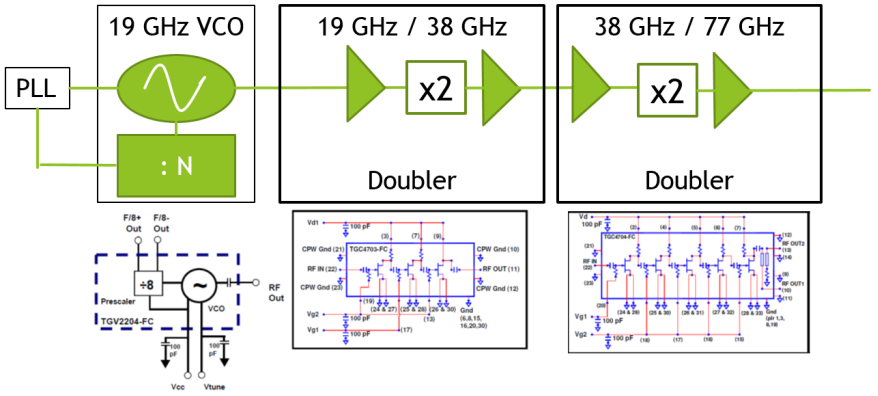

Figure 3.2: Schematic of the local oscillator based on Triquint Semiconductor flip chips. The VCO is based on chip TGV2204-FC, the first doubler on TGC4703-FC and the second doubler on TGC4704-FC.

In order to tune accurately the LO output frequency and to stabilize the VCO, a 2.4 GHz Phase-Locked Loop (PLL) has been designed, based on the fractional frequency synthesizer ADF4158 from Analog Devices. This synthesizer has a maximum output voltage equal to 3 V. Since the VCO control voltage is in the range from 0 to 8 V and with the objective of increasing the total frequency range, i.e. to be able to tune the LO frequency from 74 GHz to 78 GHz, an active loop filter that uses the operational amplifier (OP184) and a basic RC low pass filter is applied.

The output frequency of the local oscillator has been measured using Keysight PXA Signal Analyzer N9030A and its Keysight Harmonic Mixer M1970W extender (75-110 GHz) in order to check that the output frequency is controlled with the tuning voltage of the VCO. Figure 3.3 shows the output frequency characterization versus the tuning voltage.

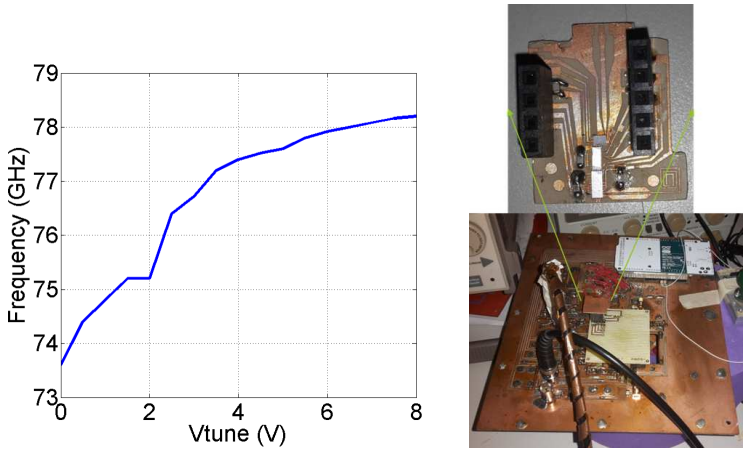

(a) (b)

Figure 3.3: (a) Frequency output versus tuning voltage of the MMIC LO. (b) Picture of the board with MMIC LO PCB with PLL for characterization. (Inset) MMIC LO detail.

It has been checked that the frequency changes monotonously with the VCO tuning voltage between 74 GHz to 78 GHz. In Figure 3.3 a picture of the PLL board in which the MMIC LO is connected in order to control the oscillation frequency is also shown.

3.2 Fourth harmonic mixer

Sometimes, it is difficult to find sources at millimetre or sub-millimetre waves with enough power to pump the diodes in order to work properly. In our case we are interested in using a local oscillator based on planar technology so that it can be integrated with the mixer in the same metallic block. For this planar technology it is even harder to find oscillators with enough power. That is why it may be necessary to work with lower LO frequency, W-band in this case, and extract the information of the fourth harmonic instead of the second harmonic mixing product. In this case we will have higher conversion losses and equivalent noise temperature; however, we have the advantage of simplified LO generation.

In this section the design procedure for a fourth harmonic mixer working at 300 GHz with a local oscillator at 74-78 GHz will be described. A 3D view of the whole model can be seen in Figure 3.4.

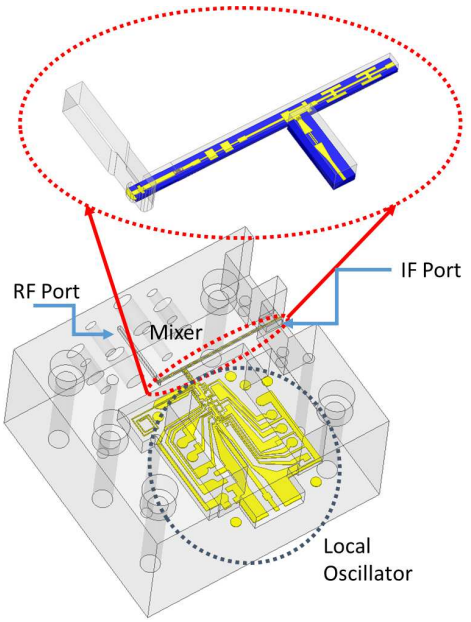

Figure 3.4: 3D perspective view of the fourth harmonic mixer.

3.2.1 Design topology

The proposed configuration is based on the use of Schottky diodes to do the harmonic mixing. For fourth harmonic mixing, which is our case, it is convenient to work with the antiparallel configuration of Schottky diodes, insomuch as the even harmonic are suppressed and we have higher conversion efficiency in the odd harmonics. In this work, moreover, we have chosen four diodes due to the fact that we are going to work with high LO power. Using more diodes avoids overheating and malfunction that may happen when working with the high temperature produced by the high LO power.

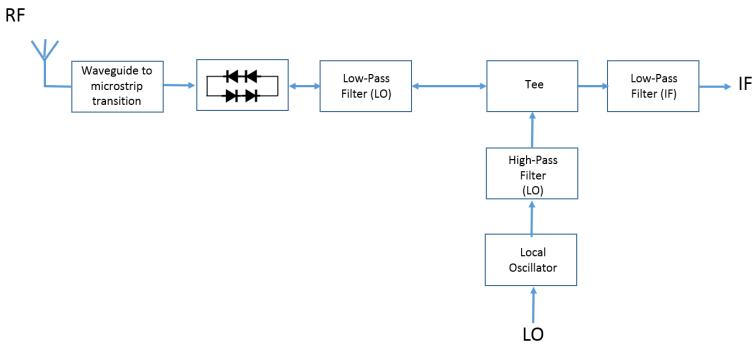

Figure 3.5: Schematic of the fourth harmonic mixer with integrated Local Oscillator.

An schematic can be seen in Figure 3.5. We can observe that the radiofrequency signal is received by an antenna and then coupled from the rectangular waveguide to the microstrip line. A matching line connects with the diodes and a low pass filter is necessary in order to isolate the IF and LO ports from the RF signal. A filter to reject the LO signal from the IF port is also essential. Finally, a high-pass filter isolates the LO from the IF and DC signals.

The design of the mixer consists of two process. The first one is based on the analysis of the passive circuits and also the passive behaviour of the Schottky diodes. This linear analysis is realized with the Finite Element software Ansys HFSS. The second step consists on the analysis of the non-linear behaviour of the diodes. The software used for the active analysis is Keysight ADS and the passive elements are introduced as data items with S-Parameters.

3.2.2 3D-Model of the Diode

The diodes are UMS Schottky varistor diodes with 1×3 μm anode size. The layers of the Schottky diode are defined by the UMS foundry manufacturing process [UMS19]. This junction exhibits a 7.3 Ω resistance, 5.14 fF junction capacitance, ideality factor n = 1.2 and forward turn-on voltage Vj = 0.65 V. The cutoff frequency of this diode is 3 THz which allows us to work at 300 GHz. An schematic view of the layers of the UMS Schottky diodes can be seen in Figure 3.6.

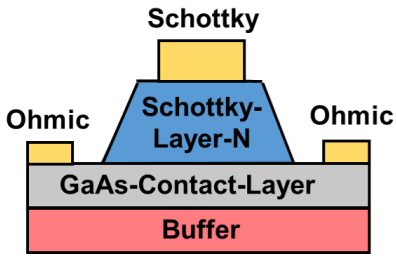

Figure 3.6: Layers of UMS Schottky Diode.

A 3D model of the Schottky diodes has been implemented in HFSS using the foundry design kit given by UMS. An schematic of the diodes in antiparallel configuration can be seen in Figure 3.7. They are simulated in HFSS in order to take into account the parasitic effects that happen in the structure and be able to realize a more realistic impedance matching.

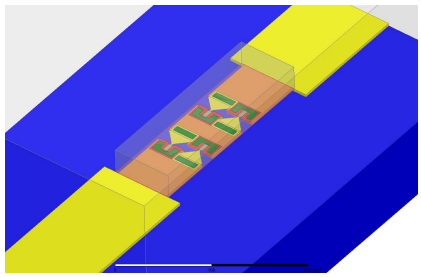

Figure 3.7: HFSS model of four diodes in antiparallel configuration.

The diodes are placed on the selected substrate, i.e. Topas COC [Mae14b]

($\epsilon_r = 2.2$ and $\tan\delta = 0.0009$) and an air channel to simulate the metallic block environment in which they will be placed is also necessary. It is important to notice that the obtained S parameters must be deembedded taking into account the length of the input and output microstrip lines until the reference plane of the diode.

3.2.3 Passive Circuit Design

As it has been already mentioned, the design of the mixer is separated into two different steps. The first part, which corresponds to the linear behaviour of the different mixer components, is explained below. The dimensions of all the circuits are gathered in Appendix B. The circuits are implemented over substrate Topas COC ($\epsilon_r = 2.2$ and $\tan\delta = 0.0009$) and the metal is copper.

Filters

A top view of the filters and their simulated response are shown in Figure 3.8.

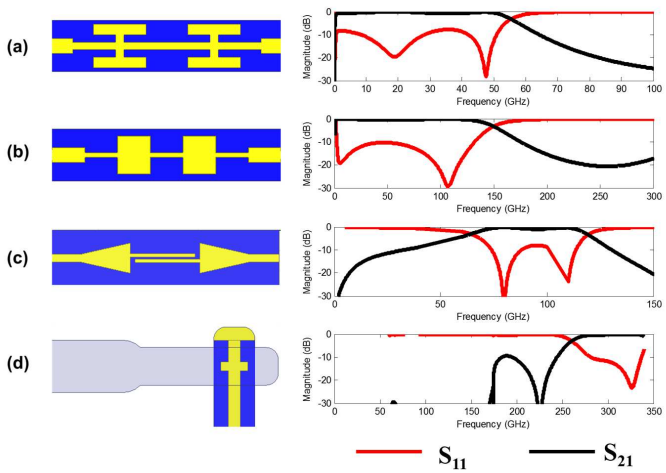

Figure 3.8: Top view and predicted response of the fourth-harmonic mixer passive circuits: (a) IF low-pass filter, (b) LO low-pass filter, (c) High-pass filter (d) E-Probe transition between waveguide and microstrip for RF.

The first filter corresponds to the low-pass filter for IF frequency. In this case we have chosen the hammerhead configuration, Figure 3.8(a), because of its compactness and good rejection. It presents rejection for the LO signal below 15 dB, achieving 22 dB in some frequencies. The cutoff frequency is 55 GHz, which is high enough for our design, given the fact that the IF will not be higher than 20 GHz.

The RF low-pass filter rejects the RF and lets only pass the LO. A stepped impedance configuration has been chosen, Figure 3.8(b). This kind of filter, which consists of quarter wavelength long alternating low and high impedance sections, presents good rejection and a wide bandwidth. As we can notice, the structure presents low losses for the LO and a rejection higher than 15 dB for the RF signal. It is also important that it lets the DC goes through. However, despite of the great advantages of the stepped impedance filter, they present an inconvenience: they may be very long and other alternatives must be used in some cases.

Finally, the last filter we need is a high-pass filter, in this case a DC-Block, which lets the LO signal pass to the circuit and rejects the other frequencies, Figure 3.8(c). We can see that the low frequencies are rejected and the LO band is able to go through this structure with low losses.

Waveguide Probes

As it was previously mentioned, a transition that couples the signal received in the antenna to the microstrip line in which the planar filters and Schottky diodes are implemented is necessary. The goal when we design this kind of transition is to minimize insertion losses at the RF frequency. Furthermore, the transition is important insomuch as it works as a high-pass filter for the IF and the LO signals, so that the rejection at the RF port is high. Finally, it should provide the required ground for the DC signal.

In this work we have designed a standard waveguide to microstrip transition, Figure 3.8(d). That means an E-field probe that couples the Quasi-TEM mode of the microstrip to the TE_{10} mode of the waveguide. The insertion losses are negligible (below 0.25 dB) from 270 to 330 GHz which give us wide enough bandwidth. The return losses are more than 15 dB for this bandwidth, whereas the LO signal is completely rejected, since this frequency is below the cutoff frequency of the RF waveguide.

Matching lines

The dimensions of the matching lines are calculated by means of the Load-Pull technique [Sys11] to match the optimum impedances of the diodes so that their conversion losses are minimum.

3.2.4 Non-linear analysis

For the non-linear analysis we use the Schottky diode model from United Monolithic Semiconductors (UMS) foundry [UMS19]. The S-Parameters of the mixer are imported to Keysight ADS software for the non-linear analysis.

Using the Load-Pull technique all the impedances in the Smith Chart are analysed and the optimum embedding impedance, i.e. the impedance which provides the best conversion loss, is determined. The load-pull technique refers to the process in which the impedance presented in one of the port of a device under test (DUT) is varied in order to evaluate its performance. The optimal conditions are established very quickly and also the optimum performance that we obtain with these load impedances. This step is necessary to know the maximum efficiency that is possible to achieve using the DUT and the load impedance which is needed to match the rest of the circuit in order to obtain that performance. It is important to say that the impedance we are matching is the impedance of the Schottky diodes over the substrate, so that the effect of the diode block, substrate and microstrip line have been taken into account. Then, the RF low-pass filter and the waveguide transition are used to match the embedding impedance of the diodes. The interface of the diode is placed in the port of the microstrip of the corresponding circuit as can be seen in Figure 3.9(a) and a deembeding is realized for the length of the diode interface. An image of the Load-Pull result for RF and LO frequencies is shown in Figure 3.9(b).

The minimum conversion losses of the ideal mixer are obtained with diode embedding impedances $Z_{LO} = 135 - j108\ \Omega$ and $Z_{RF} = 99 - j72\ \Omega$ for LO and RF, respectively. The LO input power has been swept from 6 dBm to 12 dBm and its frequency from 74-77 GHz. For the RF input, a -30 dBm signal is applied. It is important to use in this analysis an order of at least 11 harmonics to ensure the results are accurate enough.

The conversion losses (CL) and the equivalent noise temperature (ENT) of the whole fourth-harmonic mixer are shown in Figure 3.10. We can observe that the minimum is achieved at 302 GHz with 11 dB conversion loss and 3900 K equivalent noise temperature when the LO power is 12 dBm. The 3-dB bandwidth is 9 GHz (between 298 and 307 GHz), which represents a 3 %. The

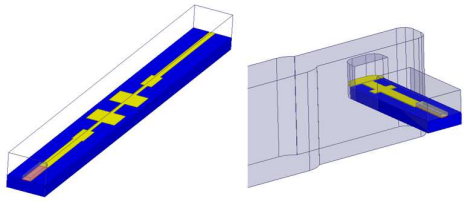

(a)

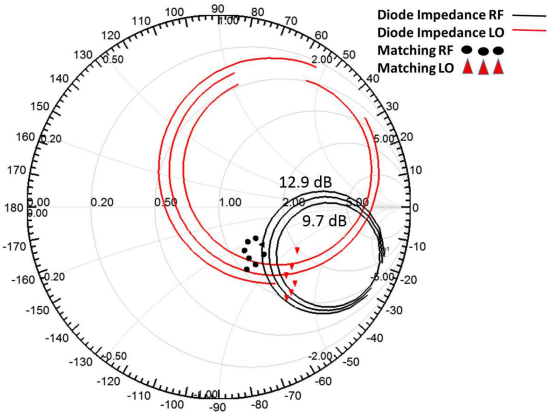

(b)

Figure 3.9: (a)Perspective view of the RF low pass filter and waveguide to microstrip transition with the diode interface for impedance matching. (b) Smith Chart with matching representation. Red solid line corresponds to the diode impedance at LO frequency and black line to RF frequency. Black circles are the S_{11} for the waveguide transition with diode interface and red triangles for the LPF with diode interface for different matching line lenghts.

mean equivalent noise temperature is around 6800 K and the mean conversion loss 13.3 dB. For 10 dBm LO power the mean conversion loss is 15 dB and the ENT is 7300 K. If the LO power reduces to 8 dBm and 6 dBm the mean CL increase to 15 and 17 dB and the ENT to 10700 K and 12300 K, respectively.

The obtained conversion losses are slightly higher than the state-of-the-art subharmonic mixers and the circuit is also slightly more noisy. However, if

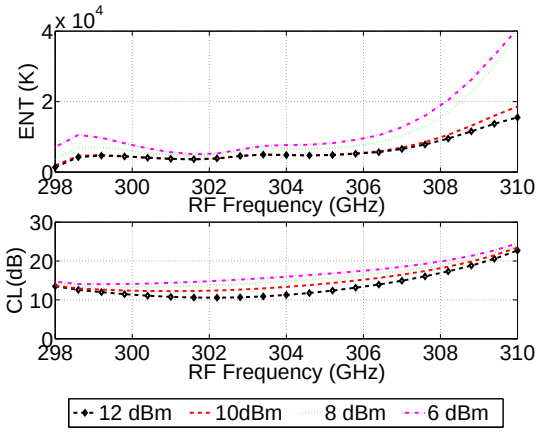

Figure 3.10: Fourth harmonic mixer predicted performance for different LO power.

these results are compared with those obtained with fourth harmonic mixers, see Table 3.1 we can see that this performance is similar to the state-of-the art. Nonetheless, this configuration presents the advantage of being simpler an compacter.

Table 3.1: State of the art of fourth harmonic Schottky diode mixers working at frequencies similar to this work.

Ref	Frequency (GHz)	CL (dB)	ENT (K)
[Li16]	369-477	14	-
[Mae14a]	430-460	14	10000
[Den18]	320-500	18	-
This work	298-310	15	10700

3.2.5 Thermal Analysis

The required LO power, around 12 dBm, can be very high for only two diodes, since their temperature might rise and damage the diodes. That is why we use

four diodes instead of only two. This way it is possible to manage more power without their behaviour deteriorating.

Just to be sure that the antiparallel configuration of four diodes is able to manage all the power that the LO is going to provide, a thermal analysis is performed. This analysis allows us to check that the operational working temperature is below the critical temperature recommended by the foundry, which in this case is 174 °C. However, around 100 °C malfunction starts and the performance deteriorates, according to the UMS Foundry manual.

In order to do this analysis the thermal module of the commercial software CST is used. We can observe, see Figure 3.11, that the maximum temperature is around 54 °C, which, according to the foundry data-sheets, is low enough for proper functioning.

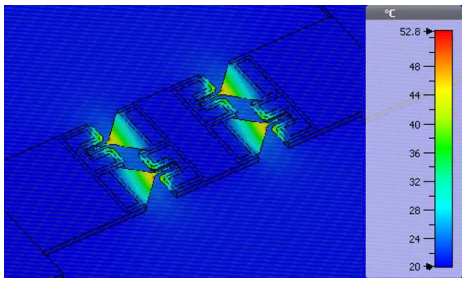

Figure 3.11: Thermal analysis results.

3.3 Combined doubler/sub-harmonic mixer

As an alternative to the fourth-harmonic mixer described in the previous section, the design of a combined frequency doubler/subharmonic mixer will be considered next. In the previous design, the fourth-harmonic mixer, it was pointed out that the main advantage of using this configuration instead of a subharmonic is that, LO frequency is halved thus the power we have in local oscillator can be higher. However, the main disadvantage is the higher conversion losses compared with the subharmonic version.

In the configuration presented in this section, however, frequency doubler and subharmonic mixer are integrated on the same substrate, which leads to a performance similar to that of a subharmonic mixer with the configuration of fourth harmonic mixer in terms of frequency. In addition, such integration leads to significant reduction in mass and volume allowing, e.g. building multi-pixel arrays of heterodyne receivers for imaging applications[Wan08].

3.3.1 Design Topology

The 3D whole model of the 300 GHz combined frequency doubler - subharmonic mixer with integrated MMIC source in a single packaging metallic block is shown in Figure 3.12. The layout of the combined doubler-mixer can be seen in the inset of this figure.

The corresponding schematic is shown in Figure 3.13. The radiofrequency signal is collected by a horn antenna (not shown) and then coupled from the input WR03 rectangular waveguide to a microstrip line. The source signal at frequency f_{IN} feeds a frequency doubler, which generates the LO signal for the subharmonic mixer. Thus, $f_{LO} = 2 \times f_{IN}$. The subharmonic mixer is based on an antiparallel Schottky diode pair. The frequency doubler uses a four diode antiseries chip with bias, which forces the use of additional DC-blocks.

The MMIC source is built on a different substrate (Rogers 3210) and wire bonded to the mixer substrate at the point IN in Fig. 3.13. After the bonding that connects both substrates, a DC-block (DC-Block 1)is mandatory to avoid the DC bias of the frequency doubler diodes leaking to the MMIC source. In addition, the DC bias requires a low-pass filter to avoid leakage of the source signal (LPF DC-Bias) and a second DC-block at the doubler output (DC-Block2). Finally, the multiplier also needs a low-pass filter (LPF1) that lets the IN signal reach the diodes but rejects the doubler output, preventing it from reaching the MMIC source.

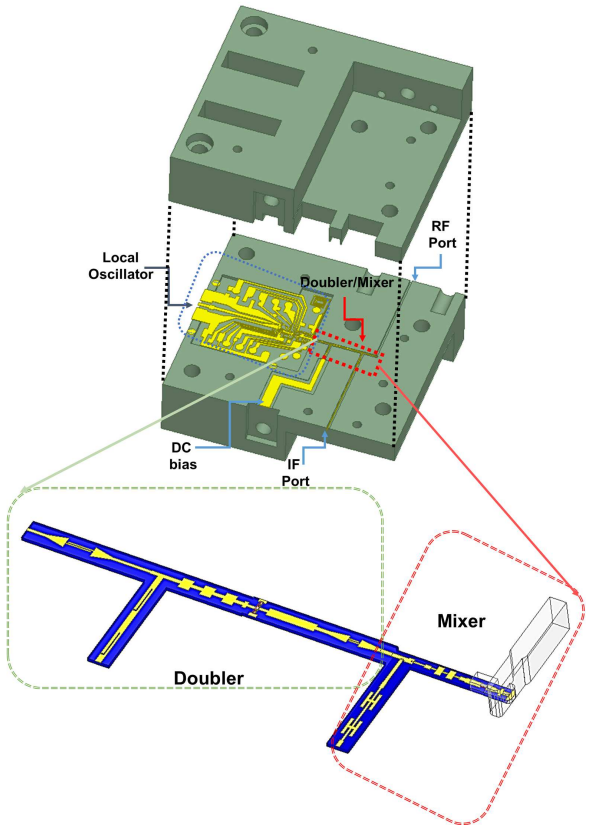

Figure 3.12: Exploded view of the 3D model of the combined doubler-subharmonic mixer with integrated MMIC based LO.

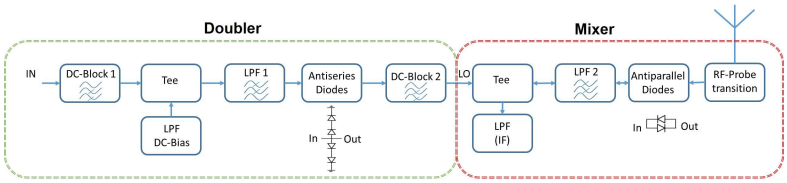

Figure 3.13: Schematic of the combined doubler/mixer circuit.

The subharmonic mixer requires a low pass filter (LPF2), which lets the LO signal (i.e. the output of the doubler) pump the diodes and blocks the RF frequency. In addition, the waveguide probe that receives the RF signal and couples it to the microstrip line acts as a high pass filter that rejects the lower frequency signals at the RF port. Finally, the IF output is formed by a tee with a low-pass filter for IF frequency, which blocks the RF and LO signals.

The design started with the frequency doubler as an independent device [Zha16, Zha11]. Afterwards, the subharmonic mixer was optimized, taking into account the output power of the doubler as the input LO [Meh98, Tho09]. Once both designs have been finished, they are evaluated together.

3.3.2 3D-Model of the Diodes

Frequency doubler

The MMIC source needs to be doubled to be used as a local oscillator to the subharmonic mixer. The MMIC source power at 75 Ghz is relatively high, around 10 dBm. Therefore, we use a four diodes antiseries flip-chip with bias, which allows to have enough power to pump the mixer diodes, but also to dissipate the heat generated. As it was explained, high temperature may damage the diodes.

The diode model is the same presented in Section 3.2.2. A 3D view can be seen in Figure 3.14.

Subharmonic mixer

The antiparallel configuration, as was described in Section 1.2.3, promotes the odd harmonic mixing and cancel the even harmonics. However, in this configuration we only use two diodes instead of four since the LO power, which is the

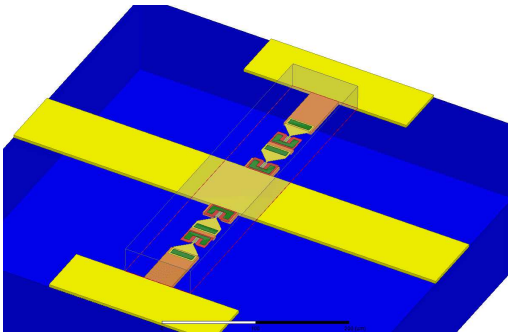

Figure 3.14: 3D illustration of the antiseries diodes used for HFSS simulation of the frequency doubler.

output of the doubler, in this case is not very high (around 2 dBm). A 3D view can be seen in Figure 3.15.

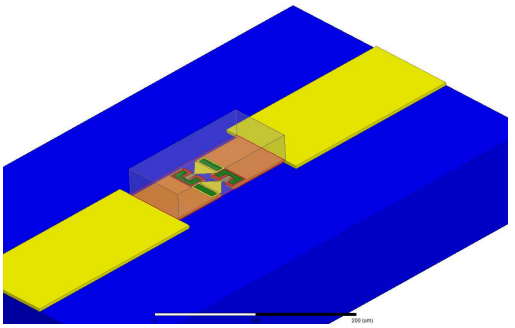

Figure 3.15: 3D illustration of the antiparallel diodes used for HFSS simulation of the subharmonic mixer.

As it happens with the fourth-harmonic mixer, the diodes are placed on COC substrate Topas ($\epsilon_r = 2.2$ and $\tan\delta = 0.0009$) and an air channel to simulate the metallic block environment in which they will be placed is also necessary.

3.3.3 Passive Circuit Design

The analysis of the different passive circuits, e.g. filters, DC-blocks and transitions, is considered in this section. The circuits are implemented over COC substrate Topas with 2 μm of copper. The software we have used for simulation is Ansys HFSS.

Firstly, the components of the frequency doubler are discussed. A top view of these elements and their predicted response are shown in Figure 3.16.

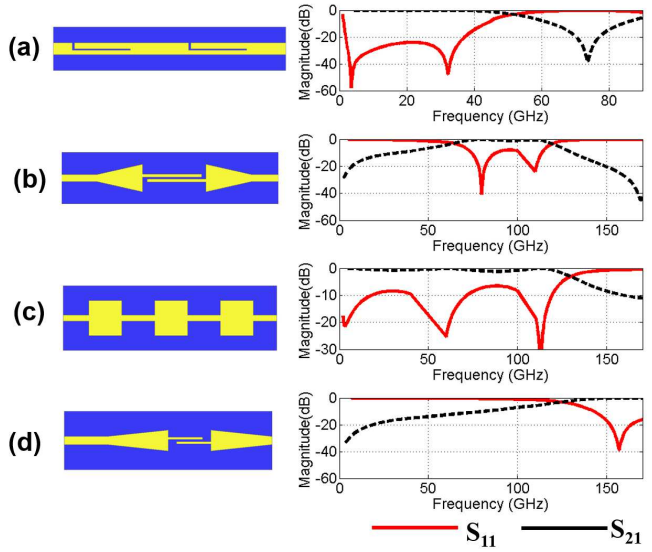

Figure 3.16: Top view and predicted response of the frequency doubler passive circuits: (a) Low pass filter for DC-Bias, (b) DC-Block 1 for MMIC source, (c) Stepped impedance low pass filter (LPF1) and (d) DC-Block 2 for LO.

The first filter that can be observed, filter (a) (LPF DC-Bias), is the low-pass filter of the DC-Bias. The cut-off frequency is 50 GHz, which allows the DC voltage to pass and provides around 25 dB rejection at MMIC source frequency (f_{IN}). The second filter (DC-Block 1) is a high-pass filter with 65 GHz cutoff frequency and 0.35 dB insertion loss at IN frequency. In Figure 3.16(c) we can see the stepped impedance low pass filter (LPF 1). This kind of filter presents a great advantage for our design, since the required low impedance section

widths are relatively narrow, which avoids higher order mode propagation in the channel. The rejection for LO is about 10 dB and the IN signal is in the pass band with low insertion losses. Finally, the last filter, (d), is another DC-Block (DC-Block 2), which rejects the IN signal with more than 12 dB insertion loss and lets only the LO signal reach the subhamonic mixer circuit. The dimensions of all these circuits are compiled in Appendix B.

The layout of the subharmonic mixer circuit components and its response is shown in Figure 3.17. First, IF output low-pass filter (LPF IF), which lets only the IF signal pass and rejects the higher frequencies, is shown in Figure 3.17(a). The hammerhead configuration has been chosen because of its compactness and high rejection, about 20 dB for LO signal (i.e. the output of the doubler). The low-pass filter that rejects the RF signal (LPF 2) is again a stepped-impedance low-pass filter, whose rejection is 20 dB. The last element shown in Figure 3.17(c) is the waveguide probe that couples the RF signal to the microstrip. The probe is short-circuited, which provides the DC return for the diodes. Its insertion losses are lower than 0.5 dB from 276 GHz to 330 GHz.

The isolation between ports is another important parameter we have to take into account when design a mixer. This parameter measures the amount of power that leaks from one port to another one. If the leakage is high, the signal interferes with the other port signal degradating the final behaviour of the circuit. In this case, it is about 30 dB for LO signal at IF port. As the RF port is a waveguide probe and both IF and LO are below the cutoff frequency, isolation for this port is beyond 60 dB.

Finally, the length and width of the matching lines are calculated in order to adjust the diodes embedding impedance for best performance.

3.3.4 Non-linear analysis

The Load-Pull technique is used to obtain the embedding impedance of the diodes for best performance at f_{IN}, i.e. the MMIC source frequency which is the input of the doubler, and at f_{LO}, i.e. the output of the frequency doubler and LO and at RF frequency for the subharmonic mixer. The results of the Load-Pull analysis, carried out to match the diodes on the substrate with the filters and the probe transition, are shown in Figure 3.18.

The minimum conversion losses of the mixer are obtained with diode embedding impedance $Z_{RF} = 28 - j11$ and $Z_{LO} = 90.59 - j46.6$ for RF and LO frequency, respectively. For the frequency doubler, the minimum conversion losses are obtained for diode embedding impedance $Z_{LO} = 90 - j86$ and $Z_{IN} = 223 - j136$ for LO and IN frequency, respectively.

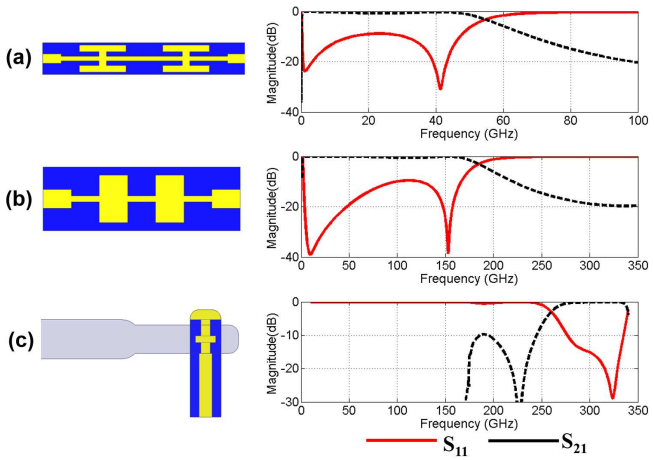

Figure 3.17: Top view and predicted response of passive circuits used in the subharmonic mixer: (a) IF Hammer-head filter, (b) Stepped impedance LPF for RF rejection and (c) RF E-Probe transition between waveguide and microstrip.

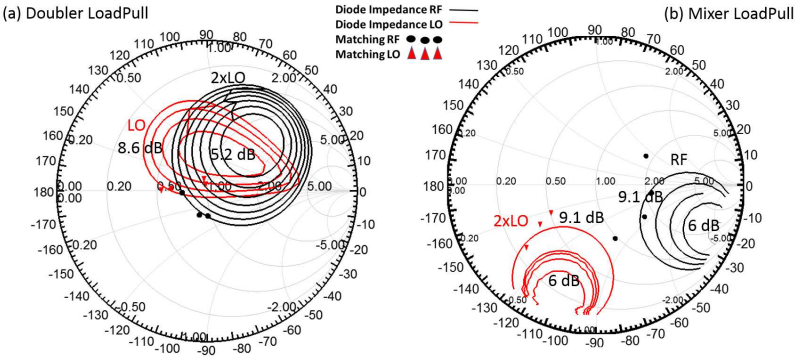

Figure 3.18: Load-Pull analysis results and matching procedure:(a) Doubler frequency multiplier and (b) Subharmonic mixer.

For the frequency doubler analysis we have swept the input power from 6 dBm to 12 dBm, since the nominal output power of the 38 GHz Triquint

TGV4704-FC frequency multiplier will be around 10 dBm. From the analysis realized in ADS we predicted the output power of the doubler and therefore its efficiency. These results are shown in Figure 3.19.

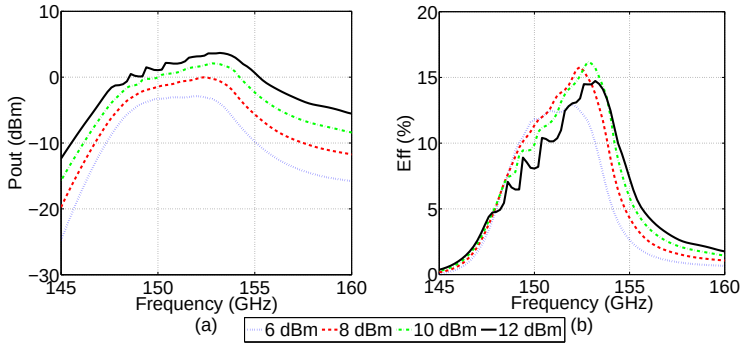

Figure 3.19: Predicted response of the frequency doubler for different LO input power levels: (a) Output power and (b) Efficiency.

We can observe that the output power is above 0 dBm from 147 GHz to 154 GHz for 12 dBm and 10 dBm IN power. In case of 8 dBm IN power the output signal of the doubler is above 0 dBm from 150 GHz to 153 GHz. For 6 dBm the output power is below 0 dBm, which may be insufficient to pump the mixer diodes. The efficiency in this bandwidth is higher than 10 % for all cases. For 12, 10 and 8 dBm, where the output is around 4, 2 and 0 dBm, the efficiency is 15 %. For 6 dBm the output is around -3 dBm, therefore the efficiency is around 12 %. Thus, the doubler is narrow band but its bandwidth is enough for our design, since it covers the range of frequencies generated by the MMIC source. These results were obtained using -1.16 V DC bias.

On the other hand, in the subharmonic mixer case, -30 dBm RF input has been considered for the harmonic balance analysis. The RF frequency has been swept, keeping the IF fixed to 2 GHz ($f_{RF} = 2 \times f_{LO} + f_{IF} = 4 \times f_{IN} + f_{IF}$). Finally, the whole circuit is evaluated with HFSS and ADS combination for different power levels of the doubler local oscillator. The predicted results are shown in Figure 3.20.

The conversion loss of the mixer for 12 dBm IN power is around 8.5 dB from 300 GHz to 307 GHz and the mean value for the whole band, from 298 GHz to 310 GHz, is 9.6 dB. The mean DSB Equivalent Noise Temperature (ENT) is 1300 K. For 10 dBm IN power the mean performance of the mixer in this

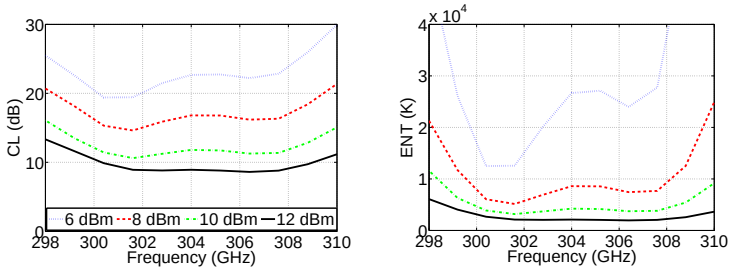

Figure 3.20: Predicted results of combined frequency doubler/subharmonic mixer for for different MMIC source power levels: (a) Conversion Loss and (b) DSB Equivalent Noise Temperature.

frequency range is: 11 dBm CL and 1900 K ENT. These values are similar to those shown in the literature. However, the performance of the mixer for 8 and 6 dBm IN power shows a significant degradation. For 8 dBm the conversion loss becomes 18.1 dBm and the DSB ENT is 8100 K. For 6 dBm the mixer performance significantly degrades, the average DSB ENT increases to around 38000 K and the CL to 23.8 dB. Summarizing, with enough power at the input, i.e. more than 8 dBm, the doubler provides enough power to pump the subharmonic mixer. Otherwise, the performance significantly degrades. Table 3.2 shows a comparison between this work and the state-of-the-art for mixers around 300 GHz.

Table 3.2: State of the art of Schottky diode subharmonic mixers working at similar frequencies to this work.

Ref	Frequency (GHz)	CL (dB)	ENT (K)
[Tho05]	300-360	6.5	1270
[Tho08a]	365-395	10	2500
[Rec15]	320-350	8	2000
[Guo18]	290-310	9-10	2000-2600
[Tho08b]	320-360	10-11	N.A
[Sob11b]	320-360	9	3000
Combined doubler/mixer	298-310	11	1900

3.3.5 Thermal analysis

The safety temperature of the diodes is the same as for fourth harmonic mixer, Section 3.2.5. The analysis is done using the Thermal Solver of CST studio for the four diodes of the doubler since the power for these diodes will be high, around 10 dBm. The result is shown in Figure 3.21.

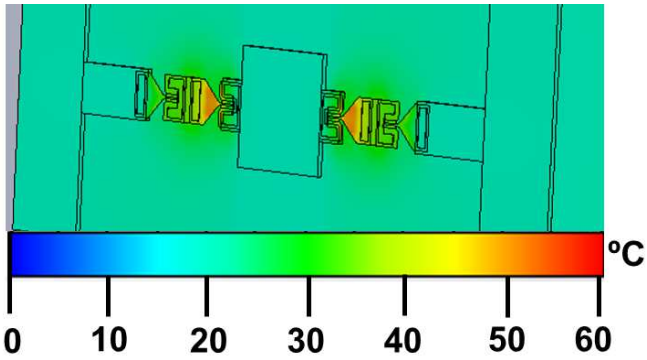

Figure 3.21: 3D illustration of the result of the thermal analysis of the frequency doubler.

As we can see, the maximum temperature is 60 °C. Therefore, it is safe for these diodes to work with this power level. However, it is important to notice that four diodes are used instead of two in order to manage the power [Jia17]. The analysis of the mixer antiparallel diode pair has not been carried out since the LO power is around 2 dBm for the best case and the diodes are not biased. Therefore, high temperatures will not be reached and no risk is foreseen.

3.4 Fabrication and measurements

The manufacturing process has been split into two phases. The fabrication of circuits on the substrate by means photolithography is realized at the Public University of Navarra (see Appendix A for details). Meanwhile, the metallic housing blocks are CNC machined in an external workshop. Finally, the Schottky diodes are fabricated by United Monolithic Semiconductor (UMS) foundry.

For characterization, the Y-Factor gain method was used [Tec14, Roh12, Rä80]. An schematic of the setup for Y-Factor characterization of the mixers is shown in Figure 3.22. The hot load is obtained placing a piece of WAVASORB material [Eme18] in front of the RF antenna. For the cold load measurement the RAM material is introduced in a container with liquid nitrogen and afterwards, placed in front of the RF antenna. Using the power difference the Y-Factor is calculated, thus, the DSB equivalent noise temperature of the receiver is obtained. The mixer equivalent noise temperature and conversion loss are afterwards obtained by removing the IF chain contribution.

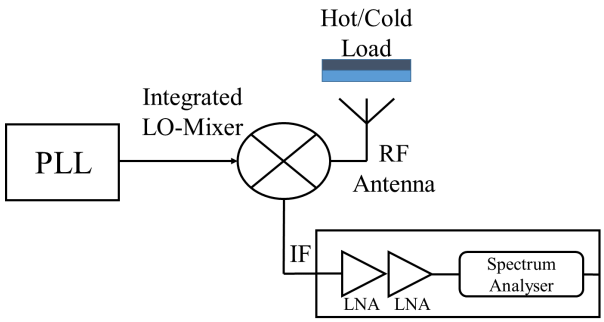

Figure 3.22: Schematic of the Y-Factor setup used for mixer characterization.

The IF chain consists of two LNA amplifiers (GAMP0100.0600SM10 [Neo19]) with 35 dB gain and 1.8 dB NF. Their output was connected directly to a Keysight N9030A spectrum analyzer, where the power at 2 GHz was measured. A 20 dBi standard gain horn antenna was connected to the RF port of the mixer and the Y-Factor technique was applied using liquid nitrogen and room temperature as cold and hot loads respectively [Mae14c].

3.4.1 Local Oscillator

The local oscillator is fabricated using photolithography on 670 μm thick Rogers 3210 ($\epsilon_r = 10.2$ and $\tan\delta = 0.0027$) and shaped with a LPKF H-100 milling machine. Afterwards, it has been mounted alone in a board in order to check that the output signal is stable. For this purpose, the control voltages of the MMICs are set by an Arduino Due [Ard19]. The local oscillator is connected to a phase lock loop to control the oscillation frequency. An image of the setup can be seen in Figure 3.23.

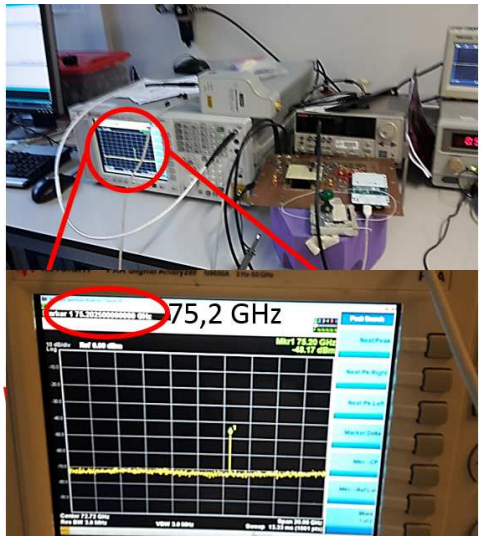

Figure 3.23: Photograph of the MMIC based local oscillator setup and zoom on the Spectrum Analyzer screen showing an example of its output.

3.4.2 Fourth harmonic mixer

The fourth harmonic mixer has been printed on Topas COC also using photolithography and copper metallization using e-Beam evaporator. The mixer is about 20 mm long, 340 μm wide and 100 μm thick. A picture can be seen in Figure 3.24.

For the assembly, firstly the Schottky diodes were shaped using a Disco Dicing Saw DAD321. Once they have been cut they are welded to the microstrip

Figure 3.24: Picture of the fourth harmonic mixer printed on Topas COC substrate.

circuit by means of silver epoxy (EPOTEK H20E). Silver epoxy and diodes placement were realized with a wire bonding and die placing machine (TPT HB16D). Afterwards, the diode I-V curve is measured and the substrates are placed in the housing metallic block. Finally, bonding with silver epoxy is done from the local oscillator Rogers substrate to the mixer substrate. A picture of the fourth harmonic mixer in the metallic housing block with an inset showing the UMS diodes in detail can be seen in Figure 3.25.

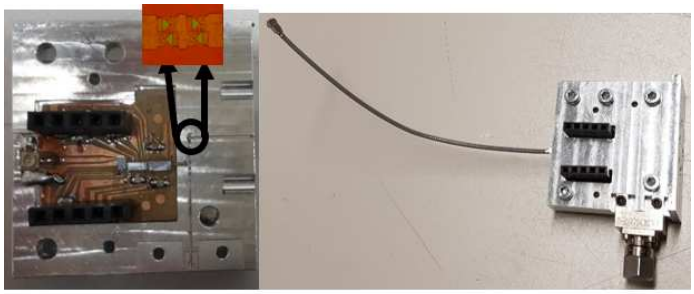

Figure 3.25: (a) Picture of the fourth harmonic mixer assembled on the metallic housing block bonded to the local oscillator. (b) Picture of the enclosed mixer block ready for measurement.

The characterization was carried out using the Y-Factor procedure and set-up above described. A picture of the real setup is shown in Figure 3.26.

The measured mixer results are shown in Figure 3.27, where the comparison between the measured and the simulated performance can be observed.

The performance of the fabricated mixer is plotted with a blue solid line. The measurement of the ENT has been done changing the LO frequency with the PLL from 74 GHz to 77 GHz and evaluating at a fixed 2 GHz IF frequency,

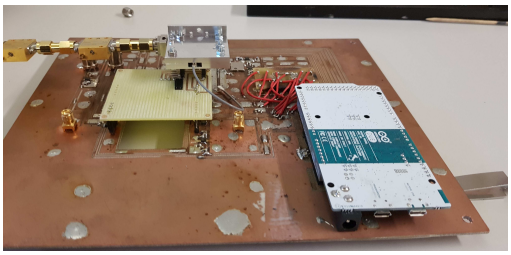

Figure 3.26: Y-Factor setup for fourth harmonic mixer characterization.

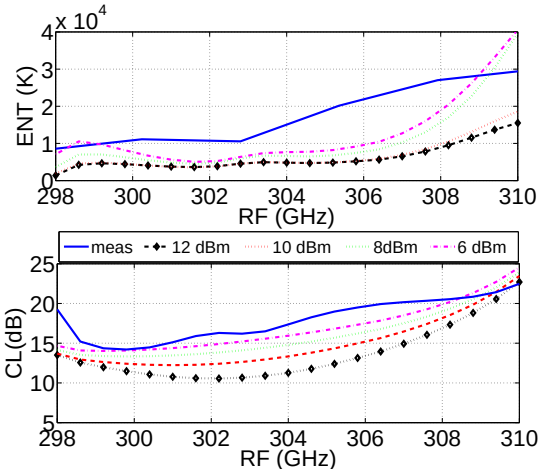

Figure 3.27: Comparison of the simulated and experimental performance of the fourth harmonic mixer for an Intermediate Frequency, IF = 2 GHz.

taking into account that the RF and the LO frequencies satisfy ($f_{RF} = 4 \times f_{LO} + f_{IF}$). The mean ENT is 18000 K and the conversion losses are 18 dB. There is a noticeable difference with respect to the best case of the simulated mixer, insomuch as the simulation is pretty stable and the ENT is about 7000 K. Observing the conversion loss, the behaviour of the fabricated mixer is similar to the case in which the LO power is about 6 dBm.

The mixer performance when sweeping the IF for a fixed LO frequency, in this case $f_{LO} = 75$ GHz, has also been measured. The predicted response compared with the characterized performance is shown in Figure 3.28.

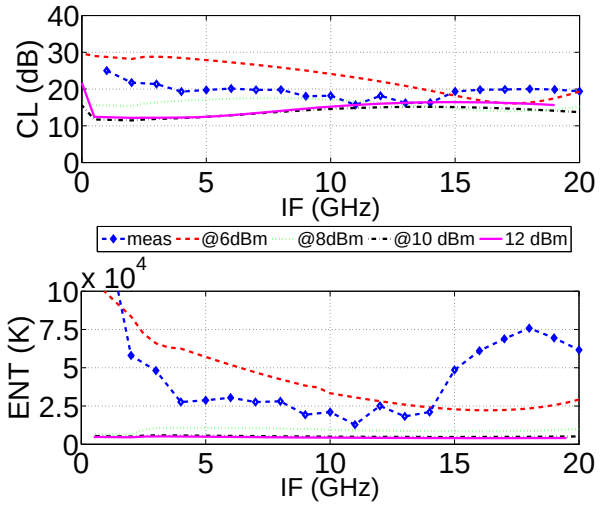

Figure 3.28: Comparison of the simulated and experimental performance of the fourth harmonic mixer for an Local Oscillator, LO = 75 GHz, sweeping the IF.

The evaluated performance of the fourth harmonic mixer is plotted with a blue dashed line with diamonds. The measurement has been done changing the IF and using a fixed 75 GHz LO frequency.

The mean measured ENT is 45000 K, although a more stable and better performance is obtained from 4 GHz to 14 GHz, mean value 25000 K. However the circuit has an increasing ENT from 14 GHz to 20 GHz and below 4 GHz. The mean conversion losses are 20 dB. There is a difference with respect to the case in which the LO power is 12 dBm, since the mean ENT is 4500 K and the CL is 15 dB. When the LO power is 6 dBm, the circuit presents mean ENT equal to 43000 K and the CL are 23 dB. In general the performance of the fabricated fourth harmonic mixer is more similar to that simulated with LO power about 6 dBm.

Since the LO power can neither be controlled nor monitored, the main reason for the worse performance is ascribed to the mixer being underpumped. In addition, the diodes are welded, which may introduce a non desired resistance, besides the small misalignment of assembly. Finally, the tolerance errors of fabrication can contribute to the additional losses. Nonetheless, despite of the increasing losses of the performance of the manufactured mixer, the results are

promising, since the circuit is completely integrated.

3.4.3 Combined doubler/subharmonic mixer

The manufacturing process includes photolithography for the circuits on Rogers 3210 and Topas substrates and CNC machining for the housing metallic block. Photographs of all mixer circuits printed on Topas are shown in Figure 3.29.

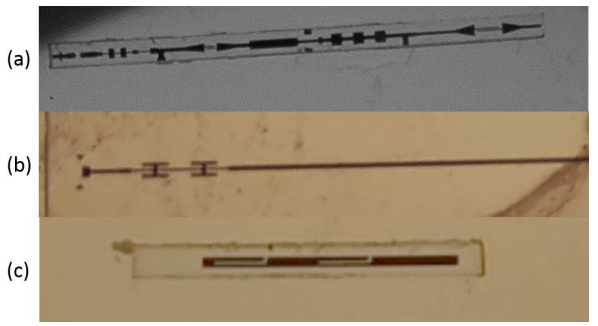

Figure 3.29: Pictures of the subharmonic mixer: (a) Subharmonic mixer printed on Topas COC without IF and LPF for DC bias filters. (b) Harmmerhead filter for IF and (c) LPF for DC Bias.

The assembly procedure is the same as that followed in the fourth harmonic mixer (3.4.2). A picture of the subharmonic mixer in the metallic housing block with inset showing the UMS diodes can be seen in Figure 3.30.

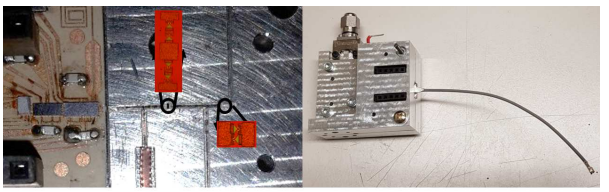

Figure 3.30: Photograph of the subharmonic mixer mounted in the metallic housing block: (a) MMIC source and doubler/subharmonic mixer with inset of the UMS diodes. (b) Enclosed housing metallic block.

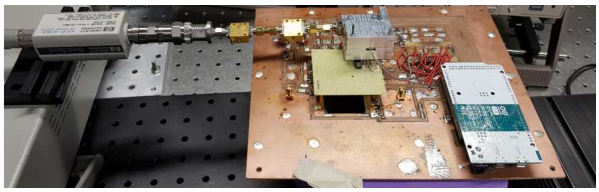

Figure 3.31: Setup for Y-Factor measurement where the board with Arduino Due for IN tuning can be observed.

Again the procedure to compute the evaluate Y-Factor is the same as for the fourth harmonic mixer. A picture of the characterization setup can be seen in Figure 3.31.

The values of conversion loss and equivalent noise temperature obtained by the Y-Factor measurement technique are compared with those predicted by simulation and shown in Figure 3.32(a) and 3.32(b), respectively.

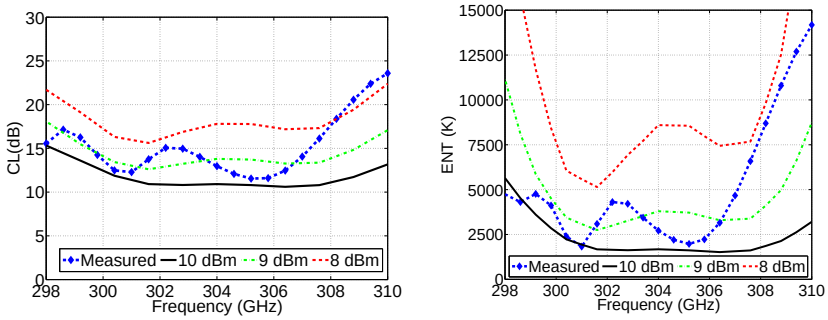

(a) (b)

Figure 3.32: (a) Measured conversion loss and (b) Measured equivalent noise temperature of the combined doubler/subharmonic mixer and its comparison with predicted performance for a fixed IF = 2 GHz.

The mean measured ENT is 4800 K, which, compared with the simulations, is around twice higher than the predicted performance. The minimum value is 1976 K, achieved at 305 GHz, and almost matches the simulated prediction. The same happens with the conversion losses, the measured mean value is 14 dB and

at 305 GHz we have the best measured conversion loss, which is 11 dB. These results are higher than the predicted response, where 10 dBm MMIC source (IN) power was considered. However, if lower IN power is considered, the response matches the measurement results. As a matter of fact, the measured response is in good agreement with the prediction for 9 dBm IN power, as shown in Figure 3.32(a) and 3.32(b).

The mixer performance when sweeping the IF for a fixed IN frequency has also been measured. The predicted response, compared with the characterized performance, is shown in Figure 3.33.

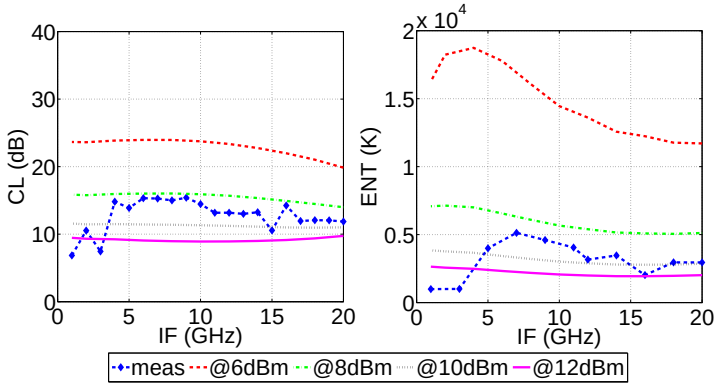

Figure 3.33: Comparison of the simulated and experimental performance of the combined doubler/harmonic mixer for a MMIC source frequency, $f_{IN} = 75.5$ GHz, sweeping the IF.

The mean measured ENT is 4000 K and the best performance, i.e. minimum noise is obtained at 1 GHz, whose value is 1200 K. The mean conversion losses are 13 dB. It can be appreciated that there is a little difference with respect to the case in which the IN power is 12 dBm, since the mean ENT is 2000 K and the CL is 9 dB. When the IN power is 10 dBm the circuit presents mean ENT equal to 3200 K and the CL are 11 dB. If the IN power is 8 dBm then the CL and ENT are 16 dB and 5600 K, respectively. In conclusion, the performance of the fabricated combined doubler/harmonic mixer seems to be more similar to that in which the MMIC source (IN) power is about 9 dBm.

This lower power can be explained by the additional losses in the manufactured circuit. In addition to this, the power generated by the MMIC source is not constant in the working frequency band.

3.5 Conclusions

Two different fourth harmonic mixers with integrated MMIC based source have been presented in this work. Firstly, a 300 GHz fourth harmonic and, secondly, a 300 GHz combined doubler/mixer were manufactured. The MMIC source acts as a LO for the fourth harmonic mixer and as a input signal for the doubler of the combined doubler/mixer, the output of the doubler is then used as LO for the mixer. This cost effective solution allows the use of low frequency MMIC sources based on COST components, which can be developed on planar technology. This allows having all the receiver packaged in the same metallic housing block.

The results show good performance, which is mainly limited by the MMIC source output power. The response of the combined doubler/subharmonic mixer is better, but at the expense of increasing the complexity of design and fabrication. Nonetheless, the presented results show the possibility of integration of a full THz receiver in the same single packaging metallic block, with the consequent reduction of mass and volume.

The behavior of the mixers is satisfactory and the results are not far from the the state-of-the-art. A comparison between this work and other published mixers working at similar frequencies is shown in Table 3.3.

Table 3.3: State-of-the-art of Schottky diode mixers working at similar frequencies to this work.

Ref	Frequency (GHz)	Harmonic	CL (dB)	ENT (K)
[Tho05]	2nd	300-360	6.5	1270
[Tho08a]	2nd	365-395	10	2500
[Rec15]	2nd	320-350	8	2000
[Guo18]	2nd	290-310	9-10	2000-2600
[Tho08b]	2nd	320-360	10-11	N.A
[Sob11b]	2nd	320-360	9	3000
[Li16]	4th	369-477	14	-
[Mae14a]	4th	430-460	14	10000
[Den18]	4th	320-500	18	-
Fourth mixer 3.4.2	4th	298-310	18	18000
Doubler/mixer 3.4.3	2nd	298-310	14	4000

Chapter 4

Optoelectronic Transmitter Based on UTC-PD source and Schottky Diodes Frequency Tripler

The use of photodiodes is a good solution for high frequency signal generation in high data rate communications. Besides, they are suitable to be implemented in wireless system [Sha17]. In order to achieve wider bandwidth, which implies the possibility of higher data rate, higher frequencies are required. To this aim, frequency multiplication of a lower frequency signal is a good solution.

In this work, Schottky diodes, which are the most common multiplying device [Mae10, Tho12, Rai92], are used for frequency multiplication of a submilimeter wave signal generated by a UniTravelling Carrier Photodiode (UTC-PD). There are other alternatives, such as Heterostructure Barrier Varactors (HBVs), which are very efficient and can manage high output power levels, but they present the disadvantage of being narrowband element [Kol89, Bry10]. Another solution could be to use an active multiplier, based on High Electron Mobility Transistors (HEMT), which, being active devices, feature good efficiency but present less stability than a passive multiplier[Mim05]. Reactive Schottky diodes, known as varactor diodes, are also a good solution for multiplication but they have the same narrow bandwidth problem as HBVs. Therefore, the best solution in our case is the use of varistor Schottky diodes that are able to per-

form wide bandwidth with good stability. However, their conversion efficiency is slightly lower than with the other devices.

In this section, an integrated transmitter will be presented, based on a balanced frequency tripler using varistor Schottky diodes. Figure 4.1(a) shows the overall block diagram of the proposed system. The input source is a UTC photodiode, pumped with two optical signals, which generate a signal in the W-Band. Therefore, the output signal of the final device will be around 300 GHz.

The frequency tripler uses a balanced configuration featuring an antiparallel pair of diodes. The main advantage that this design offers is the integration of the signal source and the tripler in the same substrate. This way a compact integrated transmitter is achieved. A perspective view of the circuit is shown in Figure 4.1 (b).

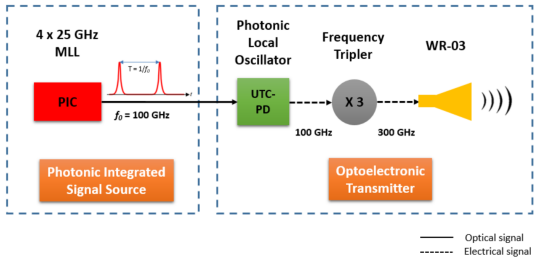

(a)

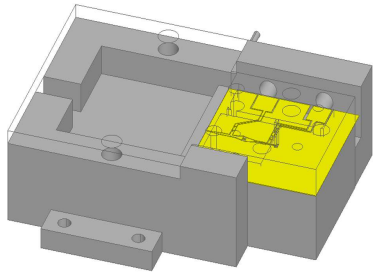

(b)

Figure 4.1: (a) Block diagram of the 300 GHz optoelectronic transmitter based on UTC-PD and Schottky diode technology. (b) 3D view of the whole transmitter. The top metallic block is shown with transparency in order to see the substrate and the bottom metallic part.

4.1 100 GHz source based on UTC-Photodiode

One of the key components in this proposed 300 GHz transmitter is a high speed UTC photodiode (UTC-PD). This type of photodiode has been dominant for generation of high power mm-Wave and sub-THz carrier signals using photonic techniques. Thanks to the separated absorption and carrier generation regions, the space-charge effect is reduced, what results in higher saturation power levels as compared with PIN photodiodes.

The UTC-PD used for this work was manufactured at III-V Lab [Rou12], with 50 Ω coplanar electrical output. They have an active area of 4 x 15 μm^2, and up to 1 mW output RF power at 120 GHz. The photodiode chip, fabricated on 120 μm thick indium phosphide (InP) substrate, was mounted on an aluminium nitride (AlN) subcarrier for improved heat dissipation.

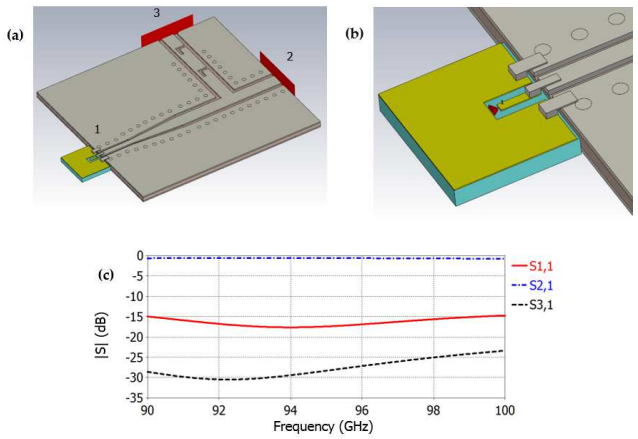

Figure 4.2: (a) 3D perspective view of the integrated UTC-PD to tripler passive circuit; (b) Close view of the UTC-PD 50 Ω coplanar structure excited by a discrete port providing the input signal; (c) Simulated frequency response.

The performance of the transition from the UTC-PD MMIC and the coplanar input of the tripler has been studied with Ansys HFSS. This includes the circuit to allow DC biasing of the PD. Figure 4.2(a) shows the full-wave electromagnetic model of the UTC-PD integrated with the input section of the tripler passive circuit.

The RF coupling between the PD and the PCB is addressed by using silver-filled epoxy, which avoids the inductance of the bond wires when wire bonding is used. The UTC-PD chip is modelled as a 5 μm thick coplanar waveguide (CPW) on InP with 50 Ω impedance, as shown in Figure 4.2(b). To achieve closest approximation, the conductive epoxy is realized as slabs of silver.

The simulated response is shown in Figure 4.2(c). It can be noticed that the overall insertion loss (S_{21}) between the input (UTC-PD) and the passive circuit stays lower than 1 dB in the complete input signal frequency range (90 – 100 GHz). The isolation (S_{31}) between input port and DC port is better than 23 dB.

4.2 UMS Schottky Diode

A 3D perspective view of the antiparallel diode configuration is shown in Figure 4.3.

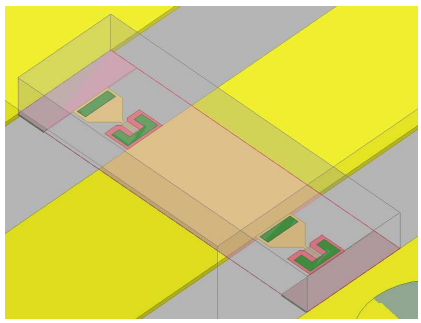

Figure 4.3: Perspective view of the balance configuration of Schottky diodes.

The flip-chip is about $200\mu m \times 80\ \mu m$. We use a balanced configuration featuring the equivalent to an antiparallel pair of Schottky diodes, i.e. the Schottky diodes are in series regarding to the DC bias but in antiparallel with respect to the RF. This configuration (details in Section 1.2.3) works only with odd harmonics and suppresses the even harmonics, which implies a more efficient design for tripler configurations. In our case we are interested in the third harmonic and we reject the other ones.

4.3 Design procedure

The frequency tripler is designed around an antiparallel configuration of Schottky diodes. This flip-chip is over 130 μm thick Rogers RT/Duroid 5880 dielectric substrate ($\epsilon = 2.2$ and $\tan\delta = 0.009$). Grounded coplanar waveguide is printed on this substrate. It also makes use of vias to assure electric contact between coplanar and bottom grounds, which improves the behaviour of the transmission line. A scheme of the whole circuit is shown in Figure 4.4.

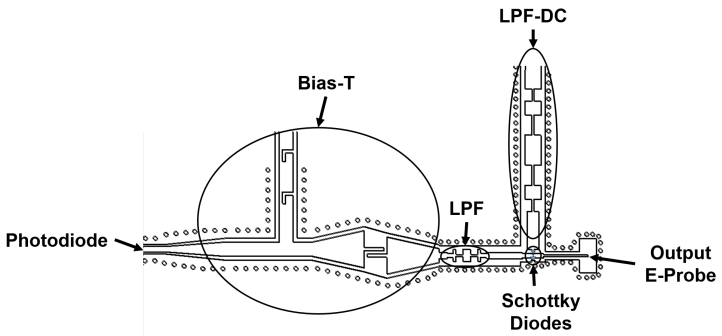

Figure 4.4: Scheme of the integrated photodiode and Schottky diode frequency tripler.

As it has been already said, the input source (IN) is a photodiode whose signal has a frequency range between 90-100 GHz and around 0 dBm output power. The photodiode is fed by an optical fiber and a Bias-T is also necessary to bias it. The Bias-T consists of a low-pass filter for the DC and a DC-Block that reject the DC and allow to pass only the high frequency signal. After the DC-Block of the Bias-T, a low-pass filter is used. This filter has been designed based on a stepped impedance configuration because of the simplicity of its design with a narrow fullprint. The goal of this filter is to reject the output of the diodes so that they go only to the output E-Probe. This probe not only excites the WR-3 waveguide but also acts as a high pass filter, since the photodiode signal is below the cutoff frequency of the waveguide. The Schottky diodes are biased, as it was commented; therefore, a low pass filter is necessary to block the RF and IN signals.

4.3.1 Passive circuit designs

The four circuits that are necessary for the implementation of the transmitter are discussed bellow. Their 3D-views and predicted responses using full wave simulator HFSS are shown in Figure 4.5.

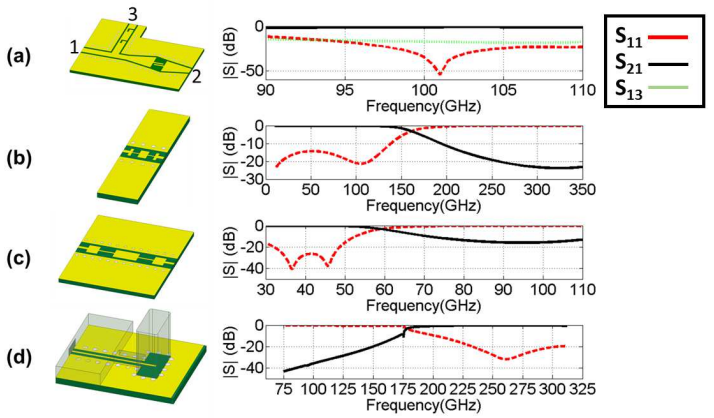

Figure 4.5: Passive circuits: perspective view and simulations. (a) Bias-T, (b) LPF for IN signal, (c) LPF for DC bias and (d) Waveguide transition.

Bias-T The Bias-T, Figure 4.5(a), is used to bias the photodiode with a DC voltage. Therefore it is important to notice the low insertion losses of the DC-Block, whose mean value is 1.3 dB, and the high rejection of the low pass filter. The DC port is isolated by 17.21 dB from the W-Band signal of the photodiode.

Low pass filter for IN signal This filter has a rejection for the RF signal of 23.3 dB at 300 GHz and the insertion loss for input frequency is very low, 0.13 dB at 100 GHz. The cutoff frequency is 160 GHz, as shown in Figure 4.5(b).

Low pass filter for DC bias Figure 4.5(c) shows the LPF for DC bias, which presents 59 GHz cut-off frequency. This filter lets the DC voltage pump the diodes and blocks both source signal and RF signals. Besides, the rejection of these signals with this filter improves the conversion loss of the frequency tripler. The rejection is 15 dB at 100 GHz.

Waveguide transition The waveguide transition, Figure 4.5(d), acts as a high pass filter for all signals except the RF, insomuch as the cutoff frequency of the waveguide is 178 GHz. The insertion loss for the RF is less than 0.5 dB in the whole band and the return loss is below 20 dB.

These components are connected by coplanar lines, whose length is optimized taking into account the nonlinear analysis of the multpiplier.

4.3.2 Non-linear analysis

For the load-pull analysis of the balanced configuration, see Figure 4.6, the impedances at input (IN) and at output (RF) frequencies have been calculated. The best performance of the tripler is obtained with diode embedding impedance $Z_{RF} = 46.75 - j73\ \Omega$ and $Z_{IN} = 124 + j76\ \Omega$ for RF and IN frequency, respectively.

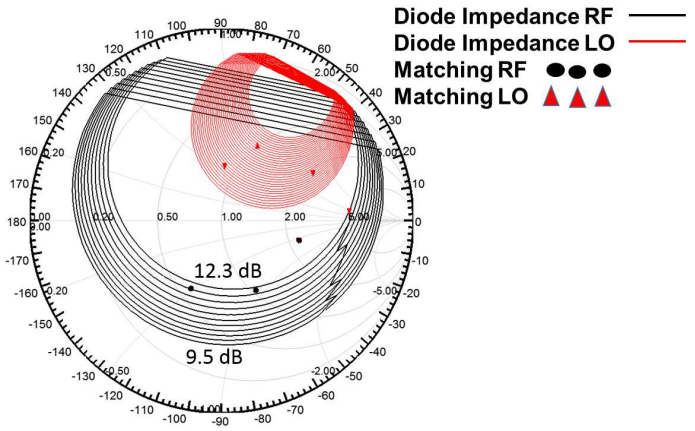

Figure 4.6: Load-Pull analysis results and matching procedure for the balanced configuration performing antiparallel pair of Schottky diodes.

The full 3D model used for the simulation can be seen in Figure 4.7.

We are considering a coplanar waveguide with vias which is covered with a standard metallic lid. The height of the lid is chosen to be 400 μm, since this height does not disturb the fields. This circuit is simulated using the finite element method of the software package Ansys HFSS.

Once it has been simulated, the S-parameters of this circuit are exported and

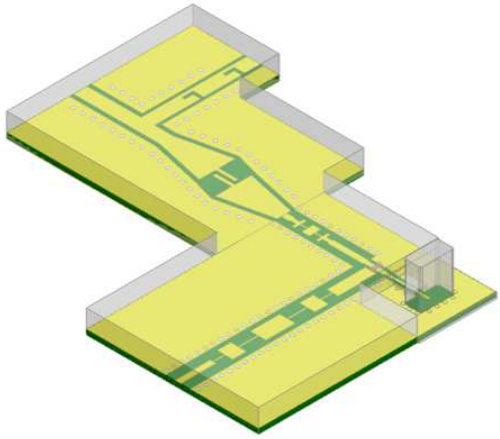

Figure 4.7: 3D perspective of the transmitter model used for simulation.

used in the harmonic balance simulation of ADS. The predicted performance is shown in Figure 4.8.

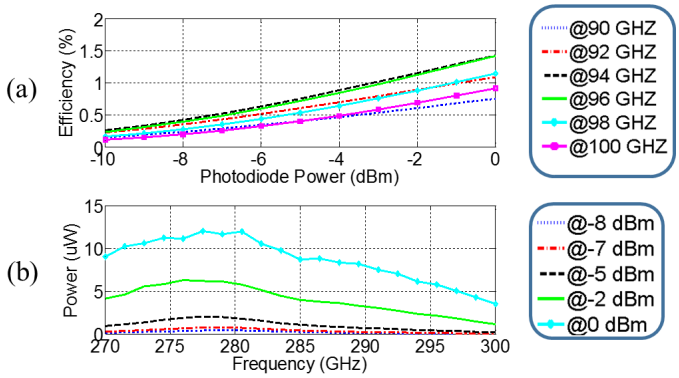

Figure 4.8: Performance of the photodiode fed frequency tripler. a) Efficiency and b) output power.

In Figure 4.8(a) we can observe the efficiency of the frequency tripler and in Figure 4.8(b) the output power. The performance has been analysed for

different values of photodiode power in order to evaluate the degradation of the behaviour when the input power is too low, i.e., the limit of operation. For the range of input powers analysed, the efficiency of the tripler increase when the input power to the multiplier also increases. The performance of the tripler is therefore limited by the output power level of the photodiode. This could be improved if a W-band amplifier were used to increase the power level.

The analysis has also been carried out for different frequencies, in order to determine the bandwidth of the frequency tripler and the output power of the system. The efficiency is rather stable in frequency for all input power levels; in any case, for 0 dBm we obtain the best case. The efficiency is around 0.7 to 1.3 % for the whole bandwidth. For -5 dBm we obtain that the efficiency goes from 0.5 to 0.8 % and in the worst case, for -10 dBm input power, it performs around 0.1 %. The output power is, therefore, around 8.5 μW for the whole bandwidth for an input power of 0 dBm, whereas for -5 dBm the power is around 1 μW.

4.3.3 Thermal analysis

The performance of the Schottky diodes may be degraded with the temperature as has been already explained in previous sections. For this reason a thermal analysis is realized in this section. Even though in this case the power of the photodiode that reaches the Schottky diodes is not very high, the diodes are biased and this DC current increases the temperature.

The predicted temperature obtained with the mechanical and thermal module of the commercial software CST is shown in Figure 4.9. As we can observe, the temperature in this case is 74 °C which is within the safety working range.

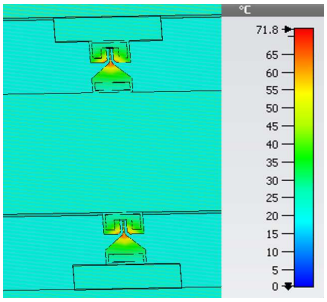

Figure 4.9: Thermal analysis of the multiplier Schottky diodes.

4.4 Conclusions

In this chapter we have presented a transmitter working in the THz frequency band for high speed wireless communications. The device has been realized integrating an UTC photodiode and a frequency tripler based on Schottky diodes. The main advantage of this device is the high integration level, since it combines both chips, i.e. photodiode and Schottky diodes, on the same substrate and packages them in the same housing metallic block.

The feasibility of this prototype has been demonstrated by simulations, as measurements is still pending. The output power we can achieve at 300 GHz is about 12 μW in the best case. This low output power is limited by the low power level generated in the photodiode and could be compensated using a LNA at W-Band in order to obtain a higher input power to the frequency tripler, with the consequence of higher output power at 300 GHz. Nonetheless, it is a good demonstration of integration, which could be of interest for future THz wireless links.

Chapter 5

Integrated mixer-multiplier based on GaAs membrane Schottky diodes

During the last years, the interest in terahertz and submillimetre wave receivers has increased due to the high possibilities for ultrafast communications, space and atmospheric observation, applications in security imaging, etc. The receiver described in this chapter performs at 600 GHz. This frequency is of interest for observation of meteorological phenomena.

However, the design of receivers at this frequency faces difficulties associated with the local oscillator (LO). A standard subharmonic mixer would require a 300 GHz LO. This can be obtained from a lower frequency signal by frequency multiplication. If this last component is individually designed and assembled a bulky solution is obtained,which is prone to problems due to misalignments and losses in the flange interfaces. Therefore, integration of the frequency multiplier and the mixer would be a more efficient solution, with advantages in terms of performance, size and mass.

In this case, due to the high frequency, an integration solution based on discrete diodes would not be possible. Therefore, a solution based on integrated GaAs membrane Schottky diodes is proposed.

5.1 Design methodology

The literature about the development of frequency multipliers and mixer is very extensive, see [Meh17] for a review. The concepts about the designs of these kind of circuits have been used in this work. In addition, new concepts have been taken into account, such as the interaction between both circuits, the mixer and the frequency multiplier.

5.1.1 GaAs membrane Schottky diode technology

The main advantage of GaAs membrane technology resides in the fact that these diodes are integrated with the substrate. This monolithic integrated circuits (MICs) avoid the problems associated to the manual assembly of discrete diodes. Besides, for high frequencies, the use of discrete diodes is limited by the performance of the supporting substrate, which must be thin enough. However, the use of a thin membrane allows the use of integrated diodes up to several terahertz [Zha12, JK09, Tho10b, Bul16]. For the diodes on membrane we begin with a six layer structure [Dra13]. These layers as described in Table. 5.1.

Table 5.1: Layers of GaAs membrane Schottky diodes.

No.	Layer	Material	Thickness [nm]	Doping[cm^{-3}]
5	Active	GaAs	64	3×10^{17}
4	Contact	GaAs	1500	$> 10^{19}$
3	Top Etch Stop	$Al_{0.55}Ga_{0.45}As$	60	Undoped
2	Membrane	GaAs	3000	Undoped
1	Bottom Etch Stop	$Al_{0.75}Ga_{0.25}As$	400	Undoped
0	Substrate	GaAs	•	Semi-insulated

Then, patterning of the ohmic contacts is realized. Afterwards, the Schottky contacts, the air bridge and membrane shape, and finally the passive circuitry, i.e., beam leads, filters and waveguide probes are created.

In this case, we aim at designing a subharmonic mixer integrated with a frequency tripler for the local oscillator, equivalent to the behaviour of a sixth harmonic mixer from the frequency conversion point of view. Therefore, the antiparallel configuration is used in order to avoid even harmonics and achieve the best performance for the tripler and subharmonic mixer. An image of the antiparallel Schottky diode pair can be seen in Figure 5.1.

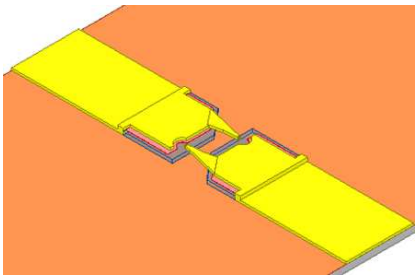

Figure 5.1: Antiparallel configuration of Schottky diodes.

The area of the anode depends on the frequency band in which they are intended to work. The anode size for the mixer working at 600 GHz is 0.7 μm^2, the series resistance is 19 Ω, saturation current, I_s, is 1.3 fA, junction capacitance, C_j, is 1.4 fF and ideality factor $n = 1.2$. The tripler works from 100 GHz to 300 GHz. It has an anode size of 1.2 μm^2 with the following parameters: series resistance is 10 Ω, saturation current, I_s, is 1.9 fA, junction capacitance C_j is 24 fF and ideality factor $n = 1.18$.

5.1.2 Topology

An schematic version of the whole structure is shown in Figure 5.2. It can be seen that, besides the diodes, some filters and waveguide probes are needed to get the desired mixer behaviour.

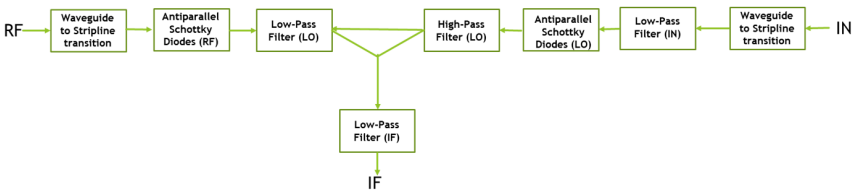

Figure 5.2: Schematic of the integrated tripler-mixer.

The waveguide probes are necessary to couple the E-field in the rectangular waveguide to the membrane stripline. Then we need the low-pass filter for the mixer, in order to avoid the signal higher than 500 GHz going through the IF bend or the tripler circuit. The low-pass filter for IF is used to isolate this

circuit from the local oscillator, i.e. the output of the frequency tripler, and radiofrequency signal.

The tripler circuit has two filters. The first one is a low-pass filter at 100 GHz to isolate the input waveguide from the 300 GHz signal generated after the multiplication.The second one is a high-pass filter used to prevent the 100 GHz signal from the IN signal to couple to the mixer, since only the 300 GHz LO signal, i.e. the output of the tripler, is allowed to go through this filter. Finally, some matching lines are needed to match the diodes to the rest of the circuit.

5.2 Passive circuits design

The passive circuitry is going to be described and analysed in this section. As it has been said before, it consists of waveguide probes, filters and matching lines. All these components are realized in stripline technology, using a 3 μm thick GaAs membrane with the following parameters: $\epsilon_r = 12.6$ and $tan\delta = 0.0004$. This substrate is enclosed in a 340 μm $\times$ 150 μm waveguide channel. A top view of all passive circuits and simulations results can be seen in Figure 5.3.

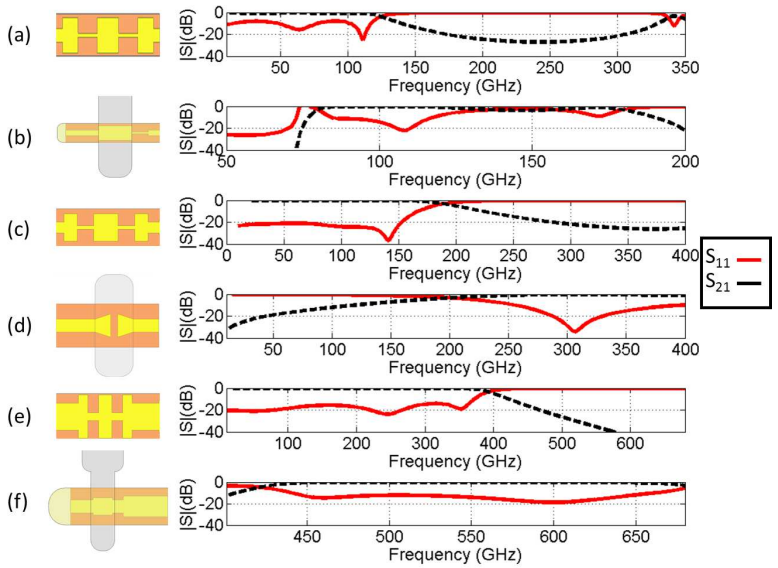

Figure 5.3: Top view and predicted response of the passive components of the sixth harmonic mixer. (a) Stepped impedance LPF for IF; (b) Waveguide transition for IN; (c) LPF for IN; (d) High pass filter for LO; (e) LPF for LO; and (f) waveguide transition for RF.

5.2.1 Filters

The filters are necessary to avoid undesired effects provoked by frequencies out of the region of interest, caused by spurious harmonics. In this case, the low-pass filters have been designed using the stepped impedance configuration. This one is the most common topology for low-pass filters due to the easy implementation and good performance even with a reduced number of steps. Every passive component has been designed and simulated using Ansys HFSS (High Frequency Structure Simulator) 2017.

Figure 5.3(a) is a low-pass filter that let pass only the intermediate frequency and reject all frequencies higher than 50 GHz. The cutoff frequency of the filter is 100 GHz, so that the intermediate frequency will pass and higher frequency will be attenuated or rejected to isolate the IF output from the non-desired higher frequency signals.

The next step consists in the design of a low-pass filter to let the input signal pass to the diodes and reject the output of the tripler (LO) in order to avoid this signal going to the input waveguide. This filter can be seen in Figure 5.3(c). The cutoff frequency of the filter is about 200 GHz and it is well matched around 100 GHz. For the output signal of the tripler, i.e. 300 GHz, the rejection is quite high, about 22 dB. This way, the LO signal will not go to the input source.

A high-pass filter is also necessary in order to avoid the input signal at 100 GHz to reach the mixer, and can be seen in Figure 5.3(d). The insertion loss is 12 dB for IN frequency and the return loss is 0.5 dB, whereas the pass-band for the LO frequency has 0.12 dB insertion loss and 20 dB return loss.

Finally, the last filter required is a low-pass filter and can be observed in Figure 5.3(e). The cutoff frequency is 396 GHz, therefore the local oscillator at 300 GHz can go through the filter as well as the intermediate frequency, but the higher frequency, related to the radiofrequency signal, is rejected. The insertion loss for RF (580-680 GHz) is higher than 40 dB.

5.2.2 Waveguide probes

Stripline to waveguide transitions are necessary to characterize this planar circuit with waveguide measurement equipment. Besides, this kind of transitions are also necessary in order to integrate it with waveguide based components, such as horn antennas. In this work the most usual transition has been implemented, the E-probe, which is realized by introducing a microstrip line through an aperture in the E-plane of a rectangular waveguide. This way the quasi-TEM mode of the microstrip line couples to the TE_{10} mode of the rectangular

waveguide.

The microstrip to WR10 waveguide transition for the input source can be seen in Figure 5.3(b). We can observe the behaviour of the transition: the S_{11} is below -15 dB from 100 GHz to 115 GHz. In principle, the frequency tone for our input is 105 GHz so the transition fits this frequency. Besides, the insertion loss is about 0.5 dB.

The waveguide probe for the RF input can be seen in Figure 5.3(f). The input waveguide in this case is WR1.5. The return loss for the radio frequency signal (580-650 GHz) is better 15 dB and the insertion losses are lower than 0.5 dB.

5.3 Non-linear analysis

Once the passive circuitry has been designed and simulated, the non-linear behaviour can be analysed. To this end, Keysight's Advanced Design System (ADS) has been used. The first step consists in the analysis of the performance of the Schottky diodes acting as a mixer and tripler by means of the load-pull technique, so that the optimum values of embedding impedance can be determined. The second one is the simulation of the whole circuit and the calculation of the matching lines needed to obtain the more similar behaviour to the ideal one.

5.3.1 Load-pull technique

The load-pull technique is applied for matching and shown in Figure 5.4.

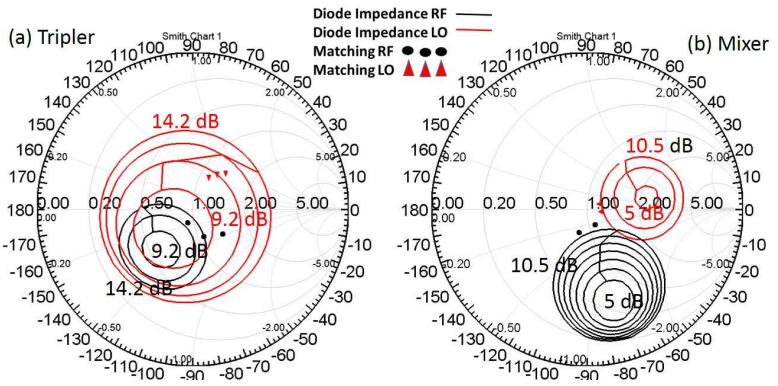

Figure 5.4: Load-pull analysis results. (a) Tripler: Red solid line corresponds to the diode embedding impedance at IN frequency and black solid line at LO frequency. (b) Mixer: Red solid line corresponds to the diode embedding impedance at LO frequency and black solid line to RF. The dots correspond to the obtained values of embedding impedance.

Figure 5.4 represents the load-pull analysis results in the Smith chart. We can see the circles for which the conversion losses are constant. In this case, the mixer has a minimum of CL equal to 5 dB. In order to achieve this optimum performance, for the frequency tripler we obtain that the diode embedding impedance is $Z_{IN} = 85.4 + j32.7\Omega$ and $Z_{LO} = 57.4 - j23.7\Omega$ for IN and LO,

respectively. For the mixer case, the minimum conversion losses are obtained for diode embedding impedance $Z_{LO} = 25.49 + j12.23\Omega$ and $Z_{RF} = 30.6 - j60.13\Omega$ for LO and RF, respectively. It is important to notice that the bigger the circle the higher the losses, that is, the bandwidth is narrower for lower conversion loss. Therefore, a trade-off between both parameters must be established.

5.3.2 Simulation of mixer behaviour

The matching lines in between the filters were optimized to obtain the required embedding impedance. The obtained values are indicated with dots in Figure 5.4. Using these values, the full model of the integrated tripler/mixer was constructed. A perspective view of the 3D model used for the simulation and evaluation of the integrated sixth harmonic mixer is shown in Figure 5.5.

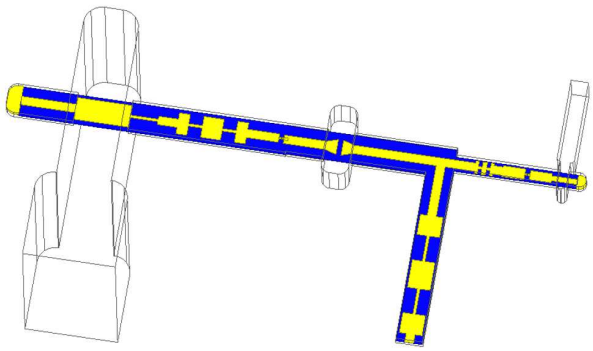

Figure 5.5: 3D view of the integrated tripler/mixer used for simulation.

As it has been already described in this thesis, firstly the linear behaviour of the whole structure is simulated using commercial software HFSS. Once the S-parameters are obtained, they are exported and used for the non-linear analysis in ADS. In this circuit we have an input signal at 106 GHz, whose power will be swept from 10 mW to 30 mW in order to determine the point for which the tripler generates enough power to pump the mixer diodes and the stability for different input power. The other input is the radiofrequency signal which is set to be -30 dBm from 600 to 660 GHz. The IF frequency is swept according to the RF taking into account that $f_{IF} = f_{RF} - 2 \times f_{LO} = f_{RF} - 6 \times f_{IN}$. We do not have any bias voltage, since both configurations are antiparallel.

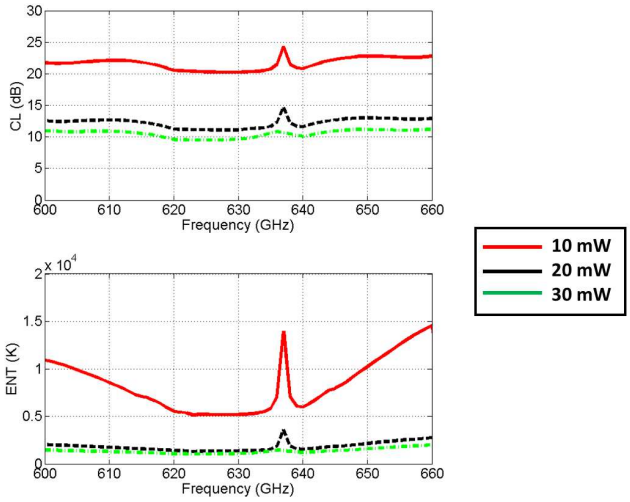

Figure 5.6: Conversion Loss and Equivalent Noise Temperature for different levels of input power.

We can see the estimated conversion loss (CL) and equivalent noise temperature (ENT) in Figure 5.6. It is observed that the conversion loss is very stable in both frequency and power. However, we need power higher than 10 mW at 100 GHz, since the output power of the tripler is not enough to pump the mixer diodes. The best conversion loss is around 10 dB for 30 mW. This is a good result, close to the state-of-the-art at these frequencies and with the advantage that comes from having the frequency tripler integrated. The ENT is around 1500 K, which is agreement with the state of the art in this frequency range.

5.4 Thermal Analysis

In previous chapters the thermal analysis has been realized for UMS Schottky diodes and the importance of such analysis has been commented. In this case, the specifications are different since the diode fabrication technology is different. The maximum temperature allowed for a normal behaviour is 180 °C. The diodes could support more temperature but they would not endure much time. Therefore, it is important to work below this temperature.

A thermal analysis of the Schottky diodes used for tripler frequency multipler is shown in Figure 5.7. The thermal analysis of the mixer diodes is not realized because the input power will be the output power of the tripler, which is low enough to be safe.

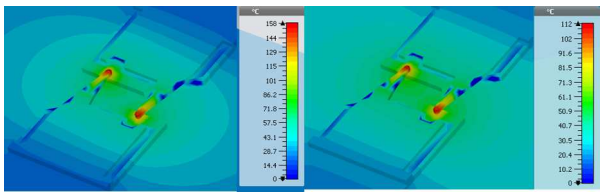

Figure 5.7: Thermal analysis of the Schottky diodes for: (a) 30 mW and (b) 20mW.

As it can be observed, the temperature is almost at the limit for an input power of 30 mW, reaching a temperature about 150 ° C. However for 20 mW the diodes are working in the safety region and the conversion loss and ENT are good enough, therefore we can conclude the performance of the diodes is safe.

5.5 Conclusions

In this chapter a mixer based on Schottky diodes GaAs membrane technology has been presented. The prototype is a sixth harmonic configuration mixer performing like a subharmonic one thanks to the integration of a frequency tripler based on Schottky diodes in the same substrate as the mixer. The mean predicted conversion loss are 10 dB and the ENT is around 1500 K. The main advantage of this design consists in its simple integration. This is of great interest e.g. in space aplications, given the reduction of volume and cost that implies. Also the fact that the combined tripler/mixer is built on the same substrate is very convenient to avoid misalignments, which become more limiting when frequency increases.

The prototype fabrication is still pending.

Chapter 6

Conclusions and future work

This final chapter summarises the main results that have been obtained in this Thesis. Furthermore, some guidelines for future research are provided.

6.1 Conclusions

In this dissertation, different configurations for integrated sub-mm wave and terahertz components have been explored. First, a design method for transitions has been developed and applied to several waveguide technologies. In addition, several contributions to the design of integrated sub-mm receivers and transmitters based on Schottky diodes have been made. In particular, the main conclusions of this thesis are the following:

- A theoretical method for the calculation of the transitions dimensions without optimization, based on the small reflections and Chebyshev transformer theories has been presented. Four inline transition from planar to waveguide technology have been developed based on this theoretical method.

  - The first prototype consists of a microstrip line with a taper and a Chebyshev transformer in waveguide technology. Although the transition presents a good performance, it requires a H-plane cut in the waveguide that needs a very good contact between top and bottom parts, making its assembly a bit cumbersome.
  - The second transition we have developed in this work is similar to the previous one, also based on the combination of a Chebyshev transformer and a microstrip linear taper. However, instead of using standard waveguide technology we have used Groove Gap Waveguide technology, which solves the problems caused by the H-plane cut.
  - The third one, also based on GGW technology, presents an additional improvement for assembly, making it even easier than the one presented in second prototype. The substrate does not require any shaping insomuch as it covers the whole bottom metallic block. Thus, the assembly is easier and misalignments are avoided. However, all GGW sections are either partially or totally filled with dielectric. Therefore, it is necessary to make a combination of ridge and groove gap technology in order to avoid high order mode propagation.
  - Finally, the last transition is a further improvement of the third one. In this case, we have also combined ridge and groove gap technology. However, the substrate does not cover the whole bottom metallic block and does not fill any waveguide step, avoiding the possibility

of high order mode propagation. Besides, there is not any intermediate impedance, therefore the design procedure using Chebyshev transformer is simplified, since it is not split into two different steps.

- We have shown the feasibility of integrating a compact terahertz receiver with an integrated MMIC based Local Oscillator (LO) in a single enclosing metallic block. Two different designs have been studied:

  – Firstly, a subharmonic mixer combined with a frequency doubler so that, in terms of frequency conversion, it has the behaviour of a fourth harmonic mixer. It has been characterized and, although limited by the available LO power, its performance is close to the state of the art.

  – A further improvement in terms of integration can be obtained if a fourth harmonic mixer configuration is used. However, this configuration has been found to be more dependent on the available LO power.

  Both configurations demonstrate a cost effective solution for integrated THz receivers.

- An new scheme of integrated optoelectronic transmitter has been designed. The UTC-PD source is integrated along with a Schottky diode tripler so that the combination of both chips provides a good solution for THz wireless links for communications. The amount of power that the prototype provides is not very high and should be improved by the use of amplifiers. However, the integration concept could be a good starting point for future THz transmitters based on photonic sources.

- Finally, a combined tripler/mixer device based on GaAs membrane technology is proposed. In this design we have increased the frequency to work at 600 GHz. In order to develop a receiver at this frequency, the use of discrete welded Schottky diodes must be discarded. That is why GaAs membrane technology is a good solution, since the diodes are integrated to the substrate during the fabrication process and the thickness is only 3 μm, so that the losses ascribed to the substrate are reduced. The main advantage of this device is that it performs like a subharmonic mixer with a sixth harmonic configuration. This allows to work with a low frequency local oscillator with high enough power to pump the diodes.

6.2 Conclusiones

En este trabajo se han explorado diferentes configuraciones de componentes integrados en la banda de terahercios y ondas submilimétricas. Primero, se ha desarrolado un método de diseño para transiciones y ha sido aplicado en diferentes tecnologías guía de onda. Además, se han implementado y estudiado diversas contribuciones al diseño de receptores y transmisores basados en diodos Schottky funcionando en el rango de terahercios. En particular, las principales conclusiones de esta tesis son las siguientes:

- *Se ha presentado un método teórico para el cálculo de las dimensiones de las transiciones sin necesidad de optimización basado en la teoría de pequeñas reflexiones y el transformador de Chebyshev. De acuerdo con este método teórico se han presentado cuatro transiciones en línea de tecnología planar a guía de onda.*

  - *El primer prototipo que se ha presentado consiste de una línea microstrip con un taper y un transformador Chebyshev en guía de onda. Aunque la transición presenta un buen funcionamiento, tiene el corte en el plano-H y eso requiere asegurar un buen contacto entre las partes superior e inferior de la caja metálica, haciendo tanto la fabricación como el ensamblado tareas difíciles.*
  - *La segunda transición desarrollada en este trabajo es muy similar al diseño anterior, basado en el transformador Chebyshev y un taper microstrip. Sin embargo hemos usado tecnología groove gap waveguide en vez de guía de onda estándar. Por lo tanto, el corte en el plano-H ya no es un problema.*
  - *El tercer diseño, también basado en tecnología GGW, presenta una mejora en cuanto al ensamblado haciéndolo incluso más fácil que en el segundo diseño. El substrato no requiere ningún corte de forma específica ya que cubre por completo la superficie de la caja inferior, haciendo más fácil el ensamblado y evitando desalineamientos. Sin embargo, todas las guías del adaptador de impedancia están parcial o totalmente rellenas de dieléctrico, por lo que para evitar propagación de modos de orden superior hay que hacer uso de una combinación de las tecnologías ridge y groove gap waveguide.*
  - *Finalmente, la última transición que se presenta es muy similar a la anterior. En este caso también hacemos uso de las tecnologías*

ridge y groove gap waveguide; sin embargo, el substrato no cubre la totalidad de la superficie de la caja inferior y tampoco rellena ni total ni parcialmente ningún paso del transformador Chebyshev, evitando la posibilidad de propagación de modos de orden superior. Además, no hay ninguna impedancia intermedia, por lo tanto el diseño del transformador Chebyshev se simplifica al no tener que dividirlo en dos pasos.

- *Se ha mostrado la posibilidad de integrar un receptor compacto en terahercio junto con un oscilador local integrado basado en MMIC en un solo bloque metálico. Se han implementado dos diseños diferentes:*
  - *Primero, un mezclado subarmónico combinado con un doblador de frecuencia de tal forma que, en términos de frecuencia, el comportamiento es el de un cuarto armónico. El dispositivo ha sido caracterizado y aunque limitado por la potencia que ofrece el oscilador local, su rendimiento es cercano al estado del arte.*
  - *Una mejora adicional en términos de ingración se puede obtener si se usa la configuración cuarto armónico. Sin embargo, esta configuración resulta ser más dependiente de la potencia disponible por el oscilador local.*

  Ambas configuraciones han demostrado ser una solución económica para el desarrollo de receptores integrados en la banda de terahercios.

- *Se ha propuesto un nuevo diseño de transmisor optoelectrónico integrado. La fuente UTC-PD se integra con el triplicador basado en diodo Schottky de tal forma que la combinación de ambos chips proporciona una buena solución para los enlaces de comunicaciones en THz. La cantidad de potencia que el prototipo proporciona no es muy alta y debería ser mejorada con el uso de amplificadores. Sin embargo, el concepto es realmente interesante desde el punto de vista de integración y podría ser un buen punto de partida para futuros transmisores de THz basados en fuentes fotónicas.*

- *Por último, se propone un dispositivo combinado mezclador/triplicador basado en la tecnología de membrana de Arseniuro de Galio. En este diseño se ha incrementado la frecuencia de trabajo hasta 600 GHz. Con el fin de desarrollar un receptor a esta frecuencia debemos descartar la idea de trabajar con diodos discretos y soldarlos, con el fin de evitar desalineamientos e incrementos de su resistencia. De modo que la idea de*

trabajar con arseniuro de galio es una buena solución, ya que los diodos están integrados al substrato desde el momento de la fabricación y al ser el grosor de la membrana de 3 μm, las pérdidas asociadas a él son mínimas. La principal ventaja de este dispositivo además, es el hecho de que su comportamiento es similar al de un mezclador subarmónico mientras su configuración es la de un sexto armónico. Esto permite trabajar con osciladores locales de más baja frecuencia con mucha más potencia.

6.3 Guidelines for future investigation

There are some points that may be key for the improvement of the devices performance presented in this Thesis.

- The application of the packaging techniques explained in Chapter 2 to the harmonic mixer development; this way it could be possible to avoid the use of the air channel, which simplifies assembly and substrate shaping and enhances the behaviour of the planar to waveguide transition.
- Further increase the integration level by building the local oscillator and harmonic mixer in the same substrate thanks to the commercial availability of mm-Wave planar technology devices.
- Integration of a W-Band LNA amplifier at the output of the photodiodes in order to obtain a higher amount of power at the input of the Schottky diodes of the frequency tripler, so that the final output power is enough for high speed wireless THz links.

6.4 Pautas para futuras investigaciones

Hay algunos puntos que pueden ser clave para la mejora del rendimiento de los dispositivos presentados en esta tesis.

- *La aplicación de las técnicas de empaquetado descritas en el capítulo 2 al desarrollo del mezclador; de esta manera se podría evitar el uso del canal de aire, facilitar el ensamblado y corte del substrato y también mejorar el comportamiento de la transición de tecnología planar a guía de onda.*
- *Integrar el oscilador local en el mismo substrato que el mezclador armónico gracias a la disponibilidad de dispositivos que funcionan en tecnología planar a frecuencias milimétricas.*
- *Integración de amplificador LNA en banda W a la salida del fotodiodo para obtener una potencia suficiente que al alcanzar los diodes del triplicador de frecuencia logren una potencia de salida factible para el funcionamiento de un enlace de alta velocidad en frecuencia de terahercio.*

Appendices

Appendix A

Photolithography

The fabrication of the prototypes has been realized by means of a standard photolithography procedure. This can be described as the process that transfers an specific pattern, which has been previously plotted into a photomask, into a photoresist using ultraviolet light. An schematic of this process at the Group of Antennas cleanroom facility is shown in Figure A.1.

Figure A.1: Schematic of the photolithography procedure at the Public University of Navarra's facilities.

In this case, we have used the AZ nLof2070 negative photoresist with 7 μm thickness. Taking this into account, the procedure can be determined by the main following steps:

- **Photoresist deposition:** previously the substrate has been cleaned with acetone and isopropyl alcohol. Using the SpinCoater a 7 μm photoresist layer is deposited on the Topas COC substrate.
- **Exposure:** After deposition, the photoresist must be baked for 90 seconds. Then, the exposure is realized, transferring the pattern from the photomask to the photoresist. In order to do that, the Mask Aligner MJB4 is used during 15 seconds.
- **Metallization:** Once the pattern has been transferred, we have to make a post exposure bake and use the AZ726mif developer for 2 minutes to properly remove the not exposed photoresist. Then, using the E-Beam Evaporator, the metallization of 20 nm of chrome in order to improve the adherence of copper is realized. Afterwards 2 um of copper are deposited.
- **Stripping:** Now the whole substrate is metallized. Therefore, we have to remove the photoresist with the copper. The NI555 stripper is employed for this purpose.

After the circuits are metallized it is necessary to cut the substrate. In this facility, the process is done with a Dicing Dicing Saw (DAD 321). For the assembly, firstly the Schottky diodes must be shaped using also Disco Dicing machine. Once they have been cut, they are welded to the microstrip circuit by means of silver epoxy (EPOTEK H20E). Placing of the silver epoxy and afterwards, of the diodes, is realized with the wire bonding and die placing machine (TPT HB16D). An image of the DAD321 and TPT HB16D can be seen in Figure A.2.

Once the diodes are placed, we heat the silver epoxy at 105^{o}C for an hour. An image of the welded diodes can be seen in Figure A.3.

Finally the I-V curve of a UMS schottky diodes is checked to be sure they are well welded. An example of a measurement of one I-V curve is shown in Figure A.4.

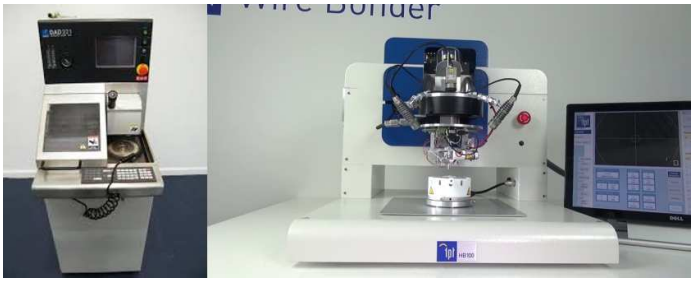

Figure A.2: Pictures of the: (Left) Dicing Saw DAD321 and (Right) TPT HB16D die bonder.

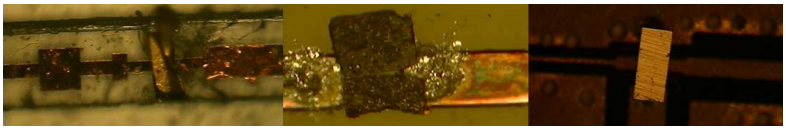

Figure A.3: Welded diodes.(Left) Antiseries Schottky Diodes configuration for doubler multiplier. (Center) Antiparallel Schottky Diodes for subharmonic mixer. (Rigth) Balance diodes featuring antiparallel configuration for the tripler multiplier.

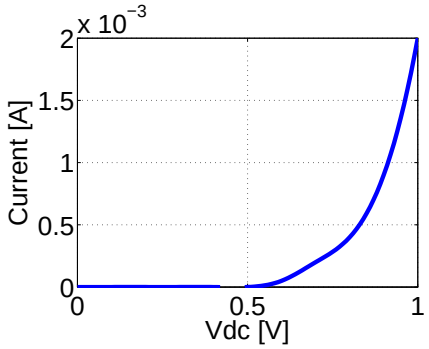

Figure A.4: I-V measured curve of an UMS Schottky diode.

Appendix B

Prototype dimensions and pictures of the receivers and transmitter

In this Appendix we compiled the layout of the receivers and the transmitter devices, their dimensions and some pictures of the prototypes that have been fabricated in the cleanroom at Public University of Navarra.

B.1 Dimension drawing of the prototypes

Firstly, the whole layout the fourth harmonic mixer is shown in Figure B.1. The layout of the combined doubler/sub-harmonic mixer is shown in Figure B.2. The schematic of the frequency tripler multiplier is shown in Figure B.3. Finally, the sixth harmonic mixer and its annotation of dimensions is shown in Figure B.4.

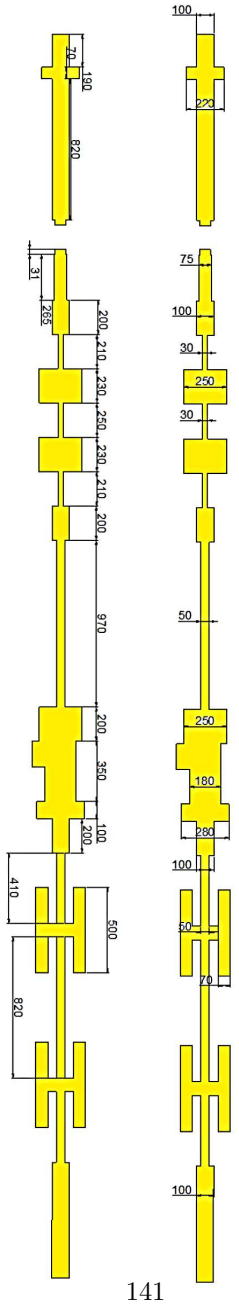

Figure B.1: Layout and dimensions of the fourth harmonic mixer.

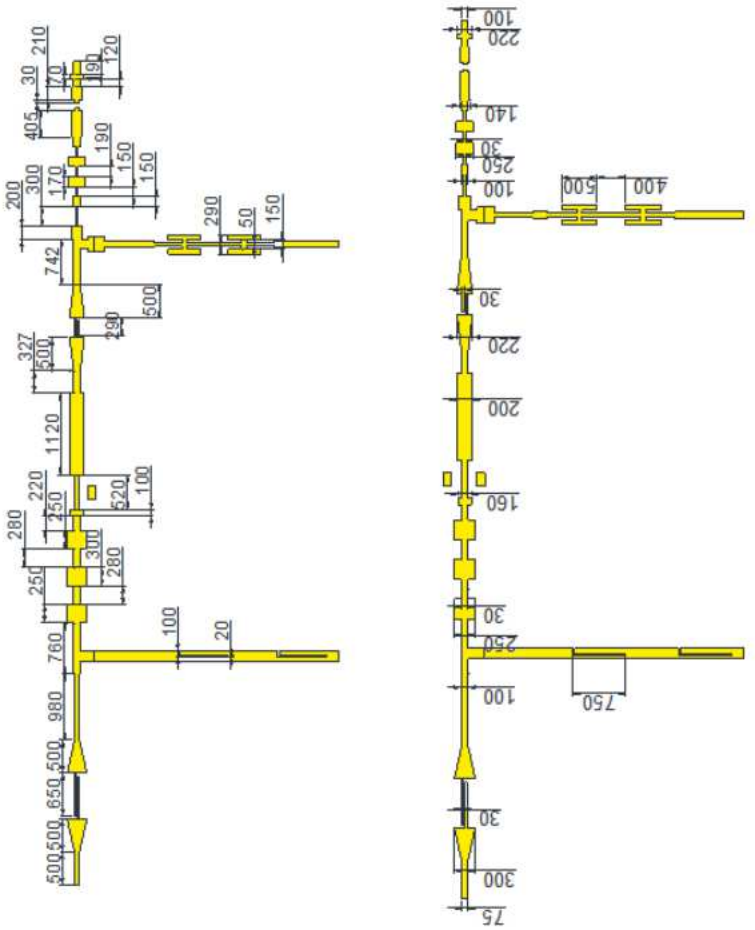

Figure B.2: Layout and dimensions of the combined doubler/sub-harmonic mixer.

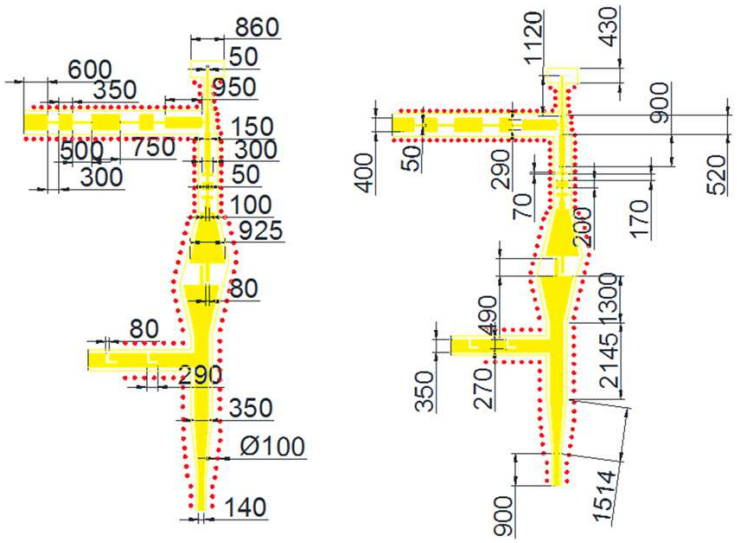

Figure B.3: Layout and dimensions of the frequency tripler multiplier.

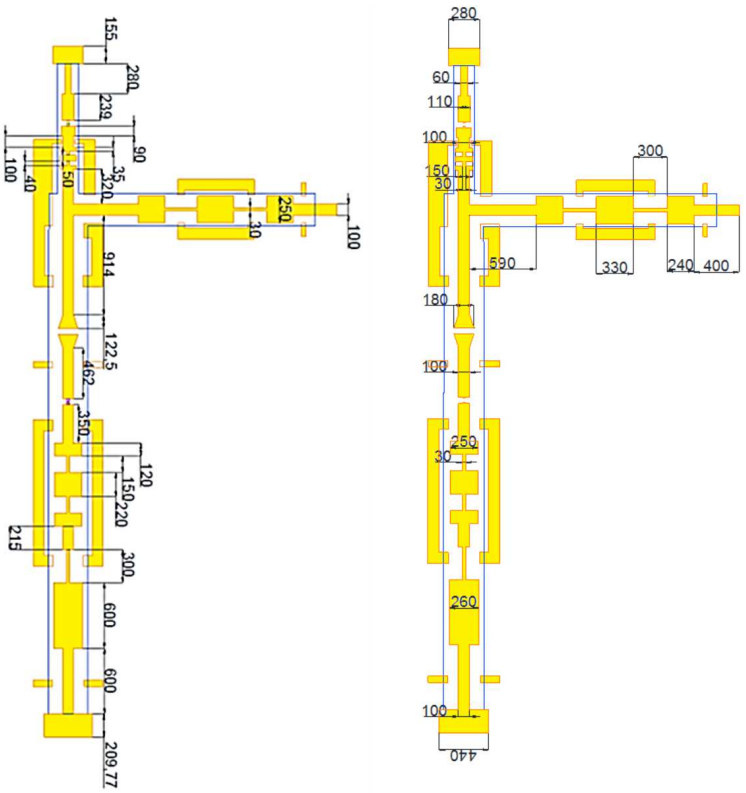

Figure B.4: Layout and dimensions of the integrated tripler/subharmonic mixer layout.

B.2 Pictures of the fabricated prototypes

Pictures has been taken with the Mitutoyo Hyper MF-U 176-402-43 measuring microscope. Images of the fourth harmonic circuit are shown in Figure B.5.

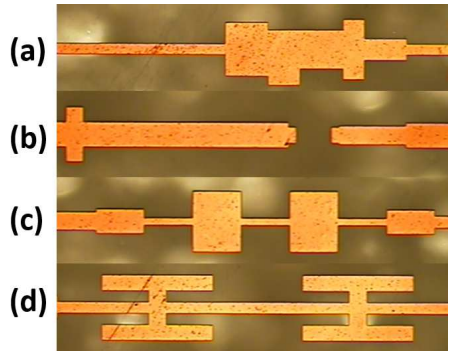

Figure B.5: Pictures of the fourth harmonic mixer fabrication. (a) Tee for the local oscillator; (b) Waveguide E-Probe transition; (c) Low pass filter and (d) Hammerhead filter.

Pictures of the doubler of the subharmonic mixer can be seen in Figure B.6.

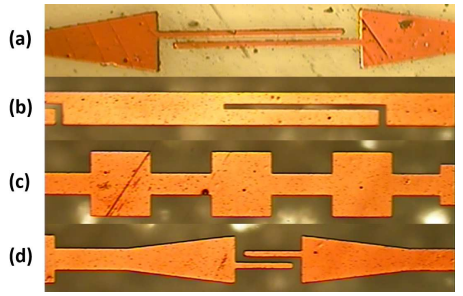

Figure B.6: Pictures of the doubler of the subharmonic mixer fabrication. (a) DC-Block for LO; (b) Low pass filter for DC feed; (c) Low pass filter for LO and (d) DC-Block for 2×LO.

Pictures of the sub harmonic mixer in Figure B.7.

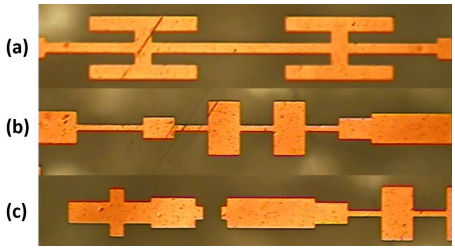

Figure B.7: Pictures of the subharmonic mixer fabrication.(a)Hammerhead filter for IF frequency; (b) Low pass filter for 2×LO and (c) Waveguide E-probe transition.

Appendix C

Y-Factor Measurement

The Y-factor technique is the most employed method in the characterization of amplifiers and mixers [Tec14, Roh12, Rä80]. It is used for characterizing the gain and the noise temperature. There are three different alternatives for measuring the Y-Factor: the attenuator procedure, noise-injection procedure and the gain procedure.

In order to make the Y-factor measurement, the device under test (DUT) (in this case a mixer) is connected to a noise source. Then, the power is measured for both cases, with the noise source ON and OFF. The ratio of these two values establish a line that determines the DUT gain, see Figure C.1.

The Y-factor is then computed as:

$$Y = \frac{N_{ON}}{N_{OFF}} \tag{C.1}$$

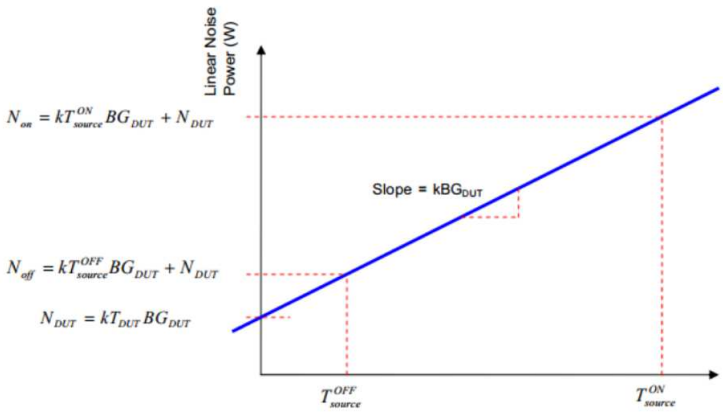

Figure C.1: Y-Factor variables (Image obtained from [Roh12]).

C.1 Attenuator Procedure

This measurement procedure is performed with and without a coaxial attenuator connected to the input of the IF chain. The receiver Y-Factor measurements are performed presenting the hot and cold load to the receiver input. Without the attenuator the Y-Factor of the receiver is:

$$Y_{rx} = \frac{P_{HOT}}{P_{COLD}} = \frac{T_{HOT} + T_{rx}}{T_{COLD} + T_{rx}} \tag{C.2}$$

Rearranging the noise temperature, we have the following equation:

$$T_{rx} = \frac{T_{HOT} - Y_{rx}T_{COLD}}{Y_{rx} - 1} \tag{C.3}$$

With the attenuator we have:

$$Y_{rx,att} = \frac{P_{HOT}}{P_{COLD}} = \frac{T_{HOT} + T_{rx,att}}{T_{COLD} + T_{rx,att}} \tag{C.4}$$

Thus,

$$T_{rx,att} = \frac{T_{HOT} - Y_{rx,att}T_{COLD}}{Y_{rx,att} - 1} \tag{C.5}$$

Equating the two equations

$$T_{rx} = T_{mix} + L_{mix}T_{IF} \tag{C.6}$$

$$T_{rx,att} = T_{mix} + L_{mix}T_{IF,att} \tag{C.7}$$

Then, the conversion loss and the noise temperature of the mixer are calculated from

$$L_{mix} = \frac{T_{rx} - T_{rx,att}}{T_{IF} - T_{IF,att}} \tag{C.8}$$

$$T_{mix} = T_{rx} - L_{mix}T_{IF} \tag{C.9}$$

C.2 Noise-Injection Procedure

This procedure is similar to that described in the previous section. The noise is injected into the input of the IF chain with a noise source and a directional coupler. Then the Y-factor is computed as follows.

With the noise source OFF, the receiver Y-Factor is:

$$Y_{OFF} = \frac{P_{HOT}}{P_{COLD}} = \frac{T_{HOT} + T_{rx,OFF}}{T_{COLD} + T_{rx,OFF}} \tag{C.10}$$

Then, the noise temperature of the receiver is:

$$T_{rx,OFF} = \frac{T_{HOT} - Y_{OFF}T_{COLD}}{Y_{OFF} - 1} \tag{C.11}$$

With the noise source ON, the receiver Y-Factor is:

$$Y_{ON} = \frac{P_{HOT}}{P_{COLD}} = \frac{T_{HOT} + T_{rx,ON}}{T_{COLD} + T_{rx,ON}} \tag{C.12}$$

In this case, the noise temperature of the receiver is:

$$T_{rx,ON} = \frac{T_{HOT} - Y_{ON}T_{COLD}}{Y_{ON} - 1} \tag{C.13}$$

Equating the two equations we have:

$$T_{rx,OFF} = T_{mix} + L_{mix}T_{IF,OFF} \tag{C.14}$$

$$T_{rx,ON} = T_{mix} + L_{mix}T_{IF,ON} \tag{C.15}$$

Finally, the conversion loss and noise temperature of the mixer are calculated as:

$$L_{mix} = \frac{T_{rx,OFF} - T_{rx,ON}}{T_{IF,OFF} - T_{IF,ON}} \tag{C.16}$$

$$T_{mix} = T_{rx,OFF} - L_{mix}T_{IF,OFF}. \tag{C.17}$$

C.3 Gain Procedure

For the measurement we use two noise temperatures, one of them is ambient temperature (T_{HOT} = 273 K) and the other one is cold (T_{COLD} = 77 K), obtained by means of a liquid nitrogen immersed load.

The power at the receiver is:

$$P_{rx} = (T_{rx} + T_R)k_B G_r x B \tag{C.18}$$

where T_{rx} is the equivalent noise temperature of the receiver, T_R is the room temperature T_{COLD} and T_{HOT}, G_{rx} is the gain, B is the bandwidth and k_B is Boltzmann's constant.

The Y-factor is:

$$Y_{rx} = \frac{P_{HOT_{rx}}}{P_{COLD_{rx}}} \tag{C.19}$$

where the measurement of the receiver are

$$P_{HOT,rx} = (T_{rx} + T_{HOT})k_B G_{rx} B \tag{C.20}$$

$$P_{COLD,rx} = (T_{rx} + T_{COLD})k_B G_{rx} B \tag{C.21}$$

and the receiver gain, therefore is

$$G_{rx} = \frac{P_{HOT,rx} - P_{COLD,rx}}{k_B B(T_{HOT} - T_{COLD})} \tag{C.22}$$

From the IF chain we obtain

$$P_{HOT,rx} = (T_{IF} + T_{HOT})k_B G_{rx} B \tag{C.23}$$

$$P_{COLD,rx} = (T_{IF} + T_{COLD})k_B G_{rx} B \tag{C.24}$$

which results in

$$G_{IF} = \frac{P_{HOT,IF} - P_{COLD,IF}}{k_B B(T_{HOT} - T_{COLD})} \tag{C.25}$$

and finally the conversion loss of the mixer is

$$L_{mix} = \frac{1}{G_{mix}} = \frac{P_{HOT,IF} - P_{COLD,IF}}{P_{HOT,rx} - P_{COLD,rx}} \tag{C.26}$$

Once the conversion loss is calculated, the noise temperature is computed using the Equation C.9.

Appendix D

Triquint Datasheet

TriQuint SEMICONDUCTOR

TGV2204-FC

19 GHz VCO with Prescaler

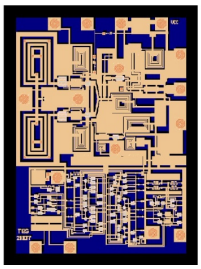

Measured Performance

Bias conditions: Vcc = 5 V, Itotal = 165 mA

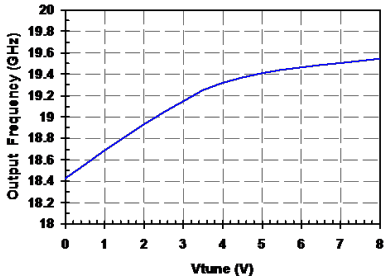

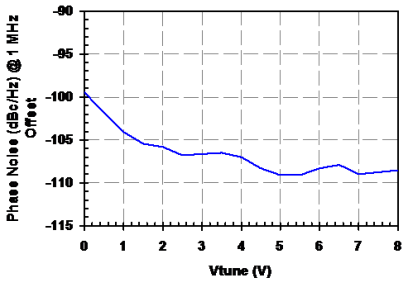

Key Features

- Frequency Range: 18.5 – 19.5 GHz
- Output Power: 7 dBm @ 19 GHz
- Phase Noise: -105 dBc/Hz at 1 MHz offset, fc=19 GHz
- Prescaler Output Freq Range : 2.31 – 2.44 GHz
- Prescaler Output Power: -6 dBm
- Bias: Vcc = 5 V, Itotal = 165 mA Typical
- Technology: HBT3
- Chip Dimensions: 1.28 x 1.71 x 0.38 mm

Primary Applications

- Automotive Radar

Product Description

The TriQuint TGV2204-FC is a flip-chip voltage controlled oscillator (VCO) designed to operate at frequencies that target the automotive Radar market. The TGV2204-FC is designed using TriQuint's proven HBT3 process and front-side Cu / Sn pillar technology for simplified assembly and low interconnect inductance.

The TGV2204-FC is a VCO that typically provides 7 dBm output power at 19 GHz with < -105 dBc/Hz phase noise at 1 MHz offset . The integrated divide-by-8 prescaler eases PLL design. The TGV2204-FC is an excellent choice for applications requiring frequency stability in transmit chain architectures.

The TGV2204-FC has a protective surface passivation layer providing environmental robustness.

Lead-free and RoHS compliant.

TriQuint Semiconductor: www. triquint.com (972)994-8465 Fax (972)994-8504 Info-mmw@tqs.com

TriQuint SEMICONDUCTOR

TGV2204-FC

Table I
Absolute Maximum Ratings 1/

Symbol	Parameter	Value	Notes
Vcc	Collector Voltage	11 V	2/
Vtune	Tune Voltage	11 V	
Itotal	Collector Current	276 mA	2/

1/ These ratings represent the maximum operable values for this device. Stresses beyond those listed under "Absolute Maximum Ratings" may cause permanent damage to the device and / or affect device lifetime. These are stress ratings only, and functional operation of the device at these conditions is not implied.

2/ Combinations of supply voltage, supply current shall not exceed the maximum power dissipation listed in Table IV.

Table II
Recommended Operating Conditions

Symbol	Parameter 1/	Value
Vcc	Collector Voltage	5 V ± 5%
Itotal	Collector Current	165 mA
Vtune	VCO Freq Tune Voltage	0-8 V

1/ See assembly diagram for bias instructions.

TriQuint Semiconductor: www. triquint.com (972)994-8465 Fax (972)994-8504 Info-mmw@tqs.com

TriQuint SEMICONDUCTOR

TGV2204-FC

Table III
RF Characterization Table

Bias: Vcc = 5 V, Itotal = 165 mA, typical

SYMBOL	PARAMETER	TEST CONDITIONS	MINIMUM	NOMINAL	MAXIMUM	UNITS
RF Out	Output Power	f = 19 – 19.25 GHz	5	7	13	dBm
PN	Phase Noise @ 1 MHz Offset	f = 19 – 19.25 GHz		-107		dBc/Hz
F/8 Pout 1/	Prescaler Output Power 1/	f = 19 – 19.25 GHz	-11	-6	2	dBm
F/8 Freq	Prescaler Output Frequency	f = 19 – 19.25 GHz		2.31 – 2.44		GHz
Fout 2V	Output Frequency, Vtune = 2 V		18.6	18.95	19.2	GHz
Fout 8V	Output Frequency, Vtune = 8 V		19.4	19.56	20.0	GHz

1/ Single-ended output power measurement

TriQuint Semiconductor: www. triquint.com (972)994-8465 Fax (972)994-8504 Info-mmw@tqs.com

TriQuint SEMICONDUCTOR

TGV2204-FC

Table IV
Power Dissipation and Thermal Properties

Parameter	Test Conditions	Value	Notes
Maximum Power Dissipation	Tbaseplate = 70 ºC	Pd = TBD W Tjunction = TBD ºC Tm = TBD Hrs	1/ 2/
Thermal Resistance, θjc	Vcc= 5 V Id = 165 mA Pd = 0.825 W Tbaseplate = 70 ºC	θjc = 80.4 (ºC/W) Tjunction = 133.5 ºC Tm = TBD Hrs	
Mounting Temperature		Refer to Solder Reflow Profiles (pp 11)	
Storage Temperature		-65 to 150 ºC	

1/ For a median life of 1E+6 hours, Power Dissipation is limited to

Pd(max) = (150 ºC – Tbase ºC)/θjc.

2/ Junction operating temperature will directly affect the device median time to failure (MTTF). For maximum life, it is recommended that junction temperatures be maintained at the lowest possible levels.

Median Lifetime (Tm) vs Channel Temperature

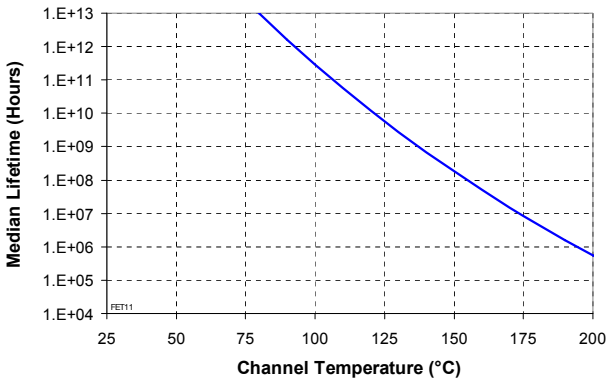

TriQuint Semiconductor: www. triquint.com (972)994-8465 Fax (972)994-8504 Info-mmw@tqs.com

TriQuint SEMICONDUCTOR

TGV2204-FC

Measured Data on Face-down (flipped) Die on Carrier Board

Bias conditions: Vcc = 5 V, Itotal = 165 mA

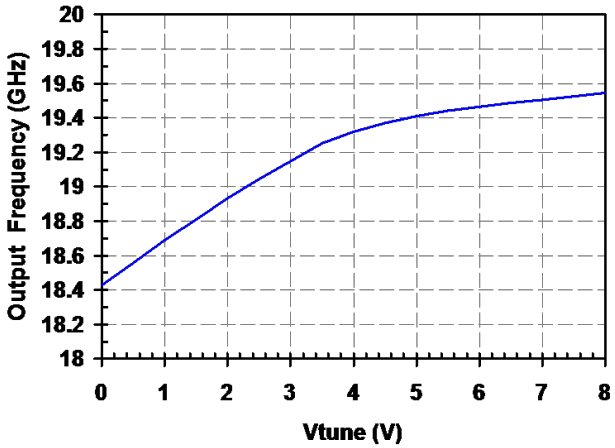

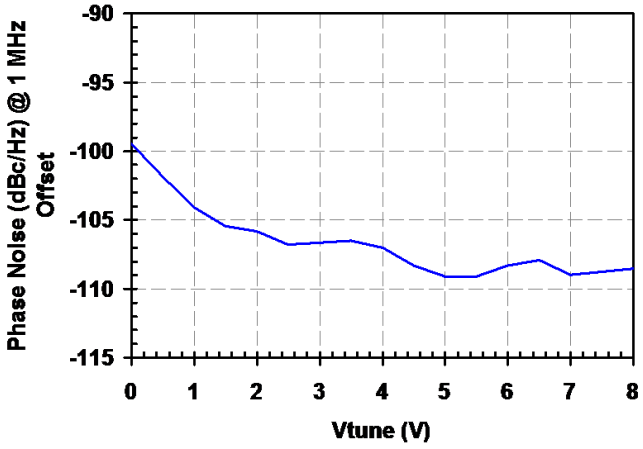

TriQuint Semiconductor: www. triquint.com (972)994-8465 Fax (972)994-8504 Info-mmw@tqs.com

TriQuint SEMICONDUCTOR

TGV2204-FC

Measured Data on Face-down (flipped) Die on Carrier Board

Bias conditions: Vcc = 5 V, Itotal = 165 mA

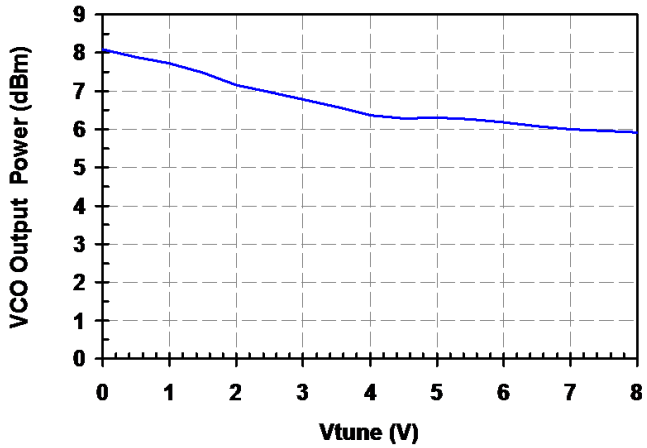

TriQuint Semiconductor: www. triquint.com (972)994-8465 Fax (972)994-8504 Info-mmw@tqs.com

TriQuint SEMICONDUCTOR

TGV2204-FC

Electrical Schematic

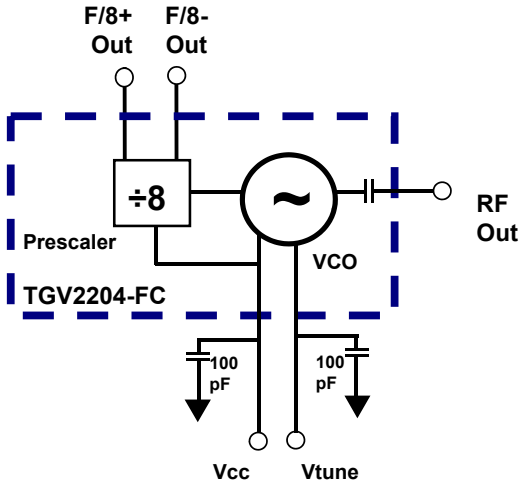

Bias Procedures

Bias-up Procedure

Vtune set to ~ +2 V (for desired Freq)

Vcc set to 5 V ± 5%

For single-ended use of the prescaler (F/8+), the F/8- output pin may be left open

Bias-down Procedure

Reduce Vcc to 0 V.

Turn Vtune to 0 V

TriQuint Semiconductor: www. triquint.com (972)994-8465 Fax (972)994-8504 Info-mmw@tqs.com

TriQuint SEMICONDUCTOR

TGV2204-FC

Mechanical Drawing

Drawing is for chip face-up

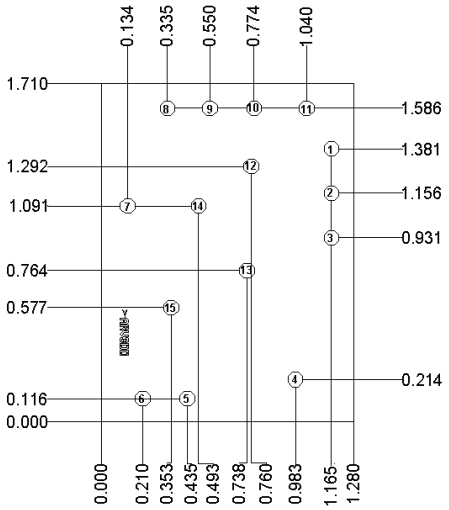

Units: millimeters
Thickness: 0.38
Die x,y size tolerance: +/- 0.050
Chip edge to pillar dimensions are shown to center of pillar

Pillar #4, 7, 10, 12-15	DC Ground	0.075 ϕ	Pillar #6	Prescaler Out (F/8+)	0.075 ϕ
Pillar #1, 3	RF CPW Ground	0.075 ϕ	Pillar #8	Vtune	0.075 ϕ
Pillar #2	RF Out	0.075 ϕ	Pillar #9	Vbb (Not Used)	0.075 ϕ
Pillar #5	Prescaler Out (F/8-)	0.075 ϕ	Pillar #11	Vcc	0.075 ϕ

GaAs MMIC devices are susceptible to damage from Electrostatic Discharge. Proper precautions should be observed during handling, assembly and test.

TriQuint Semiconductor: www. triquint.com (972)994-8465 Fax (972)994-8504 Info-mmw@tqs.com

TriQuint SEMICONDUCTOR

TGV2204-FC

Recommended Assembly Diagram

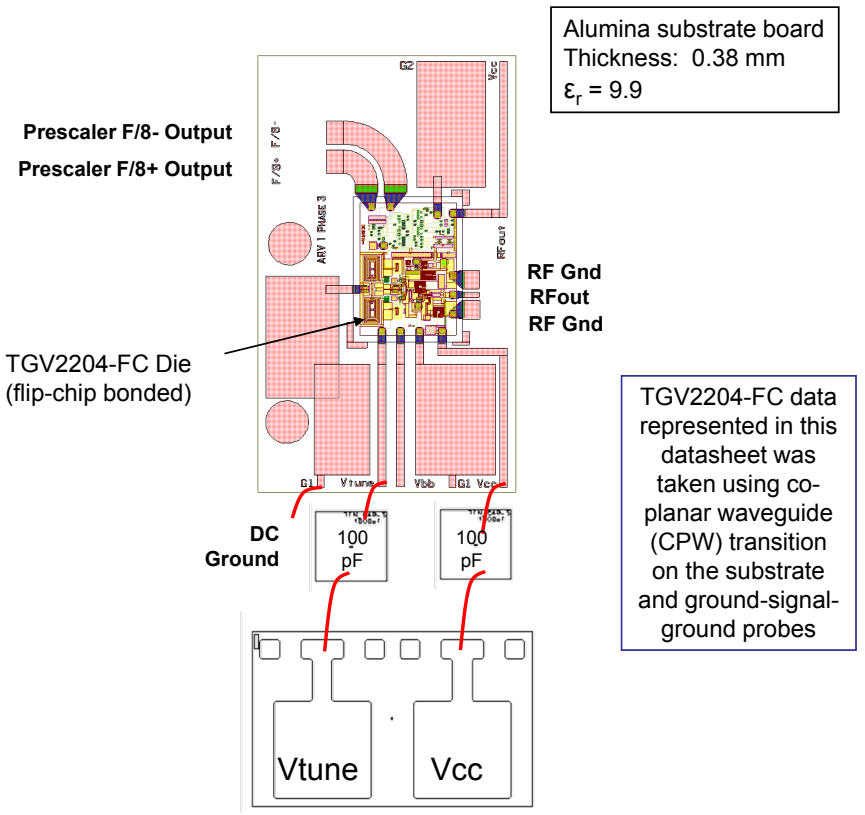

Die is flip-chip bonded / bumped to carrier

NOTE: Vcc should be bypassed sufficiently to avoid phase noise degradation. Bypass capacitors of 1 uF and 470 uF are recommended. Tuning port should also be free of supply noise.

GaAs MMIC devices are susceptible to damage from Electrostatic Discharge. Proper precautions should be observed during handling, assembly and test.

TriQuint Semiconductor: www. triquint.com (972)994-8465 Fax (972)994-8504 Info-mmw@tqs.com

TriQuint SEMICONDUCTOR

TGV2204-FC

Assembly Notes

Component placement and die attach assembly notes:

- Vacuum pencils and/or vacuum collets are the preferred method of pick up.
- Air bridges must be avoided during placement.
- Cu pillars on die are 65 um tall with a 22 um tall Sn solder cap.
- Recommended board metallization is evaporated TiW followed by nickel/gold at pillar attach interface. Ni is the adhesion layer for the solder and the gold keeps the Ni from oxidizing. The Au should be kept to a minimum to avoid embrittlement; suggested Au / Sn mass ratio must not exceed 8%.
- Au metallization is not recommended on traces due to solder wicking and consumption concerns. If Au traces are used, a physical solder barrier must be applied or designed into the pad area of the board. The barrier must be sufficient to keep the solder from undercutting the barrier.

Reflow process assembly notes:

- Minimum alloying temperatures 245 C.
- Repeating reflow cycles is not recommended due to Sn consumption on the first reflow cycle.
- An alloy station or conveyor furnace with an inert atmosphere such as N2 should be used.
- Dip copper pillars in “no-clean flip chip” flux prior to solder attach. Suggest using a high temperature flux. Avoid exposing entire die to flux.
- If screen printing flux, use small apertures and minimize volume of flux applied.
- Coefficient of thermal expansion matching between the MMIC and the substrate/board is critical for long-term reliability.
- Devices must be stored in a dry nitrogen atmosphere.
- Suggested reflow will depend on board material and density.

See Triquint Application Note for flip-chip soldering process: TBD

Typical Reflow Profiles for TriQuint Cu / Sn Pillars

Process	Sn Reflow
Ramp-up Rate	3 ºC/sec
Flux Activation Time and Temperature	60 – 120 sec @ 140 – 160 ºC
Time above Melting Point (245 C)	60 – 150 sec
Max Peak Temperature	300 ºC
Time within 5 ☐C of Peak Temperature	10 – 20 sec
Ramp-down Rate	4 – 6 ºC/sec

Ordering Information

Part	Package Style
TGV2204-FC	GaAs MMIC Die

GaAs MMIC devices are susceptible to damage from Electrostatic Discharge. Proper precautions should be observed during handling, assembly and test.

TriQuint Semiconductor: www. triquint.com (972)994-8465 Fax (972)994-8504 Info-mmw@tqs.com

TriQuint SEMICONDUCTOR

TGC4703-FC

19 to 38 GHz Doubler

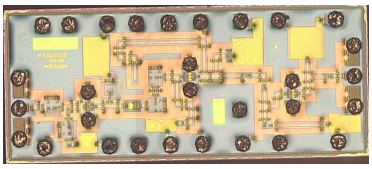

Measured Performance

Bias conditions: Vd = 3.5 V, Vg1 = -0.4 V, Vg2 = +0.2 V, Idq = 65 mA Typical

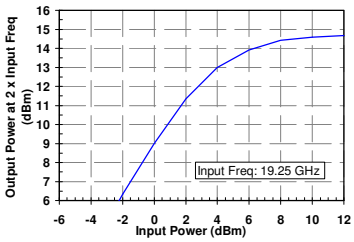

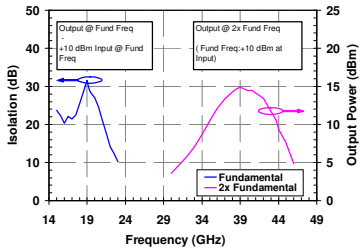

Key Features

- RF Output Frequency Range: 38 – 38.5 GHz
- Input Frequency Range: 19 – 19.25 GHz
- 14 dBm saturated Output Power
- 8 dB nominal Conversion Gain
- 30 dB input Frequency Isolation at output
- Input Return Loss > 15 dB
- Output Return Loss > 8 dB
- Bias: Vd = 3.5 V, Idq = 65mA, Vg1 = -0.4 V, Vg2 = +0.2 V Typical
- Technology: 0.13 um pHEMT with front-side Cu/Sn pillars
- Chip Dimensions: 1.16 x 2.85 x 0.38 mm

Primary Applications

- Automotive Radar
- E-Band Communication

Product Description

The TriQuint TGC4703-FC is a flip-chip frequency doubler. It combines an input and output buffer amplifier and a frequency doubler for use in automotive radar. The TGC4703-FC is designed using TriQuint's proven 0.13 µm pHEMT process and front-side Cu / Sn pillar technology for simplified assembly and low interconnect inductance. Die reliability is enhanced by using TriQuint's BCB polymeric passivation process.

The TGC4703-FC typically provides 14 dBm saturated output power with 8 dB conversion gain.

Lead-free and RoHS compliant.

TriQuint Semiconductor: www. triquint.com (972)994-8465 Fax (972)994-8504 Info-mmw@tqs.com

TriQuint SEMICONDUCTOR

TGC4703-FC

Table I
Absolute Maximum Ratings 1/

Symbol	Parameter	Value	Notes
Vd-Vg	Drain to Gate Voltage	5.5 V	
Vd	Drain Voltage	4.0 V	
Vg	Gate Voltage Range	-1 to +0.45 V	
Id	Drain Current	170 mA	
Ig	Gate Current Range	-0.5 to +3.0 mA	
Pin	Input Continuous Wave Power	13 dBm	

1/ These ratings represent the maximum operable values for this device. Stresses beyond those listed under "Absolute Maximum Ratings" may cause permanent damage to the device and / or affect device lifetime. These are stress ratings only, and functional operation of the device at these conditions is not implied.

Table II
Recommended Operating Conditions

Symbol	Parameter 1/	Value
Vd	Drain Voltage	3.5 V
Idq	Drain Current, No RF signal at Input	65 mA
Id	Drain Current, RF signal at Input	135 mA
Vg1	Multiplier Stage Gate Voltage	-0.4 V
Vg2a, Vg2b	Amplifier Stages Gate Voltage	+0.2 V

1/ See electrical schematic diagram for bias instructions.

TriQuint Semiconductor: www. triquint.com (972)994-8465 Fax (972)994-8504 Info-mmw@tqs.com

TriQuint SEMICONDUCTOR

TGC4703-FC

Table III
RF Characterization Table

Bias: Vd = 3.5 V, Idq = 65 mA, Vg1 = -0.4 V, Vg2 = +0.2 V Typical

SYMBOL	PARAMETER	TEST CONDITIONS	MINIMUM	NOMINAL	UNITS
IRL	Input Return Loss	Fin = 19.00 –19.25 GHz		15	dB
ORL	Output Return Loss	Fin = 38.00 – 38.50 GHz		8	dB
Pout	Output Power (RFin = 0 dBm)	Fin = 19.25 GHz Fout = 38.5 GHz	8	10.5	dBm
Pout	Output Power (RFin = 6 dBm)	Fin = 19.25 GHz Fout = 38.5 GHz	12.5	13.5	dBm
Isol	Isolation	Fin = 19.00 –19.25 GHz Fout = 19.00 –19.25 GHz		30	dB

TriQuint Semiconductor: www. triquint.com (972)994-8465 Fax (972)994-8504 Info-mmw@tqs.com

TriQuint SEMICONDUCTOR

TGC4703-FC

Table IV
Power Dissipation and Thermal Properties

Parameter	Test Conditions	Value	Notes
Maximum Power Dissipation	Tbaseplate = 126.5 °C	Pd = 0.560 W Tchannel = 150 °C Tm = 2.4E+7 Hrs	1/ 2/ 3/
Thermal Resistance, θjc	Vd = 3.5 V Vg1 = -0.4 V Vg2 = +0.2 V Id = 0.135 A Pd = 0.473 W Tbaseplate = 85 °C	θjc = 42 (°C/W) Tchannel = 104 °C Tm = 6.6E+9 Hrs	3/
Mounting Temperature		Refer to Solder Reflow Profiles (pp 11)	
Storage Temperature		-65 to 150 °C	

1/ For a median life of 2.4E+7 hours, Power Dissipation is limited to

Pd(max) = (150 °C – Tbase °C)/θjc.

2/ Channel operating temperature will directly affect the device median time to failure (MTTF). For maximum life, it is recommended that channel temperatures be maintained at the lowest possible levels.

3/ For this flip-chip die, the baseplate is a plane between the Cu/Sn pillars and the test board. For the TGC4703-FC, the critical pillars for thermal power dissipation are 24 thru 28 and 30. (See Mechanical Drawing.)

Median Lifetime (TM) vs Channel Temperature

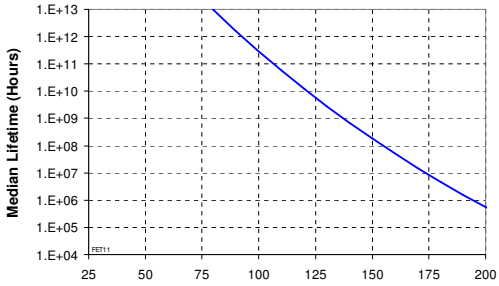

TriQuint Semiconductor: www. triquint.com (972)994-8465 Fax (972)994-8504 Info-mmw@tqs.com

TriQuint SEMICONDUCTOR

TGC4703-FC

Measured Data on Flipped Die on Carrier Board

Bias conditions: Vd = 3.5 V, Idq = 65 mA, Vg1 = -0.4 V Vg2 = +0.2 V Typical

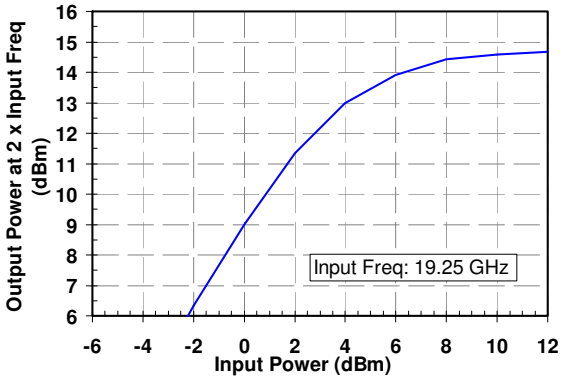

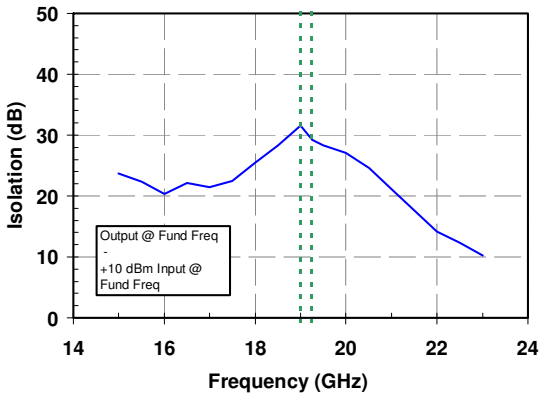

TriQuint Semiconductor: www. triquint.com (972)994-8465 Fax (972)994-8504 Info-mmw@tqs.com
November 2009 © Rev A

TriQuint SEMICONDUCTOR

TGC4703-FC

Measured Data on Flipped Die on Carrier Board

Bias conditions: Vd = 3.5 V, Idq = 65 mA, Vg1 = -0.4 V Vg2 = +0.2 V Typical

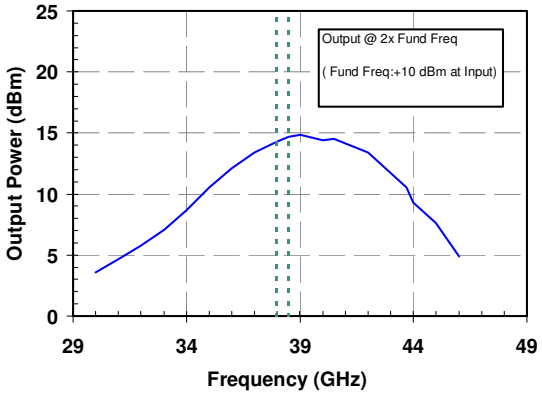

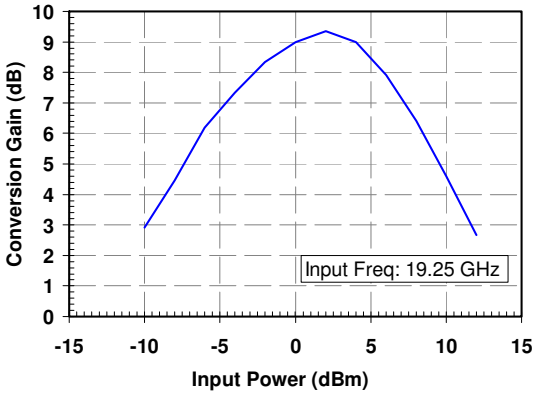

TriQuint Semiconductor: www. triquint.com (972)994-8465 Fax (972)994-8504 Info-mmw@tqs.com
November 2009 © Rev A

TriQuint SEMICONDUCTOR

TGC4703-FC

Measured Data on Flipped Die on Carrier Board

Bias conditions: Vd = 3.5 V, Idq = 65 mA, Vg1 = -0.4 V Vg2 = +0.2 V Typical

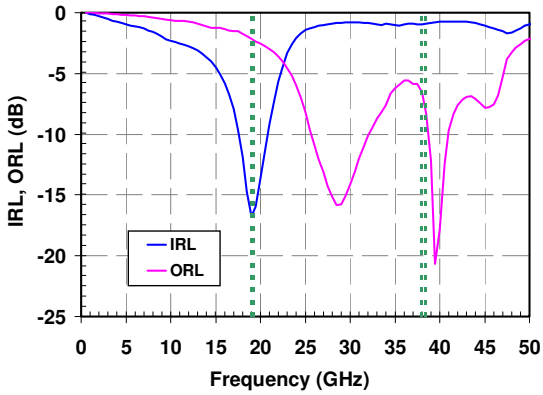

TriQuint Semiconductor: www. triquint.com (972)994-8465 Fax (972)994-8504 Info-mmw@tqs.com

TriQuint SEMICONDUCTOR

TGC4703-FC

Electrical Schematic

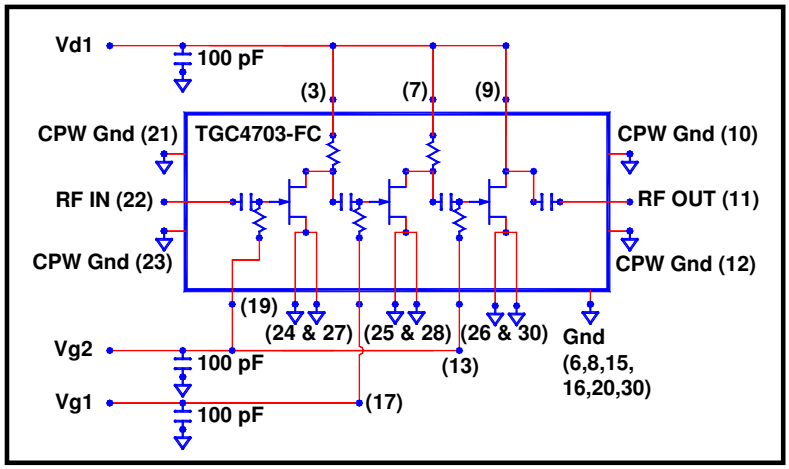

Bias Procedures

Bias-up Procedure

Vg1, Vg2 set to -0.4 V

Vd set to +3.5 V

Adjust Vg2 ONLY more positive until Id is 65 mA (Vg ~ +0.2 V)

Apply RF signal to input
Id will be ~135 mA

Bias-down Procedure

Turn off RF signal to input

Reduce Vg1, Vg2 to -0.4 V. Ensure Id ~ 0 mA

Turn Vd to 0 V

TriQuint Semiconductor: www. triquint.com (972)994-8465 Fax (972)994-8504 Info-mmw@tqs.com

TriQuint SEMICONDUCTOR

TGC4703-FC

Mechanical Drawing

Drawing is for chip face-up

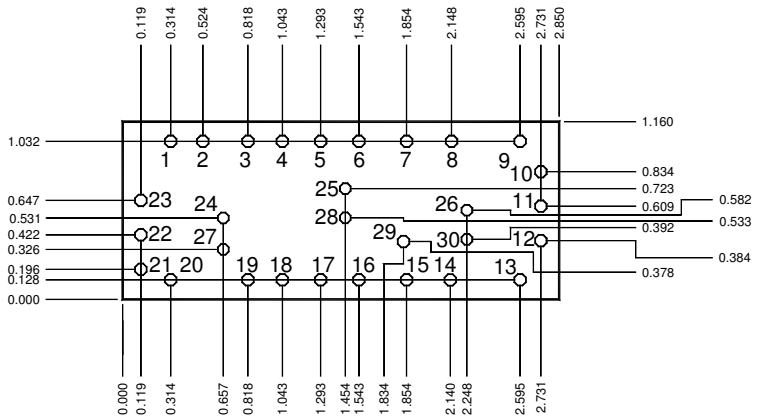

Units: millimeters Thickness: 0.380

Die x,y size tolerance: +/- 0.050

Chip edge to pillar dimensions are shown to center of pillar

Pillar #22	RF In	0.075 Ø
Pillar #11	RF Out	0.075 Ø
Pillar #10, 12, 21, 23	RF CPW Ground	0.075 Ø
Pillar #17	Vg1	0.075 Ø
Pillar #19	Vg2a	0.075 Ø
Pillar #13	Vg2b	0.075 Ø

Pillar #7	Vd1	0.075 Ø
Pillar #3	Vd2a	0.075 Ø
Pillar #9	Vd2b	0.075 Ø
Pillar #6, 8, 15, 16, 20, 24-28, 30	DC Ground	0.075 Ø
Pillar #1, 2, 4, 5, 14, 18, 29	Mech. Support Only	0.075 Ø

GaAs MMIC devices are susceptible to damage from Electrostatic Discharge. Proper precautions should be observed during handling, assembly and test.

TriQuint Semiconductor: www. triquint.com (972)994-8465 Fax (972)994-8504 Info-mmw@tqs.com

TriQuint SEMICONDUCTOR

TGC4703-FC

Recommended Assembly Diagram

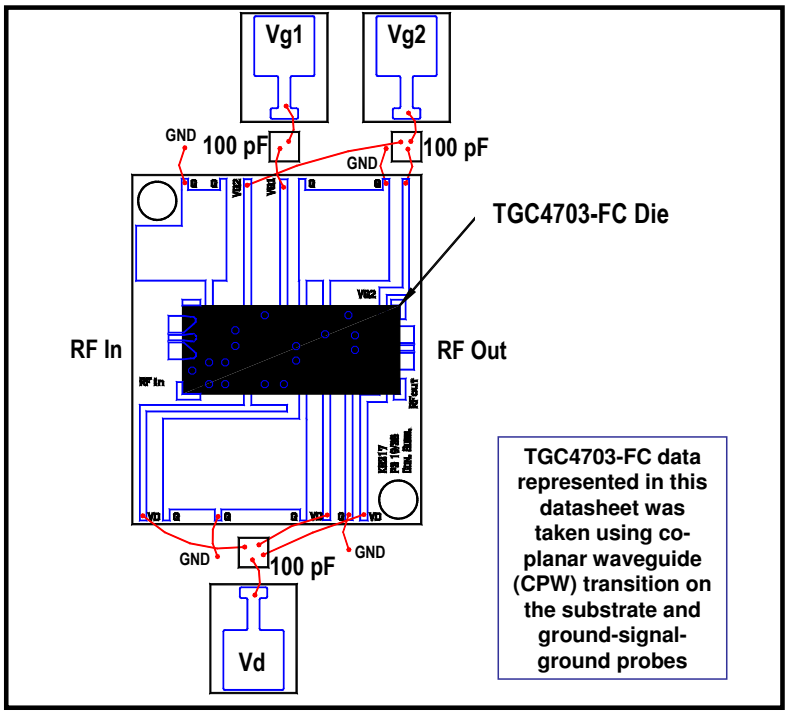

Die is flip-chip soldered to a 15 mil thick alumina test substrate

GaAs MMIC devices are susceptible to damage from Electrostatic Discharge. Proper precautions should be observed during handling, assembly and test.

TriQuint Semiconductor: www. triquint.com (972)994-8465 Fax (972)994-8504 Info-mmw@tqs.com

TriQuint SEMICONDUCTOR

TGC4703-FC

Assembly Notes

Component placement and die attach assembly notes:

- Vacuum pencils and/or vacuum collets are the preferred method of pick up.
- Air bridges must be avoided during placement.
- Cu pillars on die are 65 um tall with a 22 um tall Sn solder cap.
- Recommended board metallization is evaporated TiW followed by nickel/gold at pillar attach interface. Ni is the adhesion layer for the solder and the gold keeps the Ni from oxidizing. The Au should be kept to a minimum to avoid embrittlement; suggested Au / Sn mass ratio must not exceed 8%.
- Au metallization is not recommended on traces due to solder wicking and consumption concerns. If Au traces are used, a physical solder barrier must be applied or designed into the pad area of the board. The barrier must be sufficient to keep the solder from undercutting the barrier.

Reflow process assembly notes:

- Minimum alloying temperatures 245 °C.
- Repeating reflow cycles is not recommended due to Sn consumption on the first reflow cycle.
- An alloy station or conveyor furnace with an inert atmosphere such as N2 should be used.
- Dip copper pillars in “no-clean flip chip” flux prior to solder attach. Suggest using a high temperature flux. Avoid exposing entire die to flux.
- If screen printing flux, use small apertures and minimize volume of flux applied.
- Coefficient of thermal expansion matching between the MMIC and the substrate/board is critical for long-term reliability.
- Devices must be stored in a dry nitrogen atmosphere.
- Suggested reflow will depend on board material and density.

Typical Reflow Profiles for TriQuint Cu / Sn Pillars

Process	Sn Reflow
Ramp-up Rate	3 °C/sec
Flux Activation Time and Temperature	60 – 120 sec @ 140 – 160 °C
Time above Melting Point (245 °C)	60 – 150 sec
Max Peak Temperature	300 °C
Time within 5 °C of Peak Temperature	10 – 20 sec
Ramp-down Rate	4 – 6 °C/sec

Ordering Information

Part	Package Style
TGC4703-FC	GaAs MMIC Die

GaAs MMIC devices are susceptible to damage from Electrostatic Discharge. Proper precautions should be observed during handling, assembly and test.

TriQuint Semiconductor: www. triquint.com (972)994-8465 Fax (972)994-8504 Info-mmw@tqs.com

TriQuint SEMICONDUCTOR

TGC4704-FC

38 to 77 GHz Doubler and Medium Power Amplifier

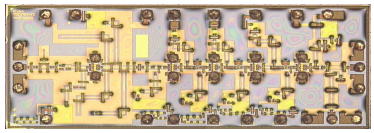

Measured Performance

Bias conditions: Vd = 4.0 V, Vg1 = -0.4 V, Vg2= 0.2 V,
Idq = 180 mA Typical

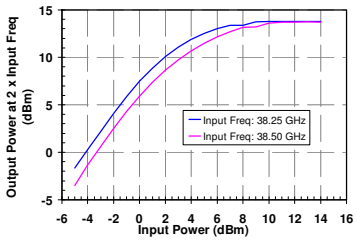

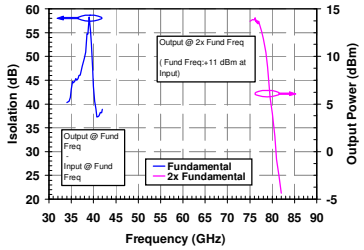

Key Features

- RF Output Frequency Range: 76–77 GHz
- Input Frequency Range: 38.0–38.5 GHz
- Two outputs – Out1 (Main) and Out2 (12 dB coupled from Out1)
- 14 dBm saturated Output Power
- 5 dB Conversion Gain
- 50 dB Input Frequency Isolation at output
- Input Return Loss > 8 dB
- Output Return Loss > 10 dB
- Bias: Vd = 3.75 V, Idq = 180 mA, Vg1 = -0.4 V Vg2 = +0.2 V Typical
- Technology: 0.13 um pHEMT with front-side Cu/Sn pillars
- Chip Dimensions: 3.38 x 1.37 x 0.38 mm

Primary Applications

- Automotive Radar
- E-Band Communication

Product Description

The TriQuint TGC4704-FC is a flip-chip frequency doubler. It combines an output medium power amplifier and a frequency doubler at frequencies in the automotive radar frequency band. The TGC4704-FC is designed using TriQuint's proven 0.13 µm pHEMT process and front-side Cu / Sn pillar technology for simplified assembly and low interconnect inductance. Die reliability is enhanced by using TriQuint's BCB polymeric passivation process.

The TGC4704-FC typically provides 14 dBm saturated output power with 5 dB conversion gain.

Lead-free and RoHS compliant.

TriQuint Semiconductor: www. triquint.com (972)994-8465 Fax (972)994-8504 Info-mmw@tqs.com

TriQuint SEMICONDUCTOR

TGC4704-FC

Table I
Absolute Maximum Ratings 1/

Symbol	Parameter	Value	Notes
Vd-Vg	Drain to Gate Voltage	5.5 V	
Vd	Drain Voltage	4.0 V	
Vg	Gate Voltage Range	-1 to + 0.45 V	
Id	Drain Current	330 mA	
Ig	Gate Current Range	-0.5 to +3.0 mA	
Pin	Input Continuous Wave Power	16 dBm	

1/ These ratings represent the maximum operable values for this device. Stresses beyond those listed under "Absolute Maximum Ratings" may cause permanent damage to the device and / or affect device lifetime. These are stress ratings only, and functional operation of the device at these conditions is not implied.

Table II
Recommended Operating Conditions

Symbol	Parameter 1/	Value
Vd	Drain Voltage	3.75 V
Idq	Drain Current, No RF signal at Input	180 mA
Id	Drain Current, RF signal at Input	240 mA
Vg1	Multiplier Stage Gate Voltage	-0.4 V
Vg2a thru Vg2d	Amplifier Stages Gate Voltage	+0.2 V

1/ See electrical schematic diagram for bias instructions.

TriQuint Semiconductor: www. triquint.com (972)994-8465 Fax (972)994-8504 Info-mmw@tqs.com

November 2009 © Rev A

TriQuint SEMICONDUCTOR

TGC4704-FC

Table III
RF Characterization Table

Bias: Vd = 3.75 V V, Idq = 180 mA, Vg1 = -0.4 V, Vg2 = +0.2 V Typical

SYMBOL	PARAMETER	TEST CONDITIONS	MINIMUM	NOMINAL	UNITS
IRL	Input Return Loss	Fin = 38.0 – 38.5 GHz		8	dB
ORL	Output Return Loss	Fin = 76.0 – 77.0 GHz		10	dB
Pout	Output Power (Pin = 8 dBm)	Fin = 38.5 GHz Fout = 77 GHz	11.5	12.5	dBm
Pout	Output Power (Pin = 10 dBm)	Fin = 38.5 GHz Fout = 77 GHz	13.0	14.0	dBm
Isol	Isolation	Fin = 38.0 – 38.5 GHz Fout = 38.0 – 38.5 GHz		50	dB

TriQuint Semiconductor: www. triquint.com (972)994-8465 Fax (972)994-8504 Info-mmw@tqs.com

TriQuint SEMICONDUCTOR

TGC4704-FC

Table IV
Power Dissipation and Thermal Properties

Parameter	Test Conditions	Value	Notes
Maximum Power Dissipation	Tbaseplate = 128.8 ℃	Pd = 1.2 W Tchannel = 150 ℃ Tm = 2.4E+7 Hrs	1/ 2/ 3/
Thermal Resistance, θjc	Vd = 4.0 V Vg1 = -0.4 V Vg2 = +0.2 V Id = 0.240 A Pd = 0.960 W Tbaseplate = 85 ℃	θjc = 17.7 (℃/W) Tchannel = 102 ℃ Tm = 9.8E+9 Hrs	3/
Mounting Temperature		Refer to Solder Reflow Profiles (pp 12)	
Storage Temperature		-65 to 150 ℃	

1/ For a median life of 2.4E+7 hours, Power Dissipation is limited to

Pd(max) = (150 ℃ – Tbase ℃)/θjc.

2/ Channel operating temperature will directly affect the device median time to failure (MTTF). For maximum life, it is recommended that channel temperatures be maintained at the lowest possible levels.

3/ For this flip-chip die, the baseplate is a plane between the Cu/Sn pillars and the test board. For the TGC4704-FC, the critical pillars for thermal power dissipation are 24 thru 33. (See Mechanical Drawing.)

Median Lifetime (Tm) vs Channel Temperature

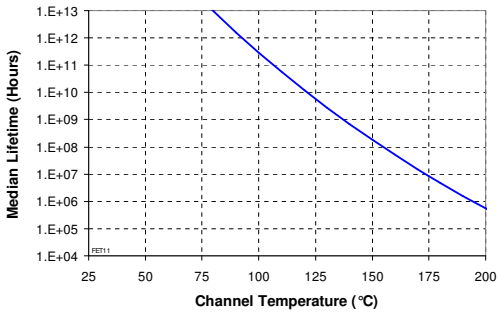

TriQuint Semiconductor: www. triquint.com (972)994-8465 Fax (972)994-8504 Info-mmw@tqs.com

TriQuint SEMICONDUCTOR

TGC4704-FC

Measured Data on Flipped Die on Carrier Board

Bias: Vd = 4.0 V, Idq = 180 mA, Vg1 = -0.4 V, Vg2 = +0.2 V Typical

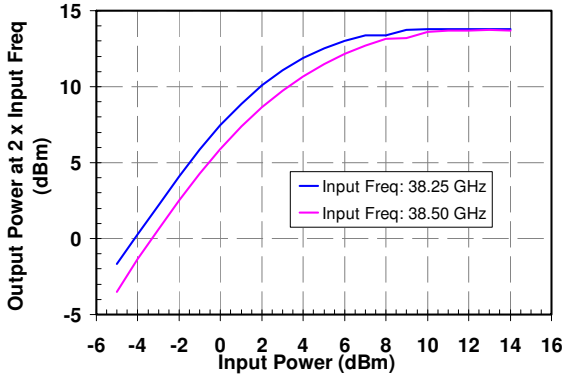

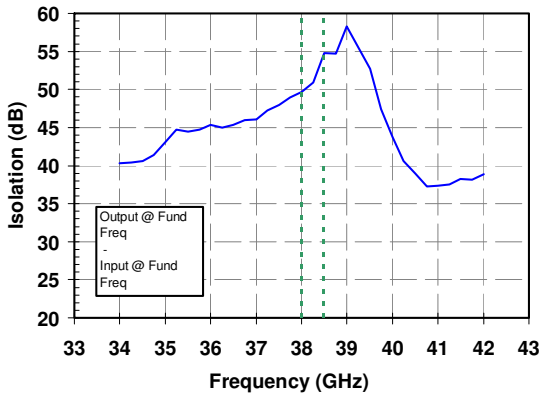

TriQuint Semiconductor: www. triquint.com (972)994-8465 Fax (972)994-8504 Info-mmw@tqs.com

TriQuint SEMICONDUCTOR

TGC4704-FC

Measured Data on Flipped Die on Carrier Board

Bias: Vd = 4.0 V, Idq = 180 mA, Vg1 = -0.4 V, Vg2 = +0.2 V Typical

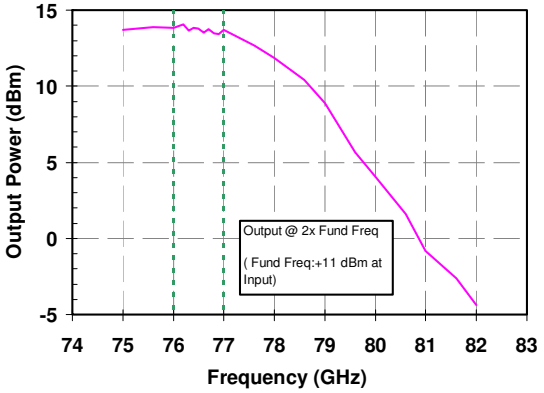

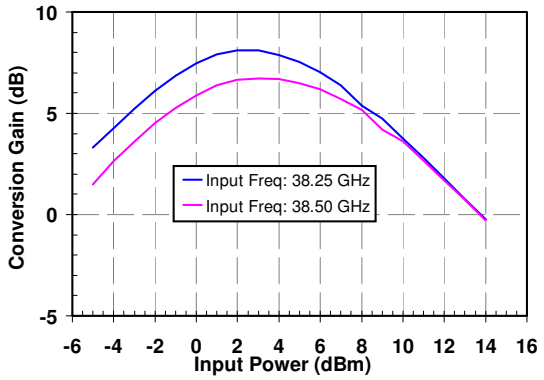

TriQuint Semiconductor: www. triquint.com (972)994-8465 Fax (972)994-8504 Info-mmw@tqs.com

TriQuint SEMICONDUCTOR

TGC4704-FC

Measured Data on Flipped Die on Carrier Board

Bias: Vd = 4.0 V, Idq = 180 mA, Vg1 = -0.4 V, Vg2 = +0.2 V Typical

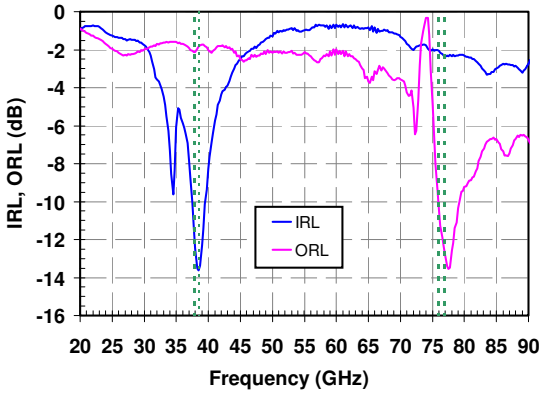

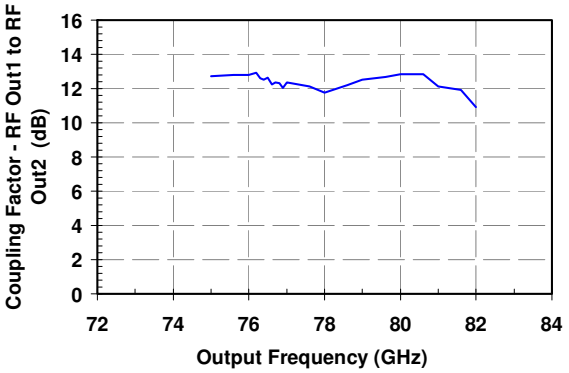

TriQuint Semiconductor: www. triquint.com (972)994-8465 Fax (972)994-8504 Info-mmw@tqs.com

TriQuint SEMICONDUCTOR

TGC4704-FC

Measured Data on Flipped Die on Carrier Board

Bias: Vd = 4.0 V, Idq = 180 mA, Vg1 = -0.4 V, Vg2 = +0.2 V Typical

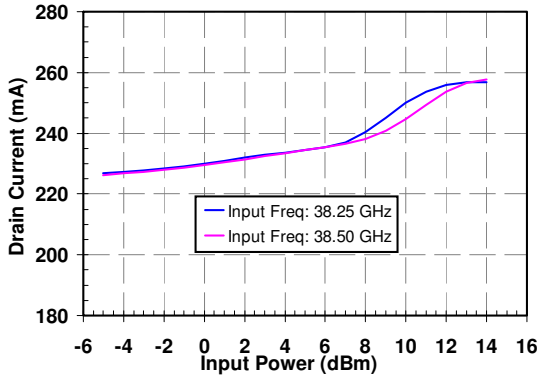

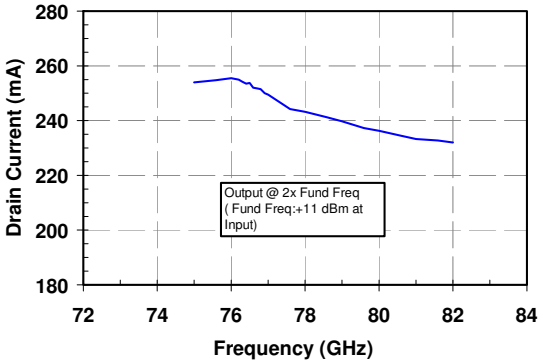

TriQuint Semiconductor: www. triquint.com (972)994-8465 Fax (972)994-8504 Info-mmw@tqs.com

TriQuint SEMICONDUCTOR

TGC4704-FC

Electrical Schematic

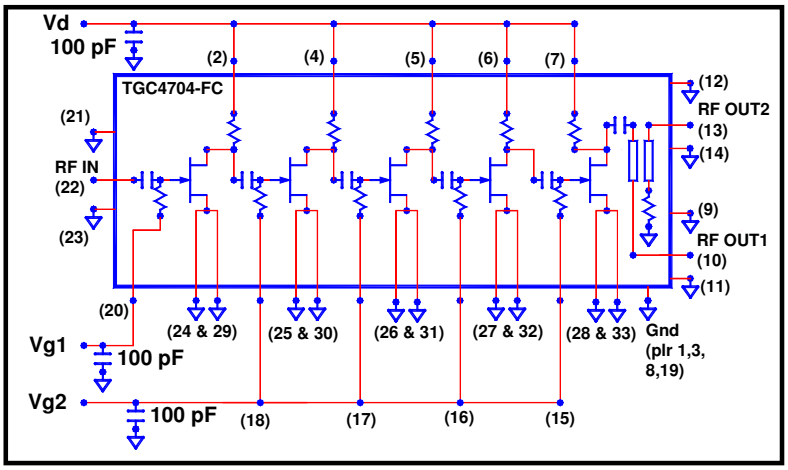

Bias Procedures

Bias-up Procedure	Bias-down Procedure
Vg1, Vg2 set to -0.4 V	Turn off RF signal to input
Vd set to +3.75 V	Reduce Vg1,2 to -0.4 V. Ensure Id ~ 0 mA
Adjust Vg2 ONLY more positive until Id is 180 mA (Vg ~ +0.2 V)	Turn Vd to 0 V
Apply RF signal to input Id will be ~240 mA	

TriQuint Semiconductor: www. triquint.com (972)994-8465 Fax (972)994-8504 Info-mmw@tqs.com

TriQuint SEMICONDUCTOR

TGC4704-FC

Mechanical Drawing

Drawing is for chip face-up

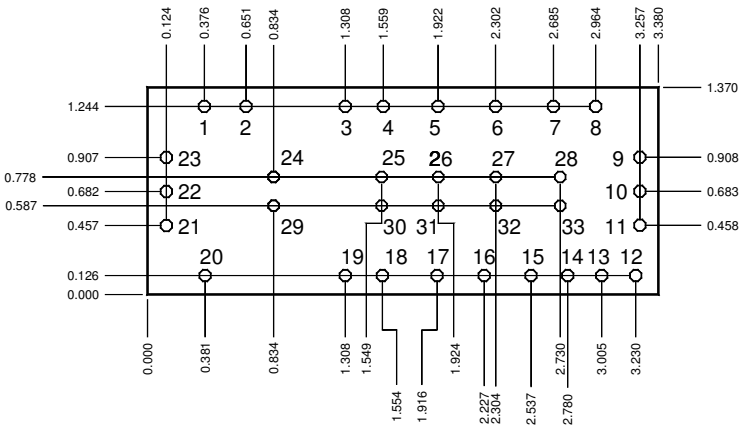

Units: millimeters Thickness: 0.380

Die x, y size tolerance +/- 0.050

Chip edge to pillar dimensions are shown to center of pillar

Pillar #22	RF In	0.075 Ø
Pillar #10	RF Out1 (Main)	0.075 Ø
Pillar #13	RF Out2 (Coupled)	0.075 Ø
Pillar #9, 11, 12, 14, 21, 23	RF CPW Ground	0.075 Ø
Pillar #20	Vg1	0.075 Ø
Pillar #18	Vg2a	0.075 Ø
Pillar #17	Vg2b	0.075 Ø
Pillar #16	Vg2c	0.075 Ø

Pillar #15	Vg2d	0.075 Ø
Pillar #2	Vd1	0.075 Ø
Pillar #4	Vd2a	0.075 Ø
Pillar #5	Vd2b	0.075 Ø
Pillar #6	Vd2c	0.075 Ø
Pillar #7	Vd2d	0.075 Ø
Pillar #1,3 8,19, 24 thru 33	DC Ground	0.075 Ø

GaAs MMIC devices are susceptible to damage from Electrostatic Discharge. Proper precautions should be observed during handling, assembly and test.

TriQuint Semiconductor: www. triquint.com (972)994-8465 Fax (972)994-8504 Info-mmw@tqs.com

TriQuint SEMICONDUCTOR

TGC4704-FC

Recommended Assembly Diagram

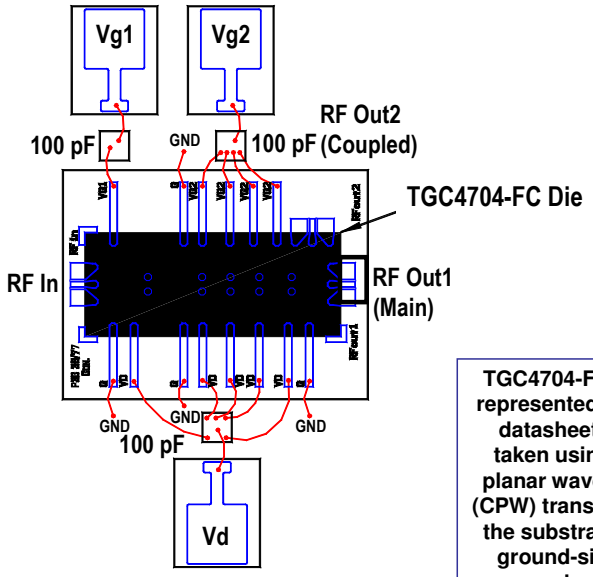

TGC4704-FC data represented in this datasheet was taken using co-planar waveguide (CPW) transition on the substrate and ground-signal-ground probes

Die is flip-chip soldered to a 15 mil thick alumina test substrate

GaAs MMIC devices are susceptible to damage from Electrostatic Discharge. Proper precautions should be observed during handling, assembly and test.

TriQuint Semiconductor: www. triquint.com (972)994-8465 Fax (972)994-8504 Info-mmw@tqs.com

TriQuint SEMICONDUCTOR

TGC4704-FC

Assembly Notes

Component placement and die attach assembly notes:

- Vacuum pencils and/or vacuum collets are the preferred method of pick up.
- Air bridges must be avoided during placement.
- Cu pillars on die are 65 um tall with a 22 um tall Sn solder cap.
- Recommended board metallization is evaporated TiW followed by nickel/gold at pillar attach interface. Ni is the adhesion layer for the solder and the gold keeps the Ni from oxidizing. The Au should be kept to a minimum to avoid embrittlement; suggested Au / Sn mass ratio must not exceed 8%.
- Au metallization is not recommended on traces due to solder wicking and consumption concerns. If Au traces are used, a physical solder barrier must be applied or designed into the pad area of the board. The barrier must be sufficient to keep the solder from undercutting the barrier.

Reflow process assembly notes:

- Minimum alloying temperatures 245 °C.
- Repeating reflow cycles is not recommended due to Sn consumption on the first reflow cycle.
- An alloy station or conveyor furnace with an inert atmosphere such as N2 should be used.
- Dip copper pillars in “no-clean flip chip” flux prior to solder attach. Suggest using a high temperature flux. Avoid exposing entire die to flux.
- If screen printing flux, use small apertures and minimize volume of flux applied.
- Coefficient of thermal expansion matching between the MMIC and the substrate/board is critical for long-term reliability.
- Devices must be stored in a dry nitrogen atmosphere.
- Suggested reflow will depend on board material and density.

Typical Reflow Profiles for TriQuint Cu / Sn Pillars

Process	Sn Reflow
Ramp-up Rate	3 °C/sec
Flux Activation Time and Temperature	60 – 120 sec @ 140 – 160 °C
Time above Melting Point (245 °C)	60 – 150 sec
Max Peak Temperature	300 °C
Time within 5 °C of Peak Temperature	10 – 20 sec
Ramp-down Rate	4 – 6 °C/sec

Ordering Information

Part	Package Style
TGC4704-FC	GaAs MMIC Die

GaAs MMIC devices are susceptible to damage from Electrostatic Discharge. Proper precautions should be observed during handling, assembly and test.

TriQuint Semiconductor: www. triquint.com (972)994-8465 Fax (972)994-8504 Info-mmw@tqs.com

Bibliography

[Aky14] I. Akyildiz, J. Jornet and C. Han, "Terahertz band: Next frontier for wireless communications.", *Physical Communication*, 09 2014.

[Alg16] A. Algaba Brazález, J. Flygare, J. Yang, V. Vassilev, M. Baquero-Escudero and P. Kildal, "Design of F-Band Transition From Microstrip to Ridge Gap Waveguide Including Monte Carlo Assembly Tolerance Analysis.", *IEEE Transactions on Microwave Theory and Techniques*, vol. 64, no. 4, pp. 1245–1254, April 2016.

[Alj17] A. Aljarosha, A. U. Zaman and R. Maaskant, "A Wideband Contactless and Bondwire-Free MMIC to Waveguide Transition.", *IEEE Microwave and Wireless Components Letters*, vol. 27, no. 5, pp. 437–439, May 2017.

[Arc81] J. W. Archer and R. J. Mattauch, "Low noise single-ended mixer for 230 GHz.", *Electronics Letters*, vol. 17, no. 5, pp. 180–181, March 1981.

[Arc84] J. W. Archer, "A Novel Quasi-Optical Frequency Multiplier Design for Millimeter and Submillimeter Wavelengths.", *IEEE Transactions on Microwave Theory and Techniques*, vol. 32, no. 4, pp. 421–427, Apr 1984.

[Ard19] Arduino, 2019. Https://store.arduino.cc/due.

[Bah88] I.J. Bahl and P. Bhartia. *Microwave solid state circuit design*. Wiley, 1988.

[Ber16] A. Berenguer, V. Fusco, D. E. Zelenchuk, D. Sánchez-Escuderos, M. Baquero-Escudero and V. E. Boria-Esbert, "Propagation Characteristics of Groove Gap Waveguide Below and Above Cutoff.", *IEEE Transactions on Microwave Theory and Techniques*, vol. 64, no. 1, pp. 27–36, Jan 2016.

[Biu15] I. Maestrojuan Biurrun. "Development of Terahertz Systems for Imaging Applications." Ph.D. thesis, Universidad Publica de Navarra, 2015.

[Bou09] B. Boukari, E. Moldovan, S. Affes, K. Wu, R. G. Bosisio and S. O. Tatu, "Robust Microstrip-to-Waveguide Transitions for Millimeter-Wave Radar Sensor Applications.", *IEEE Antennas and Wireless Propagation Letters*, vol. 8, pp. 759–762, 2009.

[Bry10] T. Bryllert, J. Vukusic, A. Ø. Olsen and J. Stake. "A broadband heterostructure barrier varactor tripler source." *2010 IEEE MTT-S International Microwave Symposium*, pp. 344–347. May 2010.

[Bul16] B. T. Bulcha, J. L. Hesler, V. Drakinskiy, J. Stake, A. Valavanis, P. Dean, L. H. Li and N. S. Barker, "Design and Characterization of 1.8–3.2 THz Schottky-Based Harmonic Mixers.", *IEEE Transactions on Terahertz Science and Technology*, vol. 6, no. 5, pp. 737–746, Sep. 2016.

[Car15] G. Carpintero, L.E. García Muñoz, H.L. Hartnagel, S. Preu and A.V. Räisänen. *Semiconductor THz Technology: Devices and Systems at Room Temperature Operation*. Wiley, 07 2015.

[Cha11] G. Chattopadhyay, "Technology, Capabilities, and Performance of Low Power Terahertz Sources.", *IEEE Transactions on Terahertz Science and Technology*, vol. 1, no. 1, pp. 33–53, Sep. 2011.

[Che04] S. Cherry. "Edholms' Law of Bandwidth.", Jul 2004. Https://spectrum.ieee.org/telecom/wireless/edholms-law-of-bandwidth.

[Cor09] R. Cory, "Schottky Diodes.", *Skyworks Solutions*, 2009.

[Cru07] F. C. Cruz, G. T. Nogueira, L. F. L. Costa, N. C. Frateschi, R. C. Viscovini and D. Pereira. "Continuous and Pulsed THz generation with

molecular gas lasers and photoconductive antennas gated by femtosecond pulses." *2007 SBMO/IEEE MTT-S International Microwave and Optoelectronics Conference*, pp. 446–449. Oct 2007.

[Den18] J. Deng, Q. Lu, D. Jia, Y. Yang and Z. Zhu, "Wideband Fourth-Harmonic Mixer Operated at 325–500 GHz.", *IEEE Microwave and Wireless Components Letters*, vol. 28, no. 3, pp. 242–244, March 2018.

[Des10] D. Deslandes. "Design equations for tapered microstrip-to-Substrate Integrated Waveguide transitions." *2010 IEEE MTT-S International Microwave Symposium*, pp. 1–1. May 2010.

[Dra13] V. Drakinskiy, P. Sobis, H. Zhao, T. Bryllert and J. Stake. "Terahertz GaAs Schottky diode mixer and multiplier MIC's based on e-beam technology." *Conference Proceedings - International Conference on Indium Phosphide and Related Materials*, pp. 1–2. 05 2013.

[Duc14] G. Ducournau, P. Szriftgiser, A. Beck, D. Bacquet, F. Pavanello, E. Peytavit, M. Zaknoune, T. Akalin and J. Lampin, "Ultrawide-Bandwidth Single-Channel 0.4-THz Wireless Link Combining Broadband Quasi-Optic Photomixer and Coherent Detection.", *IEEE Transactions on Terahertz Science and Technology*, vol. 4, no. 3, pp. 328–337, May 2014.

[Duc15] G. Ducournau, P. Szriftgiser, F. Pavanello, E. Peytavit, M. Zaknoune, D. Bacquet, A. Beck, T. Akalin and J.F. Lampin, "THz Communications using Photonics and Electronic Devices: the Race to Data-Rate.", *Journal of Infrared, Millimeter, and Terahertz Waves*, vol. 36, no. 2, pp. 198–220, Feb 2015.

[Ede07] I. Ederra, L. Azcona, B. E. J. Alderman, A. Laisne, R. Gonzalo, C. M. Mann, D. N. Matheson and P. de Maagt, "A 250 GHz Subharmonic Mixer Design Using EBG Technology.", *IEEE Transactions on Antennas and Propagation*, vol. 55, no. 11, pp. 2974–2982, Nov 2007.

[Eis10] H. Eisele, "State of the art and future of electronic sources at terahertz frequencies.", *Electronics Letters*, vol. 46, no. 26, pp. s8–s11, December 2010.

[Eme18] Emerson and Cuming, 2018. Http://trimcom.ru/pdf/WAVASORB-VHP.pdf.

[Eri85] N. R. Erickson, "A Very Low-Noise Single-Sideband Receiver for 200-260 GHz.", *IEEE Transactions on Microwave Theory and Techniques*, vol. 33, no. 11, pp. 1179–1188, Nov 1985.

[Esh05] I. A. Eshrah, A. A. Kishk, A. B. Yakovlev and A. W. Glisson, "Rectangular waveguide with dielectric-filled corrugations supporting backward waves.", *IEEE Transactions on Microwave Theory and Techniques*, vol. 53, no. 11, pp. 3298–3304, Nov 2005.

[Fai94] J. Faist, F. Capasso, D.L. Sivco, C. Sirtori, A. L. Hutchinson and A.Y. Cho, "Quantum Cascade Laser.", *Science*, vol. 264, no. 5158, pp. 553–556, 1994.

[Fed10] J. Federici and L. Moeller, "Review of terahertz and subterahertz wireless communications.", *Journal of Applied Physics*, vol. 107, no. 11, p. 111101, 2010.

[Fol05] F. Folster, H. Rohling and U. Lubbert. "An automotive radar network based on 77 GHz FMCW sensors." *IEEE International Radar Conference, 2005.*, pp. 871–876. May 2005.

[Fuj15] Fujitsu, 2015. Https://www.fujitsu.com/global/about/resources/news/press-releases/2015/0908-02.html.

[Gra17] A. B. Granja, R. Jakoby and A. Penirschke. "Outright W-Band chebyshev-based hollow waveguide to microstrip transition." *2017 42nd International Conference on Infrared, Millimeter, and Terahertz Waves (IRMMW-THz)*, pp. 1–2. Aug 2017.

[Guo18] C. Guo and et al., "A 290–310 GHz Single Sideband Mixer With Integrated Waveguide Filters.", *IEEE Trans. Terahertz Sci. Technol.*, vol. 8, no. 4, pp. 446–454, 2018.

[Has12] J. Hasch, E. Topak, R. Schnabel, T. Zwick, R. Weigel and C. Waldschmidt, "Millimeter-Wave Technology for Automotive Radar Sensors in the 77 GHz Frequency Band.", *IEEE Transactions on Microwave Theory and Techniques*, vol. 60, no. 3, pp. 845–860, March 2012.

[Hea98] D. J. T. Heatley, D. R. Wisely, I. Neild and P. Cochrane, "Optical wireless: the story so far.", *IEEE Communications Magazine*, vol. 36, no. 12, pp. 72–74, Dec 1998.

[HI07] T. Ishibashi H. Ito, T. Nagatsuma. "Uni-traveling carrier photodiodes for high-speed detection and broadband sensing." *Proceedings of SPIE - The International Society for Optical Engineering*, vol. 6479. 2007.

[Hir06] A. Hirata, T. Kosugi, H. Takahashi, R. Yamaguchi, F. Nakajima, T. Furuta, H. Ito, H. Sugahara, Y. Sato and T. Nagatsuma, "120-GHz-band millimeter-wave photonic wireless link for 10-Gb/s data transmission.", *IEEE Transactions on Microwave Theory and Techniques*, vol. 54, no. 5, pp. 1937–1944, May 2006.

[J. 16] J. He, G. Hu, Z. Zhou, G. Ma, Y. He, M. Chan and L. Song. "Study progess on FET-based Terahertz wave generation and detection." *2016 13th IEEE International Conference on Solid-State and Integrated Circuit Technology (ICSICT)*, pp. 161–164. Oct 2016.

[Jia17] D. Jiangqiao, A. Maestrini, L. Gatilova, A. Cavanna, S. Shi and W. Wu, "High Efficiency and Wideband 300 GHz Frequency Doubler Based on Six Schottky Diodes.", *Journal of Infrared, Millimeter, and Terahertz Waves*, vol. 38, no. 11, pp. 1331–1341, Nov 2017.

[Jia18] S. Jia, X. Pang, O. Ozolins, X. Yu, H. Hu, J. Yu, P. Guan, F. Da Ros, S. Popov, G. Jacobsen, M. Galili, T. Morioka, D. Zibar and L. K. Oxenløwe, "0.4 THz Photonic-Wireless Link With 106 Gb/s Single Channel Bitrate.", *Journal of Lightwave Technology*, vol. 36, no. 2, pp. 610–616, Jan 2018.

[JK09] C. Jung-Kubiak, A. Maestrini, A. Cavanna, U. Gennser, I. Sagnes, H. Wang and Y. Jin, "Conception and Fabrication of GaAs Schottky Diodes for Mixers.", *20th International Symposium on Space Terahertz Technology, Charlottesville, 20-22 April 2009*, 04 2009.

[Kan99] N. Kaneda, Y. Qian and T. Itoh, "A broad-band microstrip-to-waveguide transition using quasi-Yagi antenna.", *IEEE Transactions on Microwave Theory and Techniques*, vol. 47, no. 12, pp. 2562–2567, Dec 1999.

[Koc07] M. Koch. "Terahertz Communications: A 2020 vision." Robert E. Miles, Xi-Cheng Zhang, Heribert Eisele and Arunas Krotkus, eds., *Terahertz Frequency Detection and Identification of Materials and Objects*, pp. 325–338. Springer Netherlands, Dordrecht, 2007.

[Kol89] E. Kollberg and A. Rydberg, "Quantum-barrier-varactor diodes for high-efficiency millimetre-wave multipliers.", *Electronics Letters*, vol. 25, no. 25, pp. 1696–1698, Dec 1989.

[Leo99] Y.C Leong and S. Weinreb. "Full band waveguide-to-microstrip probe transitions." *1999 IEEE MTT-S International Microwave Symposium Digest (Cat. No.99CH36282)*, vol. 4, pp. 1435–1438 vol.4. June 1999.

[Li13] S. Li, T. Gui-Xiang and Chih Niu D., "Full W-Band Waveguide-to-Microstrip Transition With New E-Plane Probe.", *Microwave and Wireless Components Letters, IEEE*, vol. 23, pp. 4–6, 01 2013.

[Li16] Q. Li, B. Zhang, L. Zhang, D. Xing, J. Wang and Y. Fan. "A 330–500GHz 4th-harmonic mixer using schottiky diode." *2016 IEEE MTT-S International Microwave Workshop Series on Advanced Materials and Processes for RF and THz Applications (IMWS-AMP)*, pp. 1–3. July 2016.

[Li18] J. Li, L. Li, Y. Qiao, J. Chen and A. Zhang, "Full Ka Band Waveguide-to-Microstrip Inline Transition Design.", *Journal of Infrared, Millimeter, and Terahertz Waves*, vol. 39, no. 8, pp. 714–722, Aug 2018.

[Lin16] E. H. Linfield, A. Valavanis, Y. J. Han, L. H. Li, J. X. Zhu, R. Dong, P. Dean, A. G. Davies, N. Brewster, L. Bushnell, M. Oldfield and B. N. Ellison. "Terahertz frequency quantum cascade lasers for use as waveguide-integrated local oscillators." *2016 10th European Conference on Antennas and Propagation (EuCAP)*, pp. 1–3. April 2016.

[Lyn08] J. J. Lynch, H. P. Moyer, J. H. Schaffner, Y. Royter, M. Sokolich, B. Hughes, Y. J. Yoon and J. N. Schulman, "Passive Millimeter-Wave Imaging Module With Preamplified Zero-Bias Detection.", *IEEE Transactions on Microwave Theory and Techniques*, vol. 56, no. 7, pp. 1592–1600, July 2008.

[Maa03] S.A. Maas. *Nonlinear Microwave and RF Circuits*. Artech House, 2003.

[Mae10] A. Maestrini, B. Thomas, H. Wang, C. Jung, J. Treuttel, Y. Jin, G. Chattopadhyay, I. Mehdi and G. Beaudin, "Schottky diode-based terahertz frequency multipliers and mixers.", *Comptes Rendus Physique*, vol. 11, no. 7, pp. 480 – 495, 2010.

[Mae14a] I. Maestrojuan, I. Ederra and R. Gonzalo. "Comparison of a subharmonic and a fourth-harmonic mixer working at 440 GHz." *2014 39th International Conference on Infrared, Millimeter, and Terahertz waves (IRMMW-THz)*, pp. 1–2. Sep. 2014.

[Mae14b] I. Maestrojuan, I. Palacios, I. Ederra and R. Gonzalo, "USE of COC substrates for millimeter-wave devices.", *Microwave and Optical Technology Letters*, vol. 57, no. 2, pp. 371–377, 2014.

[Mae14c] I. Maestrojuan, S. Rea, R. Gonzalo and I. Ederra, "Experimental analysis of different measurement techniques for characterization of millimeter-wave mixers.", *Microw. Opt. Tech. Lett.*, pp. 1441–1447, 2014.

[Mae15] I. Maestrojuan, I. Ederra and R. Gonzalo, "Fourth-Harmonic Schottky Diode Mixer Development at Sub-Millimeter Frequencies.", *IEEE Transactions on Terahertz Science and Technology*, vol. 5, no. 3, pp. 518–520, May 2015.

[Meh98] I. Mehdi, S. M. Marazita, D. A. Humphrey, , R. J. Dengler, J. E. Oswald, A. J. Pease, S. C. Martin, W. L. Bishop, T. W. Crowe and P. H. Siegel, "Improved 240-GHz subharmonically pumped planar Schottky diode mixers for space-borne applications.", *IEEE Transactions on Microwave Theory and Techniques*, vol. 46, no. 12, pp. 2036–2042, Dec 1998.

[Meh17] I. Mehdi, J. V. Siles, C. Lee and E. Schlecht, "THz Diode Technology: Status, Prospects, and Applications.", *Proceedings of the IEEE*, vol. 105, no. 6, pp. 990–1007, June 2017.

[Mic13] S. Michaelsen, T. Johansen and V. Krozer. "Design of a x4 subharmonic sub-millimeter wave diode mixer, based on an analytic expression for small-signal conversion admittance parameters." *2013 Microwave and Optoelectronics Conference (IMOC). IEEE, 2013.*, pp. 1–4. 08 2013.

[Mim05] T. Mimura, "Development of High Electron Mobility Transistor.", *Japanese Journal of Applied Physics*, vol. 44, pp. 8263–8268, 12 2005.

[Nag11] T. Nagatsuma, "Terahertz technologies: present and future.", *IEICE Electronic Express*, vol. 8, pp. 1127–1142, 2011.

[Nag13] T. Nagatsuma, S. Horiguchi, Y. Minamikata, Y. Yoshimizu, S. Hisatake, S. Kuwano, N. Yoshimoto, J. Terada and H. Takahashi, "Terahertz wireless communications based on photonics technologies.", *Opt. Express*, vol. 21, no. 20, pp. 23736–23747, Oct 2013.

[Nag16] T. Nagatsuma, G. Ducournau and Ciryl C. Renaud, "Advances in terahertz communications accelarated by photonics.", *Nature Photonics*, vol. 10, pp. 371 – 379, 2016.

[Neo19] NeoTech, 2019. Http://www.myneotech.com/products/gamp0100-0600sm10/.

[Orf13] S.J. Orfanidis. *Electromagnetic Waves and Antennas*. http://eceweb1.rutgers.edu/ orfanidi/ewa/., 2013.

[Pé16] J. M. Pérez, A. Rebollo, R. Gonzalo and I. Ederra. "An inline microstrip-to-waveguide transition operating in the full W-Band based on a Chebyshev multisection transformer." *2016 10th European Conference on Antennas and Propagation (EuCAP)*, pp. 1–4. April 2016.

[Pé18] J.M. Pérez- Escudero, A. Torres-Garcia, R. Gonzalo and I. Ederra, "A Simplified Design Inline Microstrip-to-Waveguide Transition.", *Electronics*, vol. 7, no. 10, p. 215, Sep 2018.

[Pag85] L. Pagani, G. Beaudin, M. Gheudin, A. Deschamp and P. Encrenaz. "A 230GHz Low Noise Cooled Receiver for Radioastronomy Applications." *1985 15th European Microwave Conference*, pp. 291–296. Sep. 1985.

[Pan15] B. Panzner. "In-band wireless backhaul for 5G millimeter wave cellular communications - interactive live demo." *2015 IEEE Conference on Computer Communications Workshops*, pp. 21–22. April 2015.

[PG86] N.R. Erickson P.F. Goldsmith. "Waveguide Submillimeter Mixers." *1985 International Technical Symposium-Europe*, vol. 0598. 1986.

[Poz04] D.M. Pozar. *Microwave Engineering*. Wiley, 2004.

[Rä80] A. Räisänen, "Experimental studies on cooled millimeter wave mixers.", *Acta Polytechnica Scandinavica 46*, 1980.

[Rai80] A. V. Raisanen, C. R. Predmore, P. T. Parrish, P. F. Goldsmith, J. L. R. Marrero, R. A. Kot and M. V. Schneider. "A Cooled Schottky-Diode Mixer for 75-120 GHz." *1980 10th European Microwave Conference*, pp. 717–721. Sep. 1980.

[Rai92] A. V. Raisanen, "Frequency multipliers for millimeter and submillimeter wavelengths.", *Proceedings of the IEEE*, vol. 80, no. 11, pp. 1842–1852, Nov 1992.

[Raj10] E. Rajo- Iglesias, A. Zaman and P.S. Kildal, "Parallel Plate Cavity Mode Suppression in Microstrip Circuit Packages Using a Lid of Nails.", *Microwave and Wireless Components Letters, IEEE*, vol. 20, pp. 31 – 33, 02 2010.

[Raj11] E. Rajo- Iglesias and P.S. Kildal, "Numerical studies of bandwidth of parallel-plate cut-off realised by a bed of nails, corrugations and mushroom-type electromagnetic bandgap for use in gap waveguides.", *Microwaves, Antennas and Propagation, IET*, vol. 5, pp. 282 – 289, 03 2011.

[Raj13] E. Rajo- Iglesias, E. Pucci, A. Kishk and P.S. Kildal, "Suppression of Parallel Plate Modes in Low Frequency Microstrip Circuit Packages Using Lid of Printed Zigzag Wires.", *Microwave and Wireless Components Letters, IEEE*, vol. 23, pp. 359–361, 07 2013.

[Raz13] H. Raza, J. Yang, P. Kildal and E. Alfonso, "Resemblance between gap waveguides and hollow waveguides.", *IET Microwaves, Antennas Propagation*, vol. 7, no. 15, pp. 1221–1227, December 2013.

[Reb11] A. Rebollo, I. Maestrojuan, R. Gonzalo and I. Ederra, "A broadband radiometer configuration at 94GHz in planar technology.", *2011 IEEE MTT-S International Microwave Workshop Series on Millimeter Wave Integration Technologies*, pp. 89–92, 2011.

[Reb14] A. Rebollo, R. Gonzalo and I. Ederra, "Optimization of a Pin Surface as a Solution to Suppress Cavity Modes in a Packaged W-Band Microstrip Receiver.", *IEEE Transactions on Components, Packaging and Manufacturing Technology*, vol. 4, no. 6, pp. 975–982, June 2014.

[Reb15] A. Rebollo, R. Gonzalo and I. Ederra, "An Inline Microstrip-to-Waveguide Transition Operating in the Full W-Band.", *Journal of*

Infrared, Millimeter, and Terahertz Waves, vol. 36, no. 8, pp. 734–744, Aug 2015.

[Rec15] T. Reck, C. Jung-Kubiak, J. V. Siles, C. Lee, R. Lin, G. Chattopadhyay, I. Mehdi and K. Cooper, "A Silicon Micromachined Eight-Pixel Transceiver Array for Submillimeter-Wave Radar.", *IEEE Transactions on Terahertz Science and Technology*, vol. 5, no. 2, pp. 197–206, March 2015.

[Rie14] J. Rieh, D. Yoon and J. Yun. "An overview of solid-state electronic sources and detectors for Terahertz imaging." *2014 12th IEEE International Conference on Solid-State and Integrated Circuit Technology (ICSICT)*, pp. 1–4. Oct 2014.

[Rod18] P. Rodríguez- Vázquez, J. Grzyb, N. Sarmah, B. Heinemann and U. R. Pfeiffer. "Towards 100 Gbps: A Fully Electronic 90 Gbps One Meter Wireless Link at 230 GHz." *2018 48th European Microwave Conference (EuMC)*, pp. 1389–1392. Sep. 2018.

[Roh12] Rohde and Schwarz, "The Y Factor Technique for Noise Figure Measurements.", *Applicat. Note 1MA178-1E*, 07 2012.

[Rou12] E. Rouvalis, M. Chtioui, M. Tran, F. Lelarge, F. van Dijk, M. J. Fice, C. C. Renaud, G. Carpintero and A. J. Seeds, "High-speed photodiodes for InP-based photonic integrated circuits.", *Opt. Express*, vol. 20, no. 8, pp. 9172–9177, Apr 2012.

[Row10] S. Rownak, S. Suemii and W. Prathe, "W-Band Microstrip-to-Waveguide Transition Using via Fences.", *Progress In Electromagnetics Research Letters*, vol. 16, pp. 151–160, 01 2010.

[Sch18a] B. Scheiner, S. Mann, F. Lurz, F. Michler, S. Erhardt, S. Lindner, R. Weigel and A. Koelpin. "Microstrip-to-waveguide transition in planar form using a substrate integrated waveguide." *2018 IEEE Radio and Wireless Symposium (RWS)*, pp. 18–20. Jan 2018.

[Sch18b] M. Schroter and A. Pawlak. "SiGe heterojunction bipolar transistor technology for sub-mm-wave electronics — state-of-the-art and future prospects." *2018 IEEE 18th Topical Meeting on Silicon Monolithic Integrated Circuits in RF Systems (SiRF)*, pp. 60–63. Jan 2018.

[Sha17] H. Shams, L. Gonzalez-Guerrero, M. Fice, Z. Yang, C. Renaud and A. Seeds. "Distribution of multiband THz wireless signals over fiber." *SPIE OPTO, 2017, San Francisco, California, United States*, p. 101280G. 01 2017.

[She01] D. M. Sheen, D. L. McMakin and T. E. Hall, "Three-dimensional millimeter-wave imaging for concealed weapon detection.", *IEEE Transactions on Microwave Theory and Techniques*, vol. 49, no. 9, pp. 1581–1592, Sep. 2001.

[Shi17] Y. Shi, M. Zhou and J. Zhang, "Parallel Plate Mode Suppression in Low-Frequency Microwave Circuit Packages Using Lid of 3-D Cross by a 3-D Printing Technique.", *IEEE Transactions on Electromagnetic Compatibility*, vol. 59, no. 4, pp. 1268–1271, Aug 2017.

[Shi18] Y. Shi, J. Zhang, S. Zeng and M. Zhou, "Novel$W$-Band Millimeter-Wave Transition From Microstrip Line to Groove Gap Waveguide for MMIC Integration and Antenna Application.", *IEEE Transactions on Antennas and Propagation*, vol. 66, no. 6, pp. 3172–3176, June 2018.

[Sim18] M. Simone, A. Fanti, G. Valente, G. Montisci, R. Ghiani and G. Mazzarella, "A Compact In-Line Waveguide-to-Microstrip Transition in the Q-Band for Radio Astronomy Applications.", *Electronics*, vol. 7, no. 2, p. 24, Feb 2018.

[Sob11a] P. Sobis. "Advanced Schottky Diode Receiver Front-Ends for Terahertz Applications." Ph.D. thesis, Chalmers University of Technology, 2011.

[Sob11b] P. J. Sobis, A. Emrich and J. Stake, "A Low VSWR 2SB Schottky Receiver.", *IEEE Trans. Terahertz Sci. Technol.*, vol. 1, no. 2, pp. 403–411, 2011.

[Son11] H. Song and T. Nagatsuma, "Present and Future of Terahertz Communications.", *IEEE Transactions on Terahertz Science and Technology*, vol. 1, no. 1, pp. 256–263, Sep. 2011.

[Son15] H.J. Song and T. Nagatsuma. *Handbook of Terahertz Technologies: Devices and Applications*. Pan Stanford Publishing, 2015.

[Sys11] Advanced Design System, 2011. ADS Load Pull DesignGuide.

[Tak78] T. Takada and M. Hirayama, "Hybrid Integrated Frequency Multipliers at 300 and 450 GHz.", *IEEE Transactions on Microwave Theory and Techniques*, vol. 26, no. 10, pp. 733–737, Oct 1978.

[Tec14] Agilent Technologies, "Noise Figure Measurement Accuracy- The Y Factor Method.", *Applicat. Note 57-2*, 02 2014.

[Tho05] B. Thomas, A. Maestrini and G. Beaudin, "A low-noise fixed-tuned 300-360-GHz sub-harmonic mixer using planar Schottky diodes.", *IEEE Microwave and Wireless Components Letters*, vol. 15, no. 12, pp. 865–867, Dec 2005.

[Tho08a] B. Thomas, B. Alderman, D. Matheson and P. de Maagt, "A Combined 380 GHz Mixer/Doubler Circuit Based on Planar Schottky Diodes.", *IEEE Microwave and Wireless Components Letters*, vol. 18, no. 5, pp. 353–355, May 2008.

[Tho08b] B. Thomas, S. Rea, B. Moyna and D. Matheson, "Development of a 340-GHz Sub-Harmonic Image Rejection Mixer Using Planar Schottky Diodes.", *19th Symposium on Space Terahertz Technology*, 2008.

[Tho09] B. Thomas, S. Rea, B. Moyna, B. Alderman and D. Matheson, "A 320–360 GHz Subharmonically Pumped Image Rejection Mixer Using Planar Schottky Diodes.", *IEEE Microwave and Wireless Components Letters*, vol. 19, no. 2, pp. 101–103, Feb 2009.

[Tho10a] B. Thomas, C. Lee, A. Peralta, J. Gill, G. Chattopadhyay, S. Sin, R. Lin and I. Mehdi, "A 530-600 GHz Silicon Micro-machined Integrated Receiver Using GaAs MMIC Membrane Planar Schottky Diodes.", *21ST International Symposium on Space Terahertz Technology, Oxford (ISSTT), 23-25 March, 2010*, 03 2010.

[Tho10b] B. Thomas, A. Maestrini, J. Gill, C. Lee, R. Lin, I. Mehdi and P. de Maagt, "A Broadband 835–900-GHz Fundamental Balanced Mixer Based on Monolithic GaAs Membrane Schottky Diodes.", *IEEE Transactions on Microwave Theory and Techniques*, vol. 58, no. 7, pp. 1917–1924, July 2010.

[Tho12] B. Thomas, A. Walber, J. Treuttel, R. Henneberger and B. Alderman. "W-band balanced frequency tripler using a novel coupled lines biasing scheme compatible with flip-chip mounting." *23rd ISSTT*. 2012.

[Tor17] A. E. Torres-García, I. Ederra and R. Gonzalo. "Implementation of a THz quasi-spiral antenna for THz-IR detector." *2017 11th European Conference on Antennas and Propagation (EUCAP)*, pp. 2526–2529. March 2017.

[Tre10] J. Treuttel, A. Maestrini, B. Alderman, H. Wang, D. Matheson and P. De Maagt, "Design of a combined tripler-subharmonic mixer at 330 GHz for multipixel application using European Schottky diodes.", *21TH ISSTT, Oxford, April 2010*, 03 2010.

[Tri19] Triquint, 2019. Https://www.qorvo.com/applications/automotive.

[UMS19] UMS, 2019. Https://www.ums-gaas.com/foundry/technologies/.

[Urt17] M. Urteaga, Z. Griffith, M. Seo, J. Hacker and M. J. W. Rodwell, "InP HBT Technologies for THz Integrated Circuits.", *Proceedings of the IEEE*, vol. 105, no. 6, pp. 1051–1067, June 2017.

[Wan08] H. Wang, B. Thomas, B. Alderman, A. Maestrini and G. Beaudin. "Development of a Two-Pixel Integrated Heterodyne Schottky Diode Receiver at 183GHz." *9th International Symposium on Space Terahertz Technology*. April 2008.

[Wan09] H. Wang. "Conception et modélisation de circuits monolithiques à diode Schottky sur substrat GaAs aux longueurs d'onde millimétriques et submillimétriques pour des récepteurs hétérodynes multi-pixels embarqués sur satellites et dédiés à l'aéronomie ou la planétologie." Ph.D. thesis, Université Pierre Et Marie Curie, 05 2009.

[War04] J. Ward, E. Schlecht, G. Chattopadhyay, A. Maestrini, J. Gill, F. Maiwald, H. Javadi and I. Mehdi. "Capability of THz sources based on Schottky diode frequency multiplier chains." *2004 IEEE MTT-S International Microwave Symposium Digest*, vol. 3, pp. 1587–1590 Vol.3. June 2004.

[Woo03] R.M. Woodward, R. Wallace, D. Arnone, E. Linfield and M. Pepper, "Terahertz Pulsed Imaging of Skin Cancer in the Time and Frequency Domain.", *Journal of biological physics*, vol. 29, pp. 257–9, 06 2003.

[Xia16] Y. Xianbin, J. Shi, H. Hao, M. Galili, T. Morioka, P. Jepsen and L.K. Oxenlowe, "160 Gbit/s photonics wireless transmission in the 300-500 GHz band.", *APL Photonics*, vol. 1, 11 2016.

[Yan10] M. H. Yang, J. Xu, Q. Zhao, G. P. Li and L. Peng. "Compact, broadband waveguide-to-microstrip transition using slotline antenna." *2010 International Conference on Microwave and Millimeter Wave Technology*, pp. 744–747. May 2010.

[Yan11] Y. Yang, A. Shutler and D. Grischkowsky, "Measurement of the transmission of the atmosphere from 0.2 to 2 THz.", *Optics express*, vol. 19, pp. 8830–8, 04 2011.

[Yao94] Yao, A. Abdelmonem and K. A. Zaki, "Analysis and design of microstrip-to-waveguide transitions.", *IEEE Transactions on Microwave Theory and Techniques*, vol. 42, no. 12, pp. 2371–2380, Dec 1994.

[Yuj03] L. Yujiri, M. Shoucri and P. Moffa, "Passive millimeter wave imaging.", *IEEE Microwave Magazine*, vol. 4, no. 3, pp. 39–50, Sep. 2003.

[Zam14] A. U. Zaman, M. Alexanderson, T. Vukusic and P. Kildal, "Gap Waveguide PMC Packaging for Improved Isolation of Circuit Components in High-Frequency Microwave Modules.", *IEEE Transactions on Components, Packaging and Manufacturing Technology*, vol. 4, no. 1, pp. 16–25, Jan 2014.

[Zam16] A. U. Zaman, V. Vassilev, P. Kildal and H. Zirath, "Millimeter Wave E-Plane Transition From Waveguide to Microstrip Line With Large Substrate Size Related to MMIC Integration.", *IEEE Microwave and Wireless Components Letters*, vol. 26, no. 7, pp. 481–483, July 2016.

[Zam17] A. U. Zaman, V. Vassilev, H. Zirath and N. Rorsman, "Novel Low-Loss Millimeter-Wave Transition From Waveguide-to-Microstrip Line Suitable for MMIC Integration and Packaging.", *IEEE Microwave and Wireless Components Letters*, vol. 27, no. 12, pp. 1098–1100, Dec 2017.

[Zha10] Y. Zhang, J. A. Ruiz-Cruz, K. A. Zaki and A. J. Piloto, "A Waveguide to Microstrip Inline Transition With Very Simple Modular Assembly.", *IEEE Microwave and Wireless Components Letters*, vol. 20, no. 9, pp. 480–482, Sep. 2010.

[Zha11] H. Zhao. "Modelling and Characterisation of a Broadband 85 / 170 GHz Schottky Varactor Frequency Doubler." Ph.D. thesis, Chalmers University of Technology, 2011.

[Zha12] H. Zhao, V. Drakinskiy, P. Sobis, J. Hanning, T. Bryllert, and J. Stake. "Development of a 557 GHz GaAs monolithic membrane-diode mixer." *2012 International Conference on Indium Phosphide and Related Materials*, pp. 102–105. Aug 2012.

[Zha16] Y. Zhang, W. Zhao, Y. Wang, T. Ren and Y. Chen, "A 220 GH z subharmonic mixer based on schottky diodes with an accurate terahertz diode model.", *Microwave and Optical Technology Letters*, vol. 58, pp. 2311–2316, 10 2016.

Author's merit

Scientific production of this Thesis

Journal Papers

Generated by this Thesis:

1. **José M. Pérez Escudero**, Alicia E. Torres, Ramón Gonzalo, Iñigo Ederra. "A simplified design inline microstrip to waveguide transition". Electronics 7(10) 215, 2018.

2. **José M. Pérez Escudero**, Alicia E. Torres, Ramón Gonzalo, Iñigo Ederra. "A Chebyshev Transformer Based Microstrip to Groove Gap Waveguide Inline Transition for MMIC Packaging". IEEE Transactions on Components, Packaging and Manufacturing Technology, 2019.

3. Ali M,**Pérez-Escudero J.M.**, Guzmán-Martínez R-C, Lo M-C, Ederra I, Gonzalo R, García-Muñoz LE, Santamaría G, Segovia-Vargas D, van Dijk F, Carpintero G. "300 GHz Optoelectronic Transmitter Combining Integrated Photonics and Electronic Multipliers for Wireless Communication". Photonics. 2019; 6(2):35.

4. **José M. Pérez-Escudero**, Carlos Quemada, Ramón Gonzalo, Iñigo Ederra. "A 300 GHz Combined Doubler/Subharmonic Mixer Based on Schottky Diodes With Integrated MMIC based Local Oscillator". Submitted to Journal of Infrared Millimeter and Terahertz Waves .

Additional Publication:

1. **José M. Pérez Escudero**,Eduardo Jarauta, Francisco Falcone, Miguel Beruete. "Response of complementary split ring resonators in composite stratified substrate integrated waveguide". Journal of Applied Physics 121(19), 2017.

2. Alicia Torres-Garcia, **José M. Pérez Escudero**, Ramón Gonzalo, Iñigo Ederra. "Modified Soret Lenses for Dual-Band Integrated Detectors at Millimeter and Submillimeter Wavelengths". Submitted to IEEE Transaction on Terahertz Science and Technology.

International Conferences

Generated by this Thesis:

1. **José M. Pérez Escudero**, Ainara Rebollo, Ramón Gonzalo, Iñigo Ederra. "An inline microstrip to waveguide transition operating in the full W-Band based on Chebyshev multisection transformer". 10th European Conference on Antennas and Propagation, EuCAP 2016.

2. **José M. Pérez Escudero**, Ramón Gonzalo, Iñigo Ederra. "Design of electronic subsystem for a 300 GHz wireless communication system". 11th European Conference on Antennas and Propagation, EuCAP 2017.

3. **José M. Pérez Escudero**, Ramón Gonzalo, Iñigo Ederra. "Development of Electronic Subsystems for a Terahertz Wireless Link". 10th Global Symposium on Millimeter-Waves, GSMM 2017.

4. **José M. Pérez Escudero**, Alicia E. Torres-García, Ramón Gonzalo, Iñigo Ederra. "Design of a Groove Gap Waveguide to Microstrip Inline Transition". 13th European Conference on Antennas and Propagation, EuCAP 2019.

5. **José M. Pérez Escudero**, Carlos Quemada, Ramón Gonzalo, Iñigo Ederra. "Integrated Fourth-harmonic Mixer Based on Schottky Diode Technology and Flip-Chip Local Oscillator Developed on Planar Technology". Progress In Electromagnetics Research Symposium, PIERS 2019, Rome.

6. **José M. Pérez Escudero**, Carlos Quemada, Ramón Gonzalo, Iñigo Ederra. "Comparison of Fourth-harmonic and Combined Doubler/Subharmonic Mixer with Integrated MMIC Based Local Oscillator", 44th International

Conference on Infrared, Millimeter, and Terahertz Waves, IRMMW-THZ 2019, París.

Additional Publication:

1. Javier Chocarro, **José M. Pérez Escudero**, Iñigo Liberal, Iñigo Ederra. "Metamaterial enhanced slotted waveguide antenna". 11th International Congress on Engineered Materials Platforms for Novel Wave Phenomena, Metamaterials 2017.

2. Javier Chocarro, **José M. Pérez Escudero**,Ramón Gonzalo, Iñigo Ederra. "Design of a Metasurface Covered Slotted Waveguide Antenna". 12th European Conference on Antennas and Propagation, EuCAP 2018.

National Conferences

Generated by this Thesis:

1. **José M. Pérez Escudero**, Ainara Rebollo, Iñigo Ederra, Ramón Gonzalo. "Método Analítico para el Diseño de una Transición Microstrip a Guía de Onda Operando en Banda W". XXXI Simposio Nacional de la Unión Científica Nacional de Radio, URSI 2016, Madrid.

Additional Publication:

1. **José M. Pérez Escudero**, Alejandro Álvarez Melcón, David Martínez Martínez, Marco Guglielmi. "Aumento del Rango Libre de Espúreos en Filtros Inductivos en Guía de Onda Rectangular". XXX Simposio Nacional de la Unión Científica Nacional de Radio, URSI 2015, Pamplona.

2. Santi Legaria, Victor Pacheco Peña, **José M. Pérez Escudero**,Miguel Beruete. "Perfeccionamiento de lentes binarias de Fresnel utilizando metamateriales". XXXII Simposio Nacional de la Unión Científica Internacional de Radio, URSI 2017, Cartagena.

3. Jorge Teniente-Vallinas, Rubén Caballero-Nagore, **José M. Pérez Escudero**, Alicia Torres García, Javier Chocarro Álvarez, Adrián Gómez-Torrent. "Micromachining of High Frequency Components at ISC/UPNA". XXXIII Simposium Nacional de la Unión Científica Nacional de Radio, URSI 2018, Granada.

4. Jorge Teniente-Vallinas, Marta Melero Frago, Carlos Biurrun Quel, Alicia E. Torres García, **José M. Pérez Escudero**. "Millimetre and submillimetre wave electronic circuit manufacture with micron precision by means of photolithography techniques". XXXIV Simposium Nacional de la Unión Científica Nacional de Radio, URSI 2019, Sevilla.

Other Merits

Research Stay

Research Stay at Terahertz and Millimetre Wave Laboratory. Chalmers University of Technology. August 2017-November 2017. Göteborg, Sweden.

Jornadas G9

Participación en V Jornadas Doctorales G9 en Palma de Mallorca, Febrero 2017.